Energy & Environmental Science

Photoinduced Charge Transfer in Transition Metal Dichalcogenide Heterojunctions – Towards Next Generation Energy Technologies

Journal:	*Energy & Environmental Science*
Manuscript ID	EE-REV-05-2020-001370.R1
Article Type:	Review Article
Date Submitted by the Author:	23-Jun-2020
Complete List of Authors:	Blackburn, Jeffrey; NREL, Sulas-Kern, Dana; National Renewable Energy Laboratory, miller, elisa; national renewable energy laboratory, chemical and nano science center

Photoinduced Charge Transfer in Transition Metal Dichalcogenide Heterojunctions – Towards Next Generation Energy Technologies

Dana B. Sulas-Kern,* Elisa M. Miller,* and Jeffrey L. Blackburn*
National Renewable Energy Laboratory, Golden CO 80401

Abstract – Increasing interest in using two-dimensional transition metal dichalcogenides (2D TMDCs) in optical energy conversion technologies creates a demand for improving the yields and lifetimes of photogenerated charge carriers. Despite inherently fast photocarrier decay in neat 2D TMDCs, the unique photophysics in these quantum-confined systems motivates continued effort to control the evolution of photoexcited states and create functional devices. An intriguing strategy to accomplish this goal is to employ TMDCs in heterojunctions with appropriate semiconductors, where energy level offsets drive photoinduced charge transfer (PCT) across material interfaces. PCT in TMDC-based systems can be optimized for many different applications, such as driving free carriers to photocatalytic sites for redox reactions like water splitting, extracting charge to perform work in photovoltaics or photodetectors, and manipulating the spin and momentum valley electronic degrees of freedom for quantum computing systems. Here, we review recent strides in optimizing PCT for such applications through greater fundamental understanding of the photophysics that occurs at TMDC/semiconductor interfaces. After giving an overview of isolated TMDC properties, synthetic methods, and the basics of PCT, we discuss TMDCs in heterojunctions with several classes of materials, including other TMDCs, small molecule semiconductors, polymers, single-walled carbon nanotubes, quantum dots, perovskites, and electrolytes. In addition to highlighting the unique benefits of each materials category, we also identify parallels across common themes, such as the roles of charge-transfer states, spin, electronic coupling, delocalization, interfacial atomic morphology, and the precise design of energy landscapes to direct charge and energy motion. We hope to capture a broad range of the valuable work in this fast-paced field to inspire new research directions for employing PCT in targeted TMDC-based systems.

Broader Context – Photoinduced charge transfer across material interfaces is a critical step in the fundamental operation of energy-related (and other) technologies, especially when employing excitonic materials where additional driving force provided by interfacial energy level offsets is needed to separate Coulombically-bound electron-hole pairs. Monolayer transition metal dichalcogenides (TMDCs) are excitonic two-dimensional semiconductors with unique properties that are controllable by quantum confinement, promising many benefits for energy conversion and storage, including photovoltaic solar energy harvesting, solar fuels generation, and energy-efficient next-generation computing strategies. Heterostructures between TMDC monolayers and other inorganic or organic semiconductors have emerged as a powerful strategy for transforming the energy of photons into the long-lived separated charges that drive these energy applications. Here, we review recent progress on the current understanding of both fundamental and applied aspects of interfacial photoinduced charge transfer within TMDC-based heterostructures and the associated implications for energy technologies.

Contents

1. Introduction

Nanomaterials offer unique advantages for a wide variety of energy-related technologies. The confinement of charge carriers to nanoscale dimensions can lead to distinctive optical and electronic properties, especially near or below the Bohr radius, which specifies the typical Coulomb-mediated electron-hole distance in a bulk material. Such quantum effects arise in materials confined in three dimensions (e.g. semiconductor nanocrystals and fullerenes), two dimensions (e.g. single-walled carbon nanotubes and semiconductor nanowires), and one dimension (e.g. graphene, borophene, and a host of two-dimensional semiconductors). A multitude of quantum confinement effects exist, but some of the most important for photoresponsive energy conversion materials are: size-tunable electronic and optical band gaps;[1-2] possible ultra-high charge carrier mobilities, in some cases approaching the ballistic limit;[3-4] markedly altered kinetics for excited-state processes relative to bulk;[5-6] and symmetry-dependent optical selection rules.[7-9]

In this review, we focus on a particular class of quantum-confined two-dimensional semiconductors comprised of transition metal dichalcogenides (TMDCs). TMDCs are layered materials with the structure MX_2, where M is a transition metal (e.g. Mo, W, Zr, Pt, etc.) and X is a group VI chalcogen (e.g. S, Se, or Te). The TMDCs can exist in several different crystal structures, which causes them to range from semiconducting (e.g. a stable H phase in common TMDCs) to quasi-metallic or metallic (e.g. unstable 1T' and 1T phases, see Section 6). The individual, two-dimensional covalently bonded MX_2 sheets are held together into larger crystal structures with relatively weak van der Waals forces between layers. TMDCs have a number of unique properties that make them promising candidates for energy conversion, energy storage, and information processing. Some compelling traits of TMDCs that we will discuss in detail are strong direct bandgap absorption in the visible region of the solar spectrum,[1] high charge carrier

mobilities and diffusion lengths,[10-11] appropriate energetics and promising kinetics for photoinduced catalysis,[12-14] and a strong correlation between spin and photon degrees of freedom based on unique momentum-valley physics.[15-16] Importantly, many of these desirable properties of TMDCs can be accentuated, improved, or synergistic in heterojunctions with complementary materials (Figure 1), offering new avenues for optimizing functional TMDC-based devices.

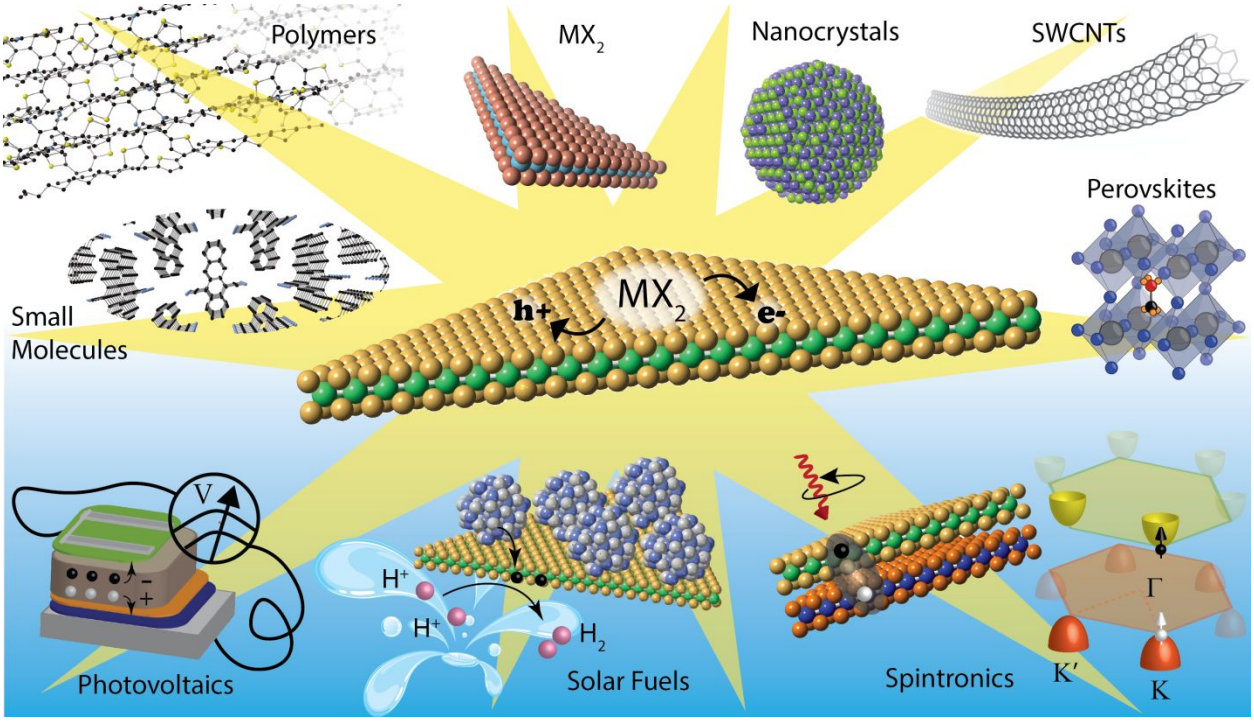

Figure 1. We discuss photoinduced charge transfer across TMDC-based heterostructures with various organic and inorganic semiconductors (top). Such heterostructures enable a number of emerging energy technologies (bottom).

Here, we review recent progress in the development of TMDC-based heterostructures, focusing specifically on the current understanding of both fundamental and applied aspects of interfacial photoinduced charge transfer and its implications for energy technologies (Figure 1). Photoinduced charge transfer (PCT) across material interfaces is a critical step in the fundamental operation of energy-related (and other) technologies, especially when employing excitonic materials where additional driving force provided by interfacial energy level offsets is needed to separate Coulombically-bound electron-hole pairs. For example, PCT is central to optimizing thin-film photovoltaic device performance by driving spatial separation of charge carriers and hindering

recombination. In this capacity, PCT underlies the function of TMDCs in solar cells and photodetectors as components in active absorbers or as extraction layers. More recently, the decreasing cost of photovoltaics along with the intermittent nature of solar electricity has driven interest in strategies to convert photon energy into value-added fuels or chemical precursors. In this capacity, PCT underlies the function of TMDCs in solar fuel generation, where the energy of photogenerated excited states can be stored in chemical bonds by converting protons, carbon dioxide, nitrogen, and other chemical inputs into molecules that can be used on demand as fuel in off-peak hours. Computing has also emerged as a dominant and growing component of our total energy consumption, motivating new strategies for information processing (computation, communication, encryption, etc.) that differ from the digital methods that have dominated over the last 50 years. In this capacity, PCT in TMDCs provides a compelling route for encoding quantum information *via* manipulation of spin-valley locked states, motivating strong interest in TMDCs for spintronics and photon-based quantum information technologies.

In this review, we discuss the role of PCT in TMDC-based heterostructures for enabling many of these exciting technologies. Importantly, we also note that there is a wealth of pioneering literature on bulk TMDC photochemistry and photophysics that goes back multiple decades,[17-19] and recent reviews summarize several important aspects of TMDCs.[9, 20-21] The explosion of studies into monolayer 2D semiconductors is heavily indebted to these pioneers of the TMDC field, and we recommend that readers explore the reviews on other aspects of TMDCs that we will point out when relevant for understanding PCT. Here, we focus on more recent work specifically covering the role of PCT in mono- and few-layer TMDC-based heterostructures, a topic which has not been covered in great detail in other reviews. With this focus, we hope to highlight recent successes and

future directions for harnessing the promise of layered semiconductors for renewable and sustainable energy conversion and storage devices.

2. Basics of Interfacial Photoinduced Charge Transfer

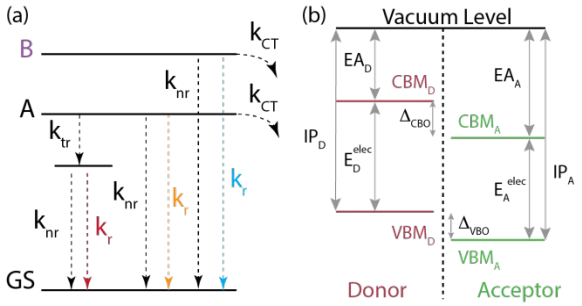

Figure 2. (a) Schematic illustration of excited-state processes (dashed lines) occurring in a TMDC following absorption of a photon to excite the A or B excitonic transition from the ground state (GS). Various excited state processes with rate k_x are shown, with detailed description in main text. (b) Energy level diagram of a Type-II heterojunction between two semiconductors (before making contact) indicating properties of the donor (*D*) and acceptor (*A*) including the ionization potential (*IP*), electron affinity (*EA*), electronic band gap (E^{elec}), conduction band minimum (*CBM*), valence band maximum (*VBM*), conduction band offset (Δ_{CBO}), and valence band offset (Δ_{VBO}).

PCT across donor/acceptor interfaces can be viewed as a subset of kinetic processes that are available to a given excited state that is generated by photon absorption. As such, the kinetics and yield of PCT are linked to the thermodynamics of charge transfer and all other competing excited-state decay processes. Figure 2 summarizes decay pathways for a representative photoexcited semiconducting TMDC that is either isolated or in contact with another semiconductor or metal at a heterojunction. Since we focus this review on monolayer (or few-layer) TMDCs, we restrict this overview to a prototypical direct-gap excitonic semiconductor with optical band gap E_{opt}, electronic band gap E_{elec}, and exciton binding energy E_{XBE}. The electronic band gap of the semiconductor reflects the energy of uncorrelated charge carriers that are not bound by the attractive Coulomb potential and can therefore be written as

$$E_{elec} = E_{opt} + E_{XBE}. \qquad \text{Equation 1}$$

The properties of photoexcited excitons in monolayer TMDCs are determined by various optical selection rules. As we further discuss in Section 5, unpolarized optical excitation produces

an equivalent population of excitons in the K and K′ valleys, whereas circularly polarized photons prepare excitons confined to either K or K′. Circularly polarized photons with appropriate energy can be used to excite spin up or spin down transitions. Depending on the TMDC composition, the lowest-energy transition may be spin-allowed or spin-forbidden, leading to corresponding bright and dark transitions.[22]

If the absorbed photon energy exceeds E_{opt}, then the initial excited state has excess energy and is typically called "hot" or "unthermalized". Hot excited states (both excitons and charge carriers) typically relax to the lowest-energy excited state by fast vibrational relaxation or internal conversion through the manifold of the excited multiplicity. Once in a relaxed excitonic state, the predominant pathways available to an exciton at low fluence are shown in Figure 2a and include: radiative recombination (k_r); non-radiative recombination (k_{nr}); interaction with a trap state (k_{tr}); intervalley scattering (not shown); and charge transfer at an interface with an appropriate material (k_{CT}). At high excitation densities, additional quasiparticle interactions can occur, such as Auger processes and exciton-exciton annihilation.[23]

Radiative recombination gives rise to photoluminescence (PL) with quantum yield (ϕ_{PL}) that is defined by the ratio between k_r and all other excited state decay pathways (k_x), also equivalent to k_r multiplied by the excited-state lifetime τ:

$$\phi_{PL} = \frac{k_r}{\sum k_x} = k_r \tau. \qquad \text{Equation 2}$$

Photon emission depends on the optical selection rules discussed in Section 5. As such, circularly polarized emission can reflect the degree to which the valley polarization is retained following various photophysical processes and PCT.[9, 24-25] Radiative recombination is an unavoidable decay pathway for semiconductors, and the reciprocity relation dictates that natively high ϕ_{PL} by avoiding nonradiative recombination is essential for materials to achieve high photon-to-electron

conversion efficiencies.[26-27] Exciton dissociation, however, decreases ϕ_{PL} and is beneficial when the carriers can be extracted. Dissociation into uncorrelated charge carriers and/or trions can occur from both hot and thermalized excitations even in isolated semiconductors with relatively large exciton binding energies.[28] Mid-gap states can also dissociate excitons by trapping charge carriers.[28-31] In some applications, such defects can play a beneficial role in tuning band energetics[32] or providing catalytic sites.[33-34] Defect states are more common in materials grown by chemical vapor deposition (~10^{12}-10^{13} states cm^{-2}) compared to exfoliation (~10^{9} cm^{-2}).[23, 29]

Interfacing a TMDC semiconductor with another semiconductor or metal opens the possibility for additional excited-state deactivation pathways, the most relevant for this review being photoinduced energy transfer and PCT. In some cases, energy transfer can compete with PCT,[35-37] although many functional TMDC-based applications require spatial separation of electrons and holes across a heterointerface (i.e. charge transfer) rather than funneling both carriers into one of the materials (i.e. energy transfer). Energy transfer can occur *via* Förster resonance energy transfer (FRET) or collisional Dexter energy transfer (DET) when the excited state's energy equals or exceeds the optical or electronic band gap of the other species in the heterojunction. FRET proceeds through resonance between transition dipole moments of transmitter and receiver species, and thus depends on the spectral overlap between the transmitter emission and receiver absorption along with the spatial alignment of their dipole orientations.[38] While FRET can be a long-range process, DET is short-range and requires orbital overlap between donor/acceptor. Nevertheless, both processes can be involved in excited-state diffusion toward or away from a heterojunction interface as well as exciton transfer across the interface.

The kinetics of interfacial PCT (k_{CT}) depend in large part on the thermodynamics at the interface, and the efficiency of charge transfer (ϕ_{CT}) depends on the ratio between k_{CT} and the rates of all other competing processes (k_x):

$$\phi_{CT} = \frac{k_{CT}}{\sum k_x} = k_{CT}\tau. \quad \text{Equation 3}$$

One of the most important characteristics for an interface that is designed to facilitate PCT is the thermodynamic driving force for charge transfer. All chemical and electrochemical reactions can be described by the change in free energy (ΔG) between reactants (with free energy G_{react}) and products (with free energy G_{prod}), where ΔG depends on the temperature (T) and the changes in enthalpy (ΔH) and entropy (ΔS) for the reaction:

$$\Delta G = G_{prod} - G_{react} = \Delta H - T\Delta S. \quad \text{Equation 4}$$

Reactions with -ΔG proceed spontaneously at a given temperature, and are called *exergonic* reactions, while +ΔG denotes *endergonic* reactions that are not spontaneous at a given temperature.

A typical way to establish a PCT driving force is to create a Type-II heterojunction, which is characterized by a 'staggered' band alignment, (see Figure 2b) where the electron affinity and ionization potential of the donor are both closer to vacuum than the corresponding energies for the acceptor. This energetic alignment facilitates electron transfer from the photoexcited donor to the acceptor and hole transfer from the excited acceptor to the donor *if* an appropriate thermodynamic driving force exists for each charge-transfer event. Equation 4 can be recast to describe the PCT driving force (ΔG_{CT}) using the free energy of charges as G_{prod} and the exciton free energy as G_{react}. The free energy of charges produced by PCT is the difference between the ionization potential of the donor (IP_D) and the electron affinity of the acceptor (EA_A), and the energy of the initial excited state is the exciton energy (E_{opt}). The driving force is therefore

$$\Delta G_{CT} = (IP_D - EA_A) - E_{opt}. \quad \text{Equation 5}$$

Error may be introduced into Equation 5 if the donor/acceptor vacuum levels are not aligned. When this is a concern, the donor/acceptor conduction band or valence band offsets ($\Delta_{CBO/VBO}$) can be used, where ΔG_{CT} is favorable when $|\Delta_{CBO/VBO}| > E_{XBE}$. In either formulation, we assume that PCT occurs from thermalized excitons occupying the lowest-energy exciton level, even for absorption of photon energies exceeding the optical gap. In reality, 'hot' charge transfer could also occur, in which case E_{opt} would be replaced by the photon energy or the energy of the higher-lying exciton level from which charge transfer occurs (if this is known).

The Marcus formulation of electron transfer connects ΔG_{CT} to the rate of PCT, k_{CT}. Despite the fact that Marcus's seminal work in the 1980's predicted k_{CT} trends in solvated molecular donor-bridge-acceptor compounds, several recent studies further suggest the veracity of Marcus theory in solid-state systems, including semiconducting polymers,[39-41] small molecules,[42] semiconducting nanocrystals,[43-44] single-walled carbon nanotubes,[45-46] and TMDCs.[44, 47] In the simplest conception of Marcus theory, k_{CT} is related to the electronic coupling between donor and acceptor (V_{DA}), the charge transfer reorganization energy (λ), and ΔG_{CT} as

$$k_{CT} = \frac{2\pi V_{DA}^2}{\hbar\sqrt{4\pi\lambda k_B T}} exp\left[\frac{-(\lambda + \Delta G_{CT})}{4\lambda k_B T}\right], \qquad \text{Equation 6}$$

where $\hbar$ is the reduced Planck constant, k_B is the Boltzmann constant, and T is temperature. The reorganization energy is related to the changes in molecular or lattice coordinates that accompany a charge-transfer event, taking a system from a neutral donor/acceptor pair to a charged $[donor]^+/[acceptor]^-$ pair. While it is important to have a large enough ΔG_{CT} to favor charge transfer, too high of driving force can be detrimental. Large ΔG_{CT} values can reduce k_{CT} by placing the system in the Marcus inverted region (where $\Delta G_{CT} > \lambda$),[48] or it could cause energetic losses that decrease system voltage and available work.

3. Predicted and Experimental Band Energies of Monolayer TMDCs

The discussion above demonstrates the importance of the TMDC conduction and valence band energies in establishing a driving force for PCT in rationally designed TMDC heterostructures. As such, we summarize some general trends in TMDC band energies. Figure 3 provides examples of calculations and experimental studies of TMDC band gaps.[12, 49] Two general trends can be observed for changes in the transition metal M and the chalcogen X for a given MX_2 series. For the chalcogen atoms, higher atomic mass in the periodic table (from S to Se to Te) results in smaller band gaps with conduction and valence band edges shifted progressively closer to vacuum (smaller *EA* and *IP*). For the two most common transition metals (Mo and W), WX_2 monolayers have smaller *EA* and *IP* values but larger band gaps than the corresponding MoX_2 monolayers.

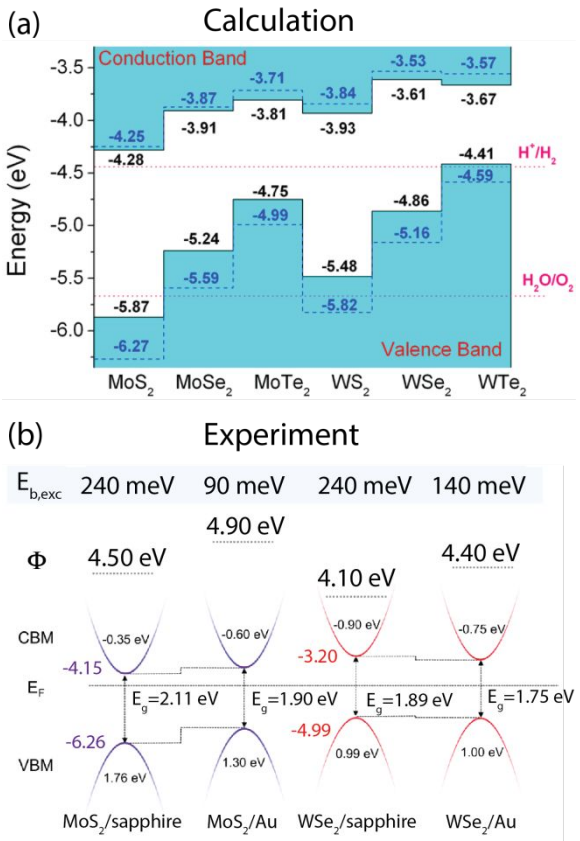

Figure 3. (a) Calculated band energies for six TMDC monolayers.[49] Solid lines were obtained by the Perdew-Burke-Ernzerhof (PBE) method, while dashed lines were obtained by the Heyd-Scuseria-Ernzerhof (HSE06) hybrid functional. Dotted pink lines give the water reduction (H^+/H_2) and oxidation (H_2O/O_2) potentials. Reprinted from ref. 49, with the permission of AIP Publishing. (b) Band energies for MoS_2 and WSe_2, either on sapphire or on gold,

determined experimentally using direct and inverse photoelectron spectroscopies.[12] The conduction mand minimum (*CBM*) and valence band maximum (*VBM*) values given in black text are referenced to the work function ($\Phi = E_F - E_{vac}$). The values in colored text for MoS_2/sapphire and WSe_2/sapphire are absolute relative to E_{vac} for direct comparison to panel (a). The electronic band gap (E_g in this figure) is $E_g = E_{CBM} - E_{VBM}$. The exciton binding energies ($E_{b,exc}$) above each sample are calculated by subtracting the measured optical band gap (E_{opt}) from E_g.

Importantly, Figure 3 suggests that the conduction band values of both MoX_2 and WX_2 monolayers are close enough to vacuum to reduce protons and produce hydrogen:

$$2H^+ + 2e^- \rightarrow H_2 \qquad \text{Equation 7}$$

Some TMDC monolayers (MoS_2 and WS_2 in Figure 3a) are predicted to have valence band energies deep enough to oxidize water to oxygen:

$$2H_2O \rightarrow 4e^- + 4H^+ + O_2 \qquad \text{Equation 8}$$

These attractive band energies are a primary motivator in considering TMDCs for applications in solar hydrogen generation. As with PCT across solid-state interfaces, the rate of PCT to produce H_2 and O_2 are related to the thermodynamic driving force available for these reactions. Recent work has also begun to explore the possible utility of TMDCs in other photocatalytic transformations. In particular, the (photo)catalytic reduction of CO_2 to C-based fuels is a valuable strategy for mitigating an important climate-forcing gas and for storing cheap renewable electrons in energy-dense carbon-carbon bonds.[50] (Photo)catalytic nitrogen fixation is also an important goal for reducing the large carbon footprint of ammonia generation for agriculture that currently constitutes ~1% of our global energy usage via the Haber-Bosch process.[51-52] In Section 12, we discuss the recent progress on understanding PCT in reactions containing TMDC catalysts, with particular focus on water splitting and hydrogen evolution.

4. TMDC Electronic Structure and Relevant Quasiparticles

The natural band gaps in TMDC semiconductors outlined in Section 3 are a primary reason that TMDCs have gained popularity for PCT-driven technologies over other 2D systems such as

graphene. While 2D systems like graphene require external perturbations to break inversion symmetry and create a finite band gap,[53-57] semiconducting TMDCs exhibit inherent monolayer inversion asymmetry and a band gap between their partially-filled metal d orbitals. This inversion asymmetry rises from the trigonal prismatic unit cell shown in Figure 4a, which extends into a 2D crystal layer with alternating atomic planes of M or X atoms that are offset in the x-y dimension.

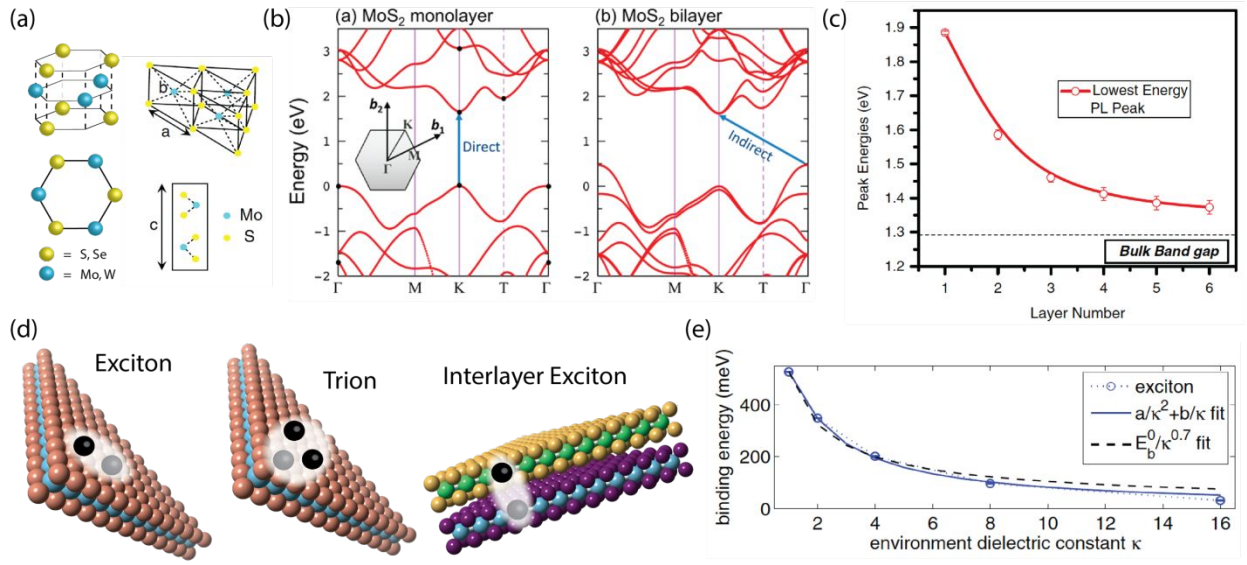

Figure 4. (a) Left: Side and top view of atomic positions in monolayer MoS_2 lattice. Right: Crystal structure of semiconducting 2H MoS_2, showing the a and b axes, along with the c axis relevant for multilayer MoS_2.[1] Reprinted with permission from ref. 1. Copyright 2010 by the American Physical Society. (b) Energy-momentum diagram for monolayer and bilayer MoS_2 showing the indirect band gap near the Γ– to K point for bilayer and the direct gap at the K-point for monolayer.[58] Inset shows the first Brillouin zone of the hexagonal atomic crystals. Reprinted with permission from ref. 58. Copyright 2016 American Chemical Society. (c) The lowest energy PL peak as a function of layer number for MoS_2 (red circles), along with the bulk band gap (dashed line).[1] Reprinted with permission from ref. 1. Copyright 2010 by the American Physical Society. (d) Three examples of bound quasi-particles formed between electrons (black) and holes (gray) in TMDCs. (e) Calculated exciton binding energy[59] for monolayer MoS_2 as a function of average dielectric constant, $\varepsilon = ½ (\varepsilon_{top} + \varepsilon_{bottom})$, where ε_{top} is dielectric constant of top surface in contact with TMDC and ε_{bottom} is dielectric constant of bottom surface in contact with TMDC (i.e. substrate). Empirical fits are given as blue line[59] and dashed line (proposed by ref. [60]). Reprinted with permission from ref. 59. Copyright 2015 by the American Physical Society.

Figure 4b shows that this monolayer structure leads to a direct band gap transition at the K-point in the hexagonal Brillouin zone, but many TMDCs transition to an indirect bandgap in the bulk or few-layer level. For example, bulk MoS_2 has an indirect lowest-energy transition centered near the Γ-point (E_{ID} = 1.29 eV) and a direct transition centered at the K-point (E_D = 1.88 eV).[1, 58, 61] At the few-layer level, as the number of layers decreases from six (6L) to two (2L), Figure 4c

shows that the indirect gap shifts from approximately 1.35 eV to 1.58 eV. This is mostly attributable to the contribution of sulfur p_z orbitals to states near the Γ point, which causes the indirect bandgap energy to be strongly dependent on interlayer coupling.[62] Importantly, the direct transition at the K-point is not dependent on interlayer coupling due to the more localized Mo *d* orbitals involved in this transition.[62] For this reason, going from 2L to 1L results in the indirect bandgap becoming larger than the monolayer direct bandgap at the K-point. This trend follows for all Mo and W-based TMDCs. Other TMDCs show a layer-number-dependent bandgap but retain the indirect bandgap as the lowest-energy transition, even for monolayers. These include HfX_2, ZrX_2, PtX_2, and PdX_2, where X = S, Se.[63-65]

With decreasing number of layers, dielectric screening also decreases and gives rise to strong Coulomb attractions between electrons and holes in monolayer TMDCs (Figure 4d). As a result, the primary quasiparticles arising from photoexcitation of monolayer TMDCs are excitons. The exciton binding energy for direct bandgap monolayer TMDCs lies in the range of 0.1 – 0.6 eV, with a strong dependence on the dielectric environment (Figure 4e and Table 1).[12, 59, 66-72] Magnetic field dependent spectroscopic experiments[70] have also enabled estimates for the physical constants of excitons in many monolayer TMDCs, as summarized in Table 1.

Table 1. Summary of optical gaps, exciton binding energies, exciton size (radius), and reduced exciton mass for several common monolayer TMDCs on substrates with varying dielectric constants.

TMDC	Optical Bandgap (eV)	Binding Energy (eV)	Electrical Bandgap (eV)	Exciton Radius (nm)*	Average ε^ or substrate	Reduced Exciton Mass Used#	Method$	Ref
MoS_2	-	0.53	-	1.1	1	$0.25m_e$	DFT	59
MoS_2	-	0.35	-	-	2	$0.25m_e$	DFT	59
MoS_2	1.94	0.22	2.16	1.2	4.4 (h-BN x2)	$0.28m_e$	DS	66
MoS_2	1.87	0.24	2.11	-	sapphire	-	PES	12
MoS_2	1.81	0.09	1.90	-	gold	-	PES	12
WS_2	-	0.51	-	-	1	$0.18m_e$	DFT	59
WS_2	-	0.32	-	-	2	$0.18m_e$	DFT	59
WS_2	2.045	0.41	2.455	1.53	1.55 (Si/SiO_2)	$0.16m_e$	DS	67
WS_2	2.06	0.18	2.24	1.8	4.4 (h-BN x2)	$0.18m_e$	DS	66
WS_2	2.09	0.32	2.41	-	1.55 Si/SiO_2	$0.16m_e$	RC	68
WS_2	2.04	>0.44	>2.48	-	1.55 quartz	-	2PPL	69
WSe_2	-	0.46	-	-	1	$0.19m_e$	DFT	59

WSe_2	-	0.29	-	-	2	$0.19m_e$	DFT	[59]
WSe_2	1.78	0.48	2.26	1.2	1.55 (SiO_2)	$0.18m_e$	DS	[70]
WSe_2	1.75	0.35	2.1	1.4	2.25 (poly/SiO_2)	$0.18m_e$	DS	[70]
WSe_2	1.73	0.22	1.95	1.6	3.30 (h-BN/SiO_2)	$0.18m_e$	DS	[70]
WSe_2	1.65	0.37	2.02	-	1.55 Si/SiO_2	-	2PPL	[71]
WSe_2	1.65	0.24	1.89	-	sapphire	-	PES	[12]
WSe_2	1.61	0.14	1.75	-	gold	-	PES	[12]
$MoSe_2$	-	0.48	-	-	1	$0.30m_e$	DFT	[59]
$MoSe_2$	-	0.32	-	-	2	$0.30m_e$	DFT	[59]
$MoSe_2$	1.64	0.23	1.87	1.1	4.4 (h-BN x2)	$0.35m_e$	DS	[66]
$MoSe_2$	1.63	0.55	2.18	-	graphene	-	STM + PL	[72]
$MoTe_2$	-	0.38			1	$0.31m_e$	DFT	[59]
$MoTe_2$	-	0.26			2	$0.31m_e$	DFT	[59]
$MoTe_2$	1.18	0.18	1.36	1.3	4.4 (h-BN x2)	$0.36m_e$	DS	[66]

[*] electron-hole hole separation

[^] Average dielectric constant, $\kappa = \frac{1}{2}(\varepsilon_{top} + \varepsilon_{bottom})$, where ε_{top} is dielectric constant of top surface in contact with TMDC and ε_{bottom} is dielectric constant of top surface in contact with TMDC (i.e. substrate). All κ values reported as relative permittivity ($\varepsilon/\varepsilon_0$) where ε_0 is the permittivity of vacuum.

[#] Reduced exciton mass, m_{exc}, defined by $m_{exc}^{-1} = m_e^{-1} + m_h^{-1}$, where m_e and m_h are electron and hole effective masses, respectively.

[$] Method abbreviations: DFT = density functional theory; DS = diamagnetic shift; PES = photoelectron spectroscopy (combination of angle-resolved photoemission spectroscopy and inverse photoemission spectroscopy); RC = reflectance contrast; 2PPL = two-photon photoluminescence spectroscopy; STM + PL = scanning tunneling microscopy and photoluminescence spectroscopy

Low dielectric screening in mono- and few-layer TMDCs also leads to trion formation under conditions of non-negligible dark carrier density, applied bias, high photoexcitation density, or excess carriers from PCT.[73-75] Trions are three-particle species consisting of an exciton bound to an extra charge carrier, where excess holes give rise to positively-charged trions and excess electrons give rise to negatively-charged trions. Trion binding energies (the energy needed to separate the extra carrier from the exciton) are typically in the range of several tens of meV for most direct bandgap TMDCs and depend on the effective mass of the additional carrier bound to the exciton, the carrier density, and Fermi energy.[76-77] Trion PL, which is observed at energies below the exciton PL peak, has been used to demonstrate the existence of excess carriers, the excess carrier type and density, and the carrier dynamics.[73-76] At high photon fluences, multi-particle interactions can give rise to biexcitons (four-particle), charged biexcitons (five-particle), and even higher order quasiparticles.[78]

The Coulomb binding of these excitonic states can be overcome to generate separated charge carriers by employing TMDCs in heterojunctions with appropriate energy level offsets as described in Section 2. Interfacial charge-transfer states can serve as intermediates to free carrier generation (i.e. an electron in one material and a hole in the other material), or as sites for charge recapture if carriers are unable to escape the interface (i.e. the reverse process). The degree to which the interfacially-bound charges can dissociate depends on factors such as the magnitude of dielectric screening for the Coulomb potential between the two charges,[79] the presence of other low-energy states available for recombination (such as triplet excitons in organics),[80] and band bending at the interface.[81] Interfacial charge-transfer states have gone by several different terminologies in the literature, such as exciplex,[82] spatially-indirect exciton,[83] and interlayer exciton.[36, 84-85] Most often, the terminology is meant to imply that the bound charges reside in different materials, in contrast to *intralayer* excitons that are created within a single TMDC. However electron-hole separation across stacked layers within a given TMDC has also been suggested to give rise to exciplex-type character,[82] and spatially-indirect excitons can be supported in the same material (e.g. MoS_2) that is separated by multiple layers of another material such as boron nitride.[86] Recent studies also suggest the existence of interlayer trions.[87-88]

5. Spin and Valley Degrees of Freedom in TMDCs

Harnessing the spin and valley degrees of freedom in monolayer TMDCs has important implications for computing, where valley degeneracy combined with spin-orbit splitting of the valence band opens new avenues for information transmission.[8-9] To this end, valleytronics and spintronics are intriguing concepts that use these nontraditional electron degrees of freedom (i.e., valley index or spin polarization) for information storage and processing, leading to technologies that go beyond the typical methods of manipulating only electronic charge.[8-9]

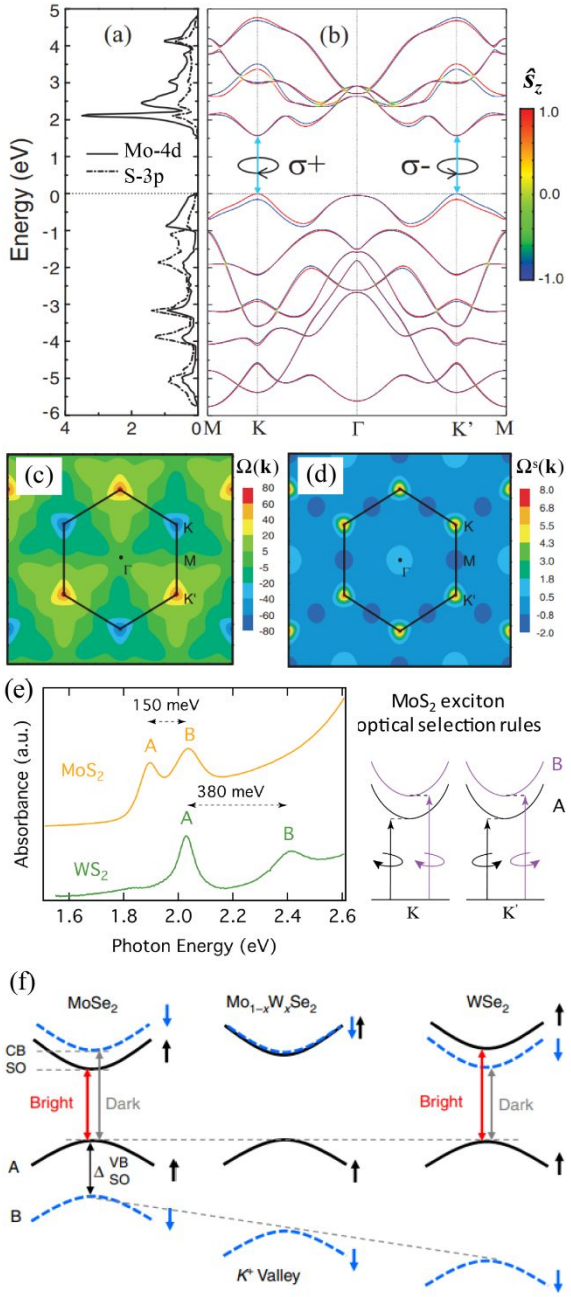

Figure 5. (a) Calculated partial density of states for MoS_2 showing contributions from Mo-4d and S-3p orbitals along with (b) the band structure of MoS_2 with the spin operator $\hat{s}_z$ projected as a color map, indicating spin-up (down-down) optical transitions coupled with circularly polarized light σ+ (σ-) at the inequivalent K (K') valleys. 2D maps in k-space show (c) Berry curvature $\Omega(\mathbf{k})$ and (d) spin Berry curvature $\Omega^s(\mathbf{k})$ highlighting differences between the K and K' high-symmetry points for MoS_2, with units in Bohrs^2. (e) Absorption spectra of CVD-grown MoS_2 and WS_2 showing larger splitting between A and B excitons due to larger spin-orbit coupling (SOC) with the heavier W transition metal, along with an illustration of spin-valley locking that enables creation of valley-polarized A and B excitons by exciting on-resonance with circularly polarized photons. (f) Illustration of increasing band gap and SOC with increasing W content, showing a switch from bright to dark lowest-energy transition caused by opposite conduction band SOC in WX_2 compared to MoX_2. Panels (a-d) are reprinted with permission from ref. 7. Copyright Year by the American Physical Society.[7] Panel (f) is reprinted by permission from Springer Nature from ref. 22. [22]

While much of the initial progress in valleytronics is owed to the rich physics discovered in graphene,[89] TMDCs promise further progress by combining similar valley physics with a natural, finite band gap. In particular, the conduction and valence band edges of both graphene and monolayer TMDCs are located at the corners of the hexagonal Brillouin zone, resulting in two degenerate but inequivalent valleys at the K and K' points, as shown in Figure 5a-d. The large difference in momentum between the two valleys is expected to limit scattering and intervalley conversion, enabling the control of valley polarization and coherence necessary for binary information transmission.

Importantly, spin-orbit coupling (SOC) also plays an essential role in preserving robust spin and valley coherence in TMDCs. Strong SOC energetically splits the band edges at the distinct valleys, as illustrated by the projection of spin operator $\hat{s}_z$ onto the MoS_2 band structure in Figure 5b, where blue indicates spin-down bands and red indicates spin-up bands. The SOC gives rise to separate A and B exciton transitions (Figure 5e) and creates locked spin and valley physics. SOC predominately splits the valence band maxima within each K valley due to the nonzero magnetic quantum number ($m_l = \pm 2$) of the constituent $d_{x^2-y^2}$ and d_{xy} orbitals, while the conduction band minimum is d_{z^2} orbital character with $m_l = 0$.[7, 90] Splitting of the valence band is on the order of hundreds of meV, with increasing magnitude for heavier metals or for larger chalcogens (see Figure 5e-f and Table 2).[22, 90-91] Because the K and K' valleys are related by time reversal symmetry, the sign of SOC splitting is opposite between the two valleys as illustrated in Figure 5b-d. This implies that the lowest-energy optical transition has a different spin polarization depending on which valley is excited, and intervalley relaxation is therefore suppressed as transitions would involve a spin flip in addition to the large change in momentum between valleys.[7, 90, 92]

Table 2. Range of reported values for energy splitting within the valence band (VB) or conduction band (CB) due to spin-orbit coupling (SOC) from experimental and computational studies[49, 90-91, 93-105]

	MoS_2	$MoSe_2$	$MoTe_2$	WS_2	WSe_2	WTe_2
VB SOC (meV)	147 ±17	185 ±3	217 ±3	434 ±15	471 ±17	485 ±4
CB SOC (meV)	4 ±3	21 ±1	28 ±9	-30 ±2	-37 ±1	-46 ±10

Unlike the large SOC splitting in the valence band, the conduction band was initially approximated as degenerate due to lack of first-order SOC from the $m_l = 0$ d_{z^2} orbital.[90] However, a small SOC splitting up to tens of meV is nevertheless observed due to (1) mixing with chalcogen p orbitals and (2) second-order effects of the d orbitals.[7, 96, 99] Interestingly, these two SOC effects have opposite effects on the conduction band splitting, which leads to material-dependent energetic ordering between spin up and spin down states as indicated by the change in sign between MoX_2 and WX_2 values in Table 2 and Figure 5f. That is, the heavier transition metal (i.e. W compared to Mo) contributes greater negative splitting, while the larger chalcogen atom (i.e. Se compared to S) contributes greater positive splitting (for the sign convention used here).[22, 91, 99] Because only transitions between bands of like-spin are allowed in monolayer TMDCs, the positive or negative conduction band splitting determines whether the TMDC monolayers have an optically bright spin-allowed ground state transitions (i.e. in MoX_2) or optically dark spin-forbidden ground-state transitions with much longer lifetimes (i.e. in WX_2).[106]

Experimentally, spin and valley coherence can be optically probed using circularly polarized light, because the lack of inversion symmetry in combination with three-fold rotational symmetry in monolayer TMDCs allows only one of the K or K' valleys to couple to light with a given polarization.[15-16, 24-25, 107-111] Although this is a valley-dependent optical selection rule, polarized light that is tuned to an appropriate energy can be used to selectively excite either the spin-up or spin-down transition. Despite the difference in momentum and spin between valleys that should suppress interconversion, neat monolayer TMDCs exhibit valley depolarization over

100's of femtoseconds to 10 picoseconds, even at low temperatures.[15, 111-115] Because these short timescales may limit the realistic use of the spin-valley polarized states, development of Type-II heterojunctions has emerged as a promising strategy to slow depolarization times to nanosecond or even microsecond scales,[24-25, 110] which we discuss further in Section 8.

6. Connection Between Crystal Structure and Electronic Structure

Manipulating TMDC crystal phase and geometry tunes the electronic structure. Mono- and few-layer TMDCs are typically found in one of three geometries (Figure 6): (1) trigonal prismatic (D_{6h} point group), denoted as 2H for few layer and 1H for monolayer; (2) octahedral (D_{3d} point group), referred to as 1T; or (3) distorted octahedral, denoted as 1T'. For 3 layers or more, a 3R phase can also exist. Figure 6b highlights calculations by Ataca et al.[116] that predict stable TMDC geometries and phases (i.e. metal, semiconducting, or half metal, where half metal refers to the majority-spin electrons yielding conducting states at the Fermi level and the minority-spin electrons yielding a semiconductor).[117]

The most common 2D TMDCs (MoS_2, $MoSe_2$, $MoTe_2$, WS_2, WSe_2, and WTe_2) are thermodynamically stable in the H phase, which is semiconducting. However, these TMDCs can be converted to the thermodynamically unstable metallic 1T phase with excess negative charge or strain.[118-122] Excess charge can be added *via* characterization techniques like transmission electron microscopy,[120] where a large flux of electrons is needed to perform the measurement. Alternatively, excess charge can be chemically imparted with dopants. Strong reductants such as n-butyl lithium, commonly used to exfoliate TMDCs,[118, 121, 123] can convert monolayer and few layers from 1H/2H to 1T and ultimately 1T'. The 1T/1T' phase is not stable and readily converts back to the 2H or 1H phase with time and/or temperature, unless it is stabilized by approaches such as surface functionalization[118] or coupling the TMDC to an electron donor, such as carbon

nanotubes.[124]

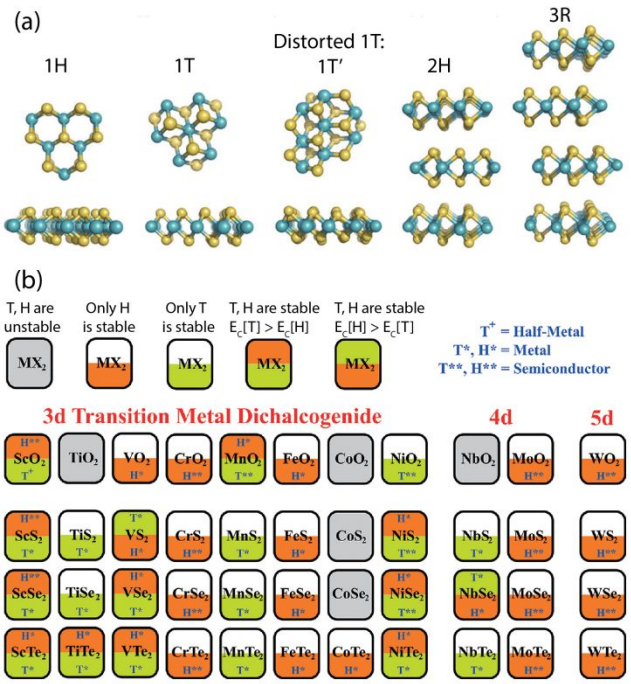

Figure 6. (a) Common structures of TMDCs.[125] Republished with permission of Royal Society of Chemistry, from ref. 125; permission conveyed through Copyright Clearance Center, Inc. (b) Diagram of stable TMDC structures from density functional theory. For each TMDC, the stable geometry is indicated by color and lowest energy structure is identified by letter (metallic, half-metallic, or semiconductor).[116] Reprinted with permission from ref. 116. Copyright 2012 American Chemical Society.

The 1T phase typically relaxes to a 1T' state with a superstructure within each layer.[125] The 1T' phase is sometimes called *quasi-metallic* because it possesses very similar qualities to the 1T phase along with a small band gap opening. For example, few-layer 1T' $MoTe_2$ has a band gap up to 60 meV due to large SOC, and other common 1T' TMDCs are predicted to have a few meV to few 100 meV band gap.[126-129]

Strain can also manipulate TMDC electronic structure. Mechanical strain can convert a direct band gap to an indirect band gap that decreases in energy with strain.[119, 130] Other studies have demonstrated that excess charge strains the lattice structure to an intermediate point between 2H and 1T where the band gap is reduced.[122, 131] Coupling TMDCs to a curved surface, such as Au nanoparticles, can also impart strain and charge transfer that decreases the 2H nature.[132]

7. Synthesis of Mono- and Few-Layer TMDCs

Many reviews have been published on growing and exfoliating TMDCs to produce mono- and few layer TMDCs.[20-21, 133-139] Growth (bottom-up approach) and exfoliation (top-down approach) produce a range of TMDC options that can be tuned for a desired application or property including thickness, lateral size, shape, purity, defects, and phase. Gas-phase TMDC growth routes, such as chemical vapor deposition (CVD) or molecular organic chemical vapor deposition, are performed in a furnace, whereas hydro/solvothermal methods grow 2D layers from solution. In all growth techniques, recipes are designed with variables such as the precursors, temperature, time, pressure, flow rate, substrates, carrier gases, and solvent. Monolayers are grown in CVD furnaces on flat substrates that can tolerate high temperatures (up to 1000 °C), such as quartz, silicon oxide, and sapphire (Figure 7, top), and lateral sizes typically range from ~1 to 100 microns.[133-135] Large area (~few cm), few layers, and defect-controlled flakes can also be controllably grown by varying the growth recipes.[140-143] Solution-based hydro/solvothermal techniques can create unique interfaces with a variety of materials and shapes, such as nanoflowers and nanospheres.[25, 138, 144] The hydro/solvothermal growth step typically occurs in a sealed autoclave using high temperature and pressure to create 2D TMDC nanosheets.

Exfoliation is also a viable technique because bulk TMDCs are held together by weak Van der Waals forces and chemical bonds do not need to be broken to separate layers. The main TMDC exfoliation methods are micromechanical cleavage, mechanical-force-assisted liquid exfoliation, and chemical exfoliation. Micromechanical cleavage can be done with the “scotch tape method” similar to graphene mechanical exfoliation where layers are peeled off from the bulk crystal using tape.[145-146] Compared to other approaches, mechanical exfoliation from pure bulk TMDCs typically generates 2D layers with a lower number of defects on the basal sites.[146] However since this method is done by hand, it is difficult to reproducibly generate similar size/thickness TMDCs

in large quantities.

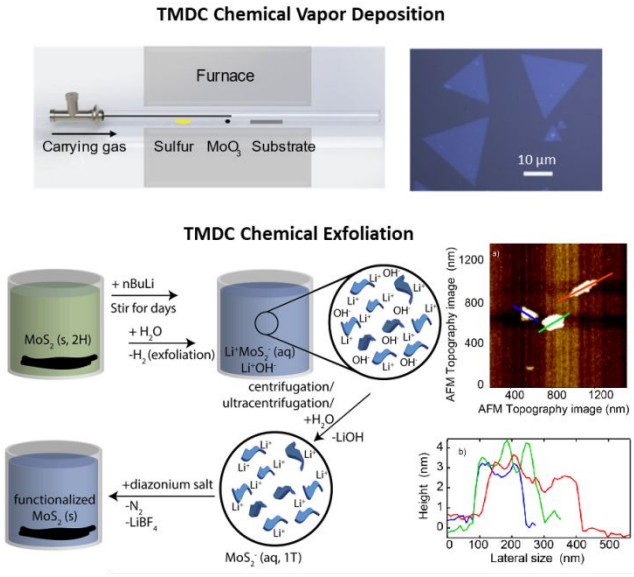

Figure 7. Common techniques for 2D TMDC growth and exfoliation. Top: Chemical vapor deposition and optical image of 2D monolayers and few layers. Bottom: Chemical exfoliation of 2D nanosheets using n-butyl-lithium followed by functionalization with a diazonium salt. The atomic force microscopy image and line scan are representative of the nanosheets height and width.

Solution-based exfoliation can be done via mechanical force or ion intercalation in solution. Mechanical-force-assisted liquid exfoliation is performed in a liquid with force applied by sonication or shear force. To effectively exfoliate TMDCs and prevent restacking during sonication, the solvent's surface energy should match that of the layered bulk material.[21, 147] Surfactants or polymers can enhance exfoliation by tuning the surface energy of the solution.[148-149] This inexpensive technique results in a wide distribution of sizes and thicknesses, but centrifuging/filtering can decrease the spread. Shear-force-assisted liquid exfoliation has been proposed as a higher-throughput way to scale up the production of 2D materials.[150] With both of these liquid exfoliation methods, the resulting 2D layers likely have surfactant/intercalating molecules on the surface, which need to be considered or removed from the 2D layer prior to use.

Chemical intercalation is another route for exfoliating TMDCs (Figure 7, bottom). The most common chemical exfoliant is n-butyl lithium where the Li+ intercalates the bulk TMDCs.[118,

[123, 151] This method is high yield, but the lateral size and thickness of nanosheets is not well controlled. Using n-butyl lithium requires great care, because H_2 is produced and could be explosive and flammable if generated in high quantities. The ion intercalation step involves charge transfer to the TMDC, which partially converts it from 2H to the 1T/1T' phase. Typically, n-butyl lithium exfoliation yields mixed phase nanosheets with both 1T/1T' and 2H.[118, 152] A similar idea to the chemically-induced ion intercalation is electrochemical Li+ intercalation where the Li+ ion intercalates the externally-reduced TMDCs.[153]

To create heterojunctions for various applications, TMDCs need to be interfaced to other semiconductors, nanomaterials, electrodes, and substrates. Heterojunctions can be created during growth processes in the bottom-up approaches or post TMDC growth/exfoliation. Small variations in growth recipes can enable sequential deposition of different TMDC layers or other 2D materials like graphene and hexagonal boron nitride.[154-156] Solution growth recipes can include other materials in the solution, such that the TMDCs grow directly onto these materials or substrates to create unique interfaces.[157-158] Methods such as thin film transfers, spraying, spin-coating, physical vapor deposition, hydrothermal mixing, membrane filtration, and grinding are also used to create interfaces between TMDCs and other semiconductors (e.g. TMDCs, organics, quantum dots, carbon nanotubes, graphitic carbon nitride, perovskites) or substrates (e.g. indium-doped tin oxide, TEM grids, metallic substrates).[25, 159-163] In the following sections, we discuss several different types of TMDC heterojunctions and highlight unique aspects of controlled heterojunction fabrication (such as interfacial alignment) when relevant.

8. Photoinduced Charge Transfer at TMDC/TMDC Heterojunctions

Heterojunctions between two (or more) different monolayer TMDCs have emerged as fascinating model systems for PCT, allowing for highly controlled studies connecting charge-

transfer kinetics to interfacial thermodynamics and spin/valley populations. Charge transfer in several TMDC/TMDC heterojunctions is driven by Type-II band offsets, as illustrated in Figure 8. These band alignments are often calculated,[164] but a number of experimental methods are also used to determine CB and VB offsets (Δ_{CBO} and Δ_{VBO}, respectively), including scanning tunneling spectroscopy,[165-166] photoelectron spectroscopy,[12] and angle-resolved photoelectron spectroscopy (ARPES).[167]

Several groups have recently demonstrated a photovoltaic effect enabled by PCT in TMDC/TMDC heterojunction devices.[136, 168] For example, Lee et al. constructed a van der Waals stacked p-n junction between aluminum-contacted n-type MoS_2 and palladium-contacted p-type WSe_2.[168] The authors observed diode-like rectification at zero gate voltage, and spatial photocurrent mapping indicated that the photocurrent arose from charge separation at the MoS_2/WSe_2 vertical junction. Increasing the carrier density in the monolayers using a positive or negative gate voltage decreased the photocurrent density, as expected for either Shockley-Read-Hall (SRH) or Langevin recombination. Modeling this gate voltage dependence with either mechanism alone was insufficient to reproduce the data, suggesting that recombination is influenced by a combination of both mechanisms. Photocurrent collection improved when using graphene electrodes due to direct vertical charge transfer to graphene rather than relying on lateral diffusion through the TMDCs to the metallic contacts. Cheng et al. studied MoS_2/WSe_2 heterojunctions in a similar geometry,[136] where they observed good rectification, efficient electroluminescence, and external quantum efficiencies in the range of 8% (633 nm) to 12% (514 nm) with no applied gate voltage.

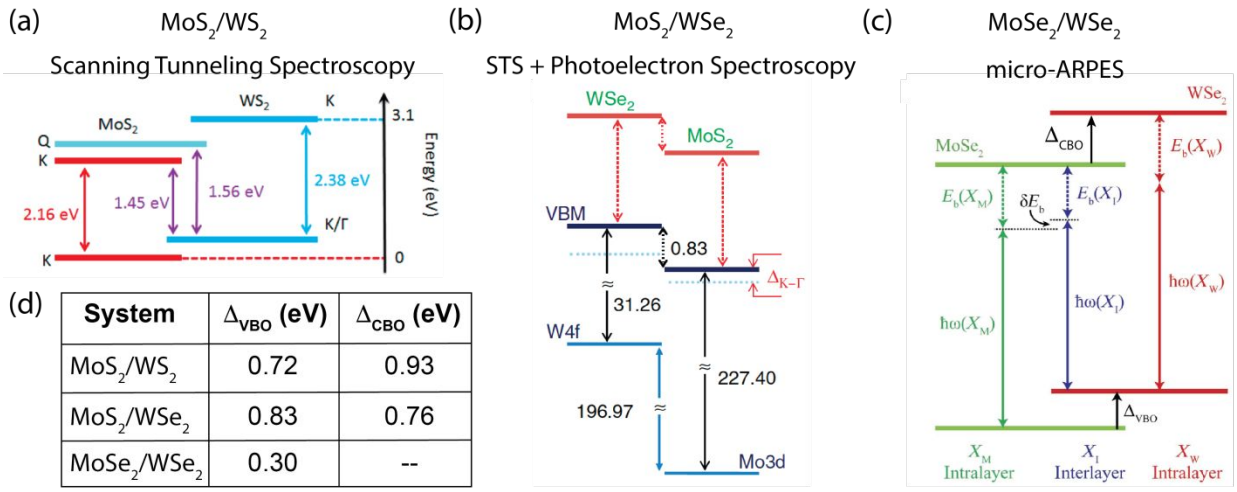

(d)

System	Δ_{VBO} (eV)	Δ_{CBO} (eV)
MoS_2/WS_2	0.72	0.93
MoS_2/WSe_2	0.83	0.76
$MoSe_2/WSe_2$	0.30	--

Figure 8. Experimentally Determined Band Alignments for Select TMDC/TMDC Heterojunctions (a) MoS_2/WS_2, determined by scanning tunneling spectroscopy (STS).[166] Reprinted with permission from ref. 166. Copyright 2016 American Chemical Society. (b) MoS_2/WSe_2, determined by a combination of STS and photoelectron spectroscopy.[165] In addition to the valence band maximum (VBM) and conduction band minimum (CBM), tungsten 4f (W4f) and molybdenum 3d (Mo3d) core level energies are shown, as are the splitting energies between VBM at the K and Γ points ($\Delta_{K-\Gamma}$), obtained by ARPES. Reprinted by permission from Springer Nature from ref. 165. (c) $MoSe_2/WSe_2$, determined by micro-angle-resolved photoelectron spectroscopy (micro-ARPES).[167] Also highlighted are the three exciton energies [$\hbar\omega(X_i)$] and their associated binding energies [$E_b(X_i)$] – $MoSe_2$ intralayer (X_M), WSe_2 intralayer (X_W), and interlayer exciton (X_I). From Ref. 167. © The Authors, some rights reserved; exclusive licensee American Association for the Advancement of Science. (d) Table showing experimental valence band offsets (Δ_{VBO}) and conduction band offsets (Δ_{CBO}) for each of these systems.

These demonstrations of photocurrent generation in functional TMDC/TMDC devices are promising, but the development of design principles for further device optimization depends on a number of important *fundamental* considerations that we discuss in the following sections, including the time scales and yields of ultrafast charge transfer and recombination, the formation of interlayer excitons, the role of momentum in PCT and recombination, and the impact of spin-valley polarization. The bulk of our discussion centers around *vertical* heterojunctions fabricated by growing or stacking individual TMDC monolayers on top of each other to form bilayers or even trilayers. At the end of the section, we briefly discuss emerging but less studied *lateral* heterostructures, where different TMDC monolayers are covalently stitched together at coherent in-plane interfaces, typically through well-controlled vapor-phase growth methods.

8.1 Ultrafast Charge Transfer in TMDC/TMDC Hetero-Bilayers

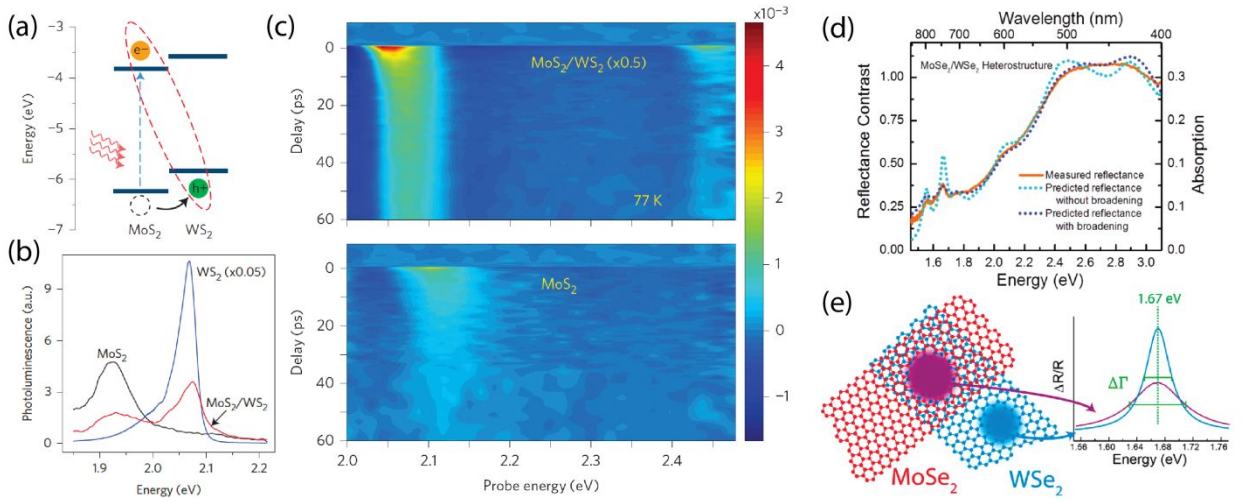

Figure 9. (a) Schematic of band diagram of MoS_2/WS_2 bilayer that facilitates photoinduced hole transfer from MoS_2 to WS_2.[169] (b) PL of MoS_2 and WS_2 is quenched in this bilayer.[169] (c) 2D transient absorption map showing (top) WS_2 ground state bleach following pumping of lower bandgap MoS_2 and (bottom) MoS_2 only.[169] (d) Reflectance contrast (RC) spectra of $MoSe_2/WSe_2$ heterojunction, simulated from the dielectric functions of the respective monolayers with (blue dotted line) and without (cyan dotted line) additional peak broadening. Orange solid line shows the measured RC spectrum.[170] (e) Transient reflectance at the $MoSe_2/WSe_2$ interface (purple trace) and at monolayer WSe_2 only (blue trace). Panels (a) – (c) are reprinted by permission from Springer Nature from ref. 169. Panels (d) – (e) are reprinted with permission from ref. 170. Copyright 2015 American Chemical Society.

Probing ultrafast charge-transfer events at Type-II TMDC/TMDC heterojunctions is often achieved using PL (Figure 9b) and transient absorption (TA, Figure 9c) spectroscopies.[169] For example, Figure 9b shows quenching of the direct-gap PL from individual monolayers in MoS_2/WS_2 heterojunctions due to interfacial PCT.[169] In principle, PL quenching of the larger bandgap WS_2 layer could result from energy transfer or charge transfer when WS_2 is excited. However, energy transfer would quench only the WS_2 PL and enhance PL from the lower-gap MoS_2 layer, while charge transfer quenches both layers. In addition to mutual PL quenching, Hong et al. confirm photoinduced hole transfer in MoS_2/WS_2 heterojunctions using TA spectroscopy.[169] Figure 9c shows photobleaching of the WS_2 A exciton transition (2.06 eV) following selective photoexcitation of MoS_2 (1.86 eV). Since the 1.86 eV pump photons cannot excite the WS_2 layer, the authors conclude that the WS_2 bleach arises from hole transfer from MoS_2 to WS_2. The rise time of the WS_2 bleach suggests hole transfer faster than the instrument response of ~50 fs. This strategy of pumping the lowest-energy TMDC exciton to negate the possibility of energy transfer

is a ubiquitous feature of probing PCT, although appropriate experimental design and analysis can also extract PCT kinetics upon photoexcitation of higher energy excitons.

Ceballos and co-workers performed similar TA measurements on $MoS_2/MoSe_2$ heterojunctions formed by mechanical exfoliation and transfer stacking.[171] The authors found electron and hole transfer times on par with or faster than the instrument response time of ~200 fs. Spatially-indirect excitons formed by charge transfer recombined on time scales of 50 – 300 ps, depending on excitation wavelength and fluence. The slowest decay times in the heterojunction represent approximately two-fold longer-lived states relative to excitons in separate MoS_2 or $MoSe_2$ monolayers.

Rigosi et al. suggest a simple analysis for estimating the lower bound of charge-transfer times in TMDC/TMDC heterojunctions based on steady-state optical absorption.[170] They produced randomly-oriented (i.e., no intentional crystallographic alignment) bilayer heterojunctions of both MoS_2/WS_2 and $MoSe_2/WSe_2$ on quartz substrates using mechanical exfoliation and transfer techniques. The excitons' absorption transitions were broadened in the heterojunctions relative to the same transitions in individual TMDCs, with the A and B transitions broadened by about 25 – 30 meV and the C and D excitons broadened by 150 (+/- 60) meV. The authors ruled out many possible sources for this broadening: processing conditions, doping, strain, enhanced thermal phonon scattering in heterojunctions, energy transfer between layers in the heterostructure, and intervalley scattering within individual layers of the heterostructure. Based on the staggered Type-II band alignment expected for these heterojunctions, the authors suggest that the broadening arises from ultrafast PCT. That is, the fast exciton decay causes uncertainty in its transition energy, so the uncertainty relationship $\tau = {\hbar}/{\Delta\Gamma}$ can be used to calculate the exciton population lifetime τ associated with the observed energetic broadening $\Delta\Gamma$. For the A and B

transitions, the 25 – 30 meV broadening corresponds to an estimated lower bound for the PCT time of 25 – 30 fs.

PCT across TMDC/TMDC heterojunctions can also be identified by emergence of trion PL.[73, 172] For example, Bellus et al. identified emission from negative trions (X^-) in WS_2 following electron transfer from $MoSe_2$.[73, 172] In this case, the electrons transferred from $MoSe_2$ to excitons generated via steady-state excitation of WS_2, producing negative trions which emit between 60 meV (low excitation power) to 80 meV (high excitation power) lower in energy than the neutral WS_2 exciton PL. The authors estimated 62 +/- 2 meV for the WS_2 trion binding energy based on extrapolation of the power-dependent Stokes shift of the trion peak. Similarly, in $MoSe_2/MoS_2$ heterostructures, Kim et al. observed negative MoS_2 trions and positive $MoSe_2$ trions following electron transfer from $MoSe_2$ to MoS_2.[73, 172]

The ultrafast charge-transfer times observed in TMDC/TMDC heterojunctions have motivated rigorous theoretical studies aimed at understanding charge-transfer mechanisms. Long et al. reported time-domain *ab initio* simulations of PCT and recombination across $MoS_2/MoSe_2$ heterojunctions.[173] Their calculations suggest that charge separation is facilitated by excited-state delocalization between donor ($MoSe_2$) and acceptor (MoS_2). This interfacial quantum coherence helps to overcome the strong electron-hole Coulomb attraction, and the resulting transfer times correlate with the coherence time, nonadiabatic coupling, density of acceptor states, and coupling with high-frequency vibrational modes. For the $MoS_2/MoSe_2$ heterojunction, these considerations lead to sub-picosecond interfacial charge transfer for both electron and hole, with faster electron transfer than hole transfer. The calculations suggest that electron-hole recombination is slower in the heterojunction (680 ps) relative to neat MoS_2 (41 ps) or neat $MoSe_2$ (63 ps), with computed

recombination times trending with experimental values (240 ps,[171] 100 ps,[174-175] and 125 ps,[176] respectively).

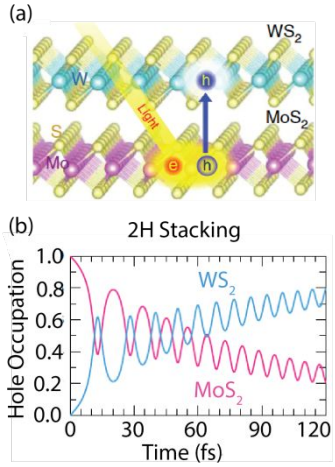

Figure 10. Theoretical calculation of coherent charge transfer across MoS_2/WS_2 interface.[177] (a) Schematic of photoinduced hole transfer from MoS_2 to WS_2. (b) Hole population dynamics modeled at 300 K resulting from photoexcitation of MoS_2.[177] Reprinted by permission from Springer Nature from ref. 170.

Wang et al. utilized time-dependent density functional theory and molecular dynamics to study hole transfer from MoS_2 to WS_2 (Figure 10).[177] The authors found that PCT is associated with the collective motion of holes across the interface, resulting in a macroscopic dipole similar to a parallel plate capacitor. Interestingly, while this interfacial dipole field *opposes* the hole transfer from MoS_2 to WS_2, it dynamically enhances the electronic coupling between the states in the two materials and ultimately enhances the hole transfer rate. The coherent charge oscillations couple strongly to Γ-point A_{1g} phonon modes that correspond to out-of-plane vibrations of sulfur atoms. This coherent ultrafast charge transfer occurs predominantly for the energetically favorable 2H stacking, but not for the 3R and AB′ stacking configurations where the calculated charge-transfer rate is accordingly much slower.

8.2 Inter-layer Excitons in TMDC/TMDC Heterostructures

Following PCT, charges separated across TMDC/TMDC interfaces may still experience significant Coulomb attraction and exist as stable charge-transfer excitons. Charge-transfer states

appear frequently in donor/acceptor systems, especially when dielectric screening is relatively inefficient.[25, 39, 79-80, 178-180] In layered 2D materials, charge-transfer states are widely referred to as inter-layer excitons (ILEs). Excellent reviews exist on ILEs[25] and the general behavior of charge-transfer states.[180] Here, we recount a few important considerations and recent discoveries.

We first note that, while ILEs could be a necessary intermediate for free carrier generation, they may simultaneously serve as a loss pathway for solar fuels or PV applications via charge recapture or inhibiting separation of mobile carriers that could be collected as current or driven to a catalytic center. While ILEs typically have longer lifetimes than intra-layer excitons, they still recombine significantly faster than truly free charges.[84-85] ILE binding energies have been reported in the range of 90 to 200 meV.[167, 181 180] In other low-dielectric systems with similar charge-transfer state binding energies, it has long been debated how it is possible to reach 100% absorbed photon-to-electron internal quantum efficiency despite the existence of these low-energy interfacially-bound "traps".[180, 182-183] To this end, Zhu et al. discussed the possible routes by which (i) charge generation may bypass relaxation to localized charge-transfer excitons (e.g. *via* charge delocalization in the donor and/or acceptor phases) or (ii) the charge transfer exciton binding energies can be countered by a potential landscape in the opposite direction (e.g. a free energy gradient from interfacial dipoles or structural inhomogeneity at/near the interface).[180]

ILEs are often characterized by their sub-gap luminescence features. Figure 11a shows that ILEs in TMDC/TMDC heterojunctions emit at energies below the emission of either isolated TMDC,[85, 184] where the $MoSe_2/WSe_2$ system exhibits ILE PL nearly 300 meV below the $MoSe_2$ exciton PL.[85] Interestingly, the $MoSe_2/WSe_2$ ILE can be resolved into two narrow peaks at low temperature (Figure 11b). Some groups assign these peaks to inter-layer spin-triplet (1.39 eV) and spin-singlet (1.41 eV) transitions.[185-186] In this suggested assignment, the energy difference of ~20

meV between these peaks represents the SOC spin-splitting in the CB. The authors suggest that breaking of the out-of-plane mirror symmetry in hetero-bilayers brightens the triplet transition denoted as IX_T in Figure 11c, which is in contrast to neat monolayers where recombination between bands of opposite spin is a spin-forbidden dark transition. For rotation angle of 60° between the TMDC layers, the K valley of $MoSe_2$ aligns with the K′ valley of WSe_2, and the ILE spin-splitting can be resolved up to 200 K.[186] Both peaks show giant valley Zeeman splitting (Figure 11d), with Lande g-factors of ~15 for the 1.39 eV ILE and ~11 for the 1.41 eV ILE.[186] Geim et al. provide an alternate interpretation that assigns the two peaks to an interlayer exciton (1.41 eV) and interlayer trion (1.39 eV).[88] In making this assignment, the authors suggest that the temperature dependence is inconsistent with the two peaks arising from different interlayer excitons, and they use bias-dependent doping studies to support the assignment of the lower-energy peak to an interlayer trion.

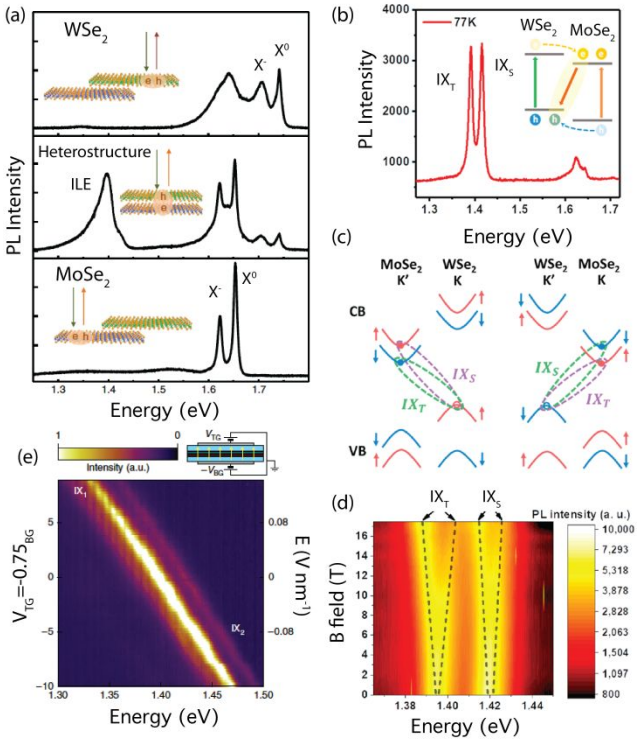

Figure 11. Interlayer Excitons in $MoSe_2/WSe_2$. (a) PL spectra of WSe_2 (top), $MoSe_2$ (bottom) and $MoSe_2/WSe_2$ heterostructure (middle), showing existence of neutral exciton PL (X^0), trion PL (X^-) and interlayer exciton PL (ILE).[85]

Reprinted by permission from Springer Nature from ref. 85. (b) 77 K PL spectrum of $MoSe_2/WSe_2$ heterostructure, showing triplet (IX_T) and singlet (IX_S) ILE emission.[186] (c) ILE configurations at adjacent K/K′ valleys of $MoSe_2/WSe_2$. Solid dots represent the electrons and the open circles represent the holes. Dashed lines represent formation of IX_S and IX_T, where green (purple) color represents σ+(σ−) helicity PL observed experimentally.[186] (d) Color plot of $MoSe_2/WSe_2$ ILE PL (T = 77 K, CW excitation at 1.959 eV) as a function of applied out-of-plane magnetic field.[186] Panels (b) – (d) are reprinted with permission from ref. 186. Copyright 2019 American Chemical Society. (e) Map of ILE PL for top- and bottom-gated $MoSe_2/WSe_2$ bilayer device as a function of applied gate voltages V_{TG} and V_{BG} when sweeping at constant doping.[185] For this device, IX_1 is the triplet ILE and IX_2 is the singlet ILE. Reprinted by permission from Springer Nature from ref. 185.

ILEs appear to retain memory of the initial valley polarization created by circularly-polarized photoexcitation of excitons in the constituent TMDC layers.[25, 186] For example, the valley polarization of the 1.41 eV ILE in $MoSe_2/WSe_2$ is as high as 100% at 23 K and 85% at 82 K, due to the long valley lifetime of the holes.[186] The systematically-varying helicity associated with peaks in the ILE manifold fine structure can be rigorously assigned and can even be used to manipulate the outgoing polarization via electrical control.[185-186] The ILE emission energy can also be controlled by an out-of-plane electric field (Figure 11e), where the field induces a strong Stark effect due to the substantial out-of-plane dipole moments caused by the opposite carriers of the ILE residing in adjacent layers.[185, 187]

ILEs in TMDC hetero-bilayers represent a particularly interesting model system for probing the degree to which interfacial crystal lattice (mis)match affects orbital interactions and interfacial electronic structure. When the lattice vector of one TMDC layer is rotated with respect to the same lattice vector of the other TMDC, this rotational mismatch leads to periodic atomic registry variations in both real space and momentum space (Figure 12a and 12b). Twist-angle-dependent orbital hybridization can significantly modify the transition energies of momentum-direct ILEs. Kuntsmann et al. recently showed for MoS_2/WSe_2 hetero-bilayers that the ILE PL intensity around 1.6 eV varied little with twist angle, in contrast to what would be expected for a momentum-direct (K-K) interlayer transition formed from the electron and hole being in the K-valley band minima in each TMDC.[188] DFT calculations of the twist angle dependent ILE energies

suggested that the observed ILE is *momentum-indirect* having hybrid Γ-K character (Figure 12c-d). Tight-binding calculations suggested nearly double Γ-K binding energy (0.55 eV) compared to the K-K binding energy (0.29 eV) due to delocalization of the hole wave function over the two TMDC layers that enhances the electron-hole Coulomb attraction.

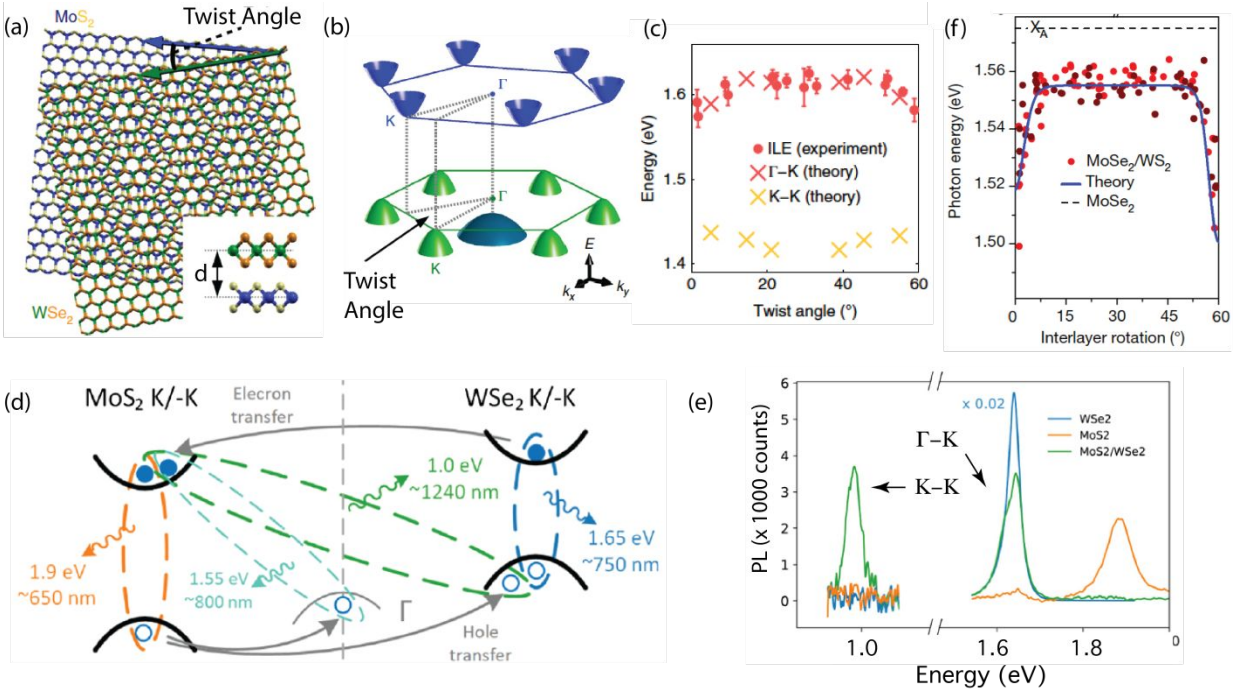

Figure 12. Momentum-direct and momentum-indirect excitons in TMDC/TMDC hetero-bilayers. (a) Atomic structure illustration of a twisted MoS_2/WSe_2 hetero-bilayer. Inset shows side view.[188] (b) Two-dimensional band structure of same hetero-bilayer near the band edges. At twist angles of 0° and 60° (not shown), the K-K ILE is momentum-direct, whereas for other twist angles, both the K-K and Γ-K ILEs are momentum-indirect.[188] (*c*) Configurations and energies of the K-K and Γ-K ILEs for the MoS_2/WSe_2 hetero-bilayer.[188] Panels (a) – (c) are reprinted by permission from Springer Nature from ref. 188. (d) Experimental ILE energies and DFT-calculated transition energies for MoS_2/WSe_2 hetero-bilayers with different twist angles, showing the quantitative agreement of Γ − K with experiment.[187] (e) Room-temperature PL spectra for isolated MoS_2 (orange) and WSe_2 (blue) monolayers, and crystollographically aligned (twist angle near 0°) hetero-bilayer (green).[187] The momentum-direct K-K ILE can be observed for the heterostructure near 1.0 eV. (f) $MoSe_2/WS_2$ hetero-bilayers have strong hybridization at 0° and 60° that leads to lower energy emission features at these nearly aligned orientations. Panels (d) – (e) are reprinted with permission from ref. 187. Copyright 2019 by the American Physical Society.

Karni et al. measured PL spectra deeper into the infrared on a similar MoS_2/WSe_2 hetero-bilayer with twist angle near 0° to observe the *momentum-direct* K-K ILE near 0.97 eV (Figure 12e).[187] In contrast to the Γ-K ILE observed near 1.6 eV,[188] the direct K-K ILE emission was extremely weak for intentionally misaligned layers. The authors also demonstrated that the energy

of the K-K ILE PL peak could be systematically shifted with a perpendicular applied electric field, revealing an out-of-plane dipole of roughly 0.5 – 0.8 *e* nm (24 – 38 D) for an electron in the MoS_2 layer and hole in the WSe_2 layer.[187]

For hetero-bilayers where either the CBs or VBs are near-isoenergetic, Alexeev et al. recently demonstrated that interlayer hybridization can be especially strong at small twist angles (i.e. 0° and 60°) where Brillouin zones of the two layers are aligned (Figure 12f).[151] In $MoSe_2/WS_2$, holes in the $MoSe_2$ layer form ILEs with a twist-dependent superposition of electron states in the adjacent WS_2 monolayers. Hybridization is strongest near 0° and 60°, leading to a stabilization of the ILE at these angles with corresponding decrease in PL energy (Figure 12f).

While the twist-angle-dependent optical studies discussed thus far characterize spatially-averaged ILE properties for a given twist angle, it is important to note that twist angle between the stacked 2D crystal structures leads to periodically-repeated patterns of varying atomic (and momentum) alignment as implied by Figure 12a. This is called a Moiré superlattice, and corresponding modulation in potential energy can localize ILEs if the Moiré periodicity on the order of 10 nm or greater.[189-190] Large detuning of CB and VB energies in stacked hetero-bilayers (e.g. in $MoSe_2/WSe_2$) can lead to variations in the interlayer band gap along the heterostructure plane and deep Moire potential wells of 100-200 meV.[190] Interestingly, Tran et al. showed that the strong connection between rotational symmetry with ILE confinement and optical selection rules results in a complex PL spectrum with multiple ILE resonances having alternating circularly polarized PL, opposing magnetic field induced PL energy shifts, and systematically varying lifetime.[190-191]

8.3 The Role of Momentum in Charge Transfer and Recombination

Since photoexcitation of a direct-gap TMDC monolayer produces excitons in the lowest-energy K valleys, the charge transfer and recombination rates should, in theory, be quite sensitive to the degree of lattice registry (twist angle) between the two layers. However, the observation of ILEs for a wide variety of twist angles *via* PL studies such as the ones discussed above makes it clear that there may be mechanism(s) by which crystal momentum mismatch is circumvented to facilitate charge transfer and recombination. In this section, we consider recent experiments that delve into how/why charge transfer and recombination can occur in mis-aligned TMDC/TMDC heterojunctions.

Yu et al. made an early observation for MoS_2/WS_2 heterojunctions that the efficiency of interfacial PCT did not depend strongly on lattice (mis)match between the two layers.[192] The authors compared hetero-bilayers created in an epitaxial CVD process, whereby either separate monolayers were grown and mechanically stacked or the two layers were co-deposited into epitaxial heterojunctions. In both cases, PCT was inferred from PL quenching by 2 orders of magnitude relative to the neat monolayers. While the relative crystal orientations were not measured in this study, this initial result suggested that epitaxial crystal alignment may not correlate strongly with the efficiency of PCT in this model TMDC hetero-bilayer.

Chen et al. suggest that hot charge-transfer states provide a mechanism for circumventing momentum mismatch across randomly-stacked TMDC/TMDC hetero-bilayers.[193] This study utilized pump-probe TA measurements that could probe either excitons in the visible range or free charge carriers in the mid-infrared. They studied a MoS_2/WS_2 heterojunction epitaxially grown in a two-step CVD method, where the relative stacking orientations were 0º (AA stacking, momentum-matched) and 60º (AB stacking, momentum-mismatched). Their results were consistent with a two-step mechanism (Figure 13a) whereby the initially excited exciton in one

TMDC dissociates by charge transfer to produce a hot electron ($\tau \approx 50$ fs) in the other TMDC. This forms weakly-bound hot ILEs that cool over 800 fs. The authors suggest that the excess energy of the intermediate hot ILE allows the state to sample a broader range of momentum space and overcome momentum conservation requirements determined by the CB minima and VB maxima.

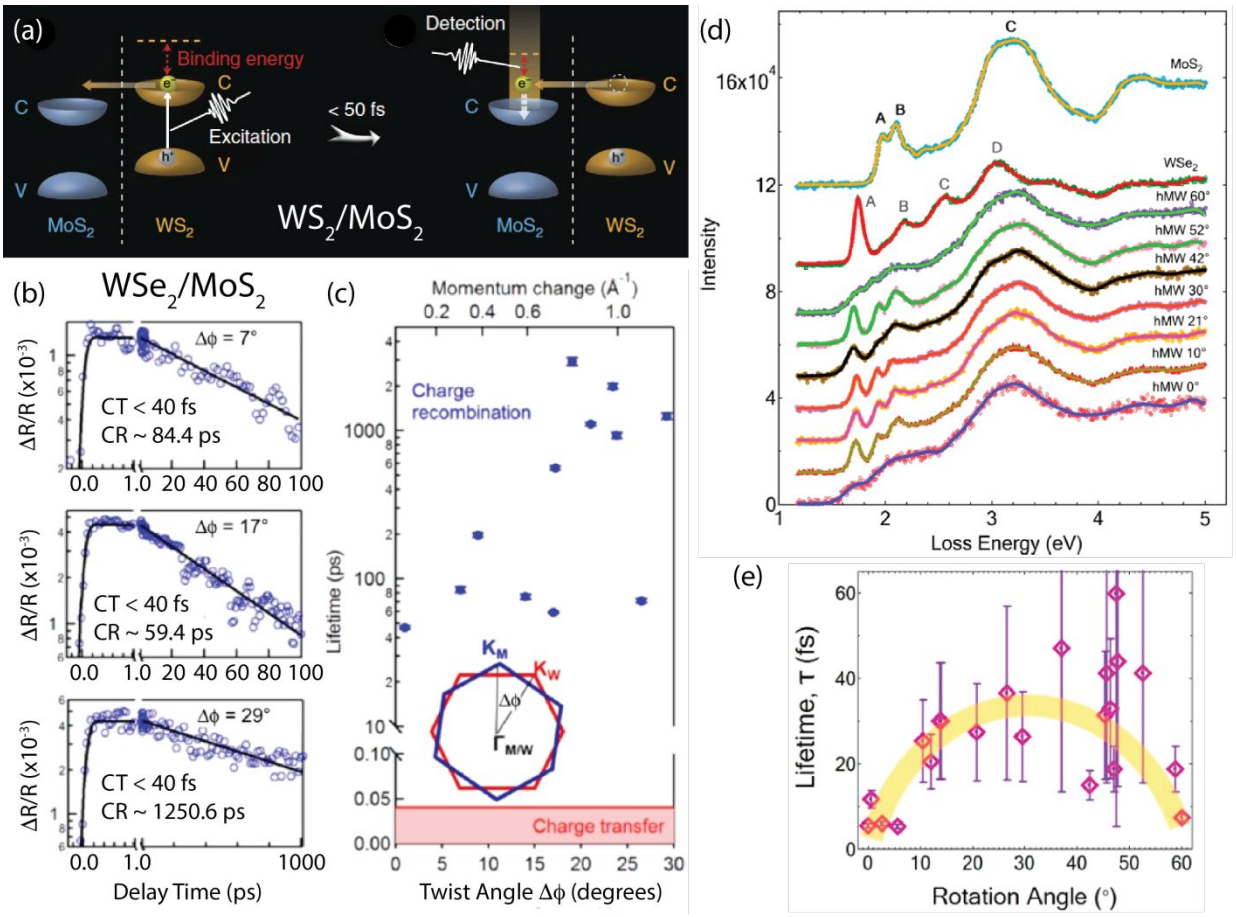

Figure 13. (a) Proposed hot exciton route for bypassing momentum mismatch in WS_2/MoS_2 hetero-bilayers. Rapid (<50 fs) electron transfer from WS_2 to MoS_2 initially produces a hot ILE that can be probed in the infrared before relaxing to form a cold ILE.[193] Reprinted by permission from Springer Nature from ref. 193. (b) Transient reflectance probing of photoinduced charge transfer (CT) and charge recombination (CR) for a WSe_2/MoS_2 bilayer, at varying twist angles ($\Delta\phi$).[195] (c) CT and CR lifetime as a function of $\Delta\phi$ (bottom axis) or momentum change (top axis) in WSe_2/MoS_2 bilayer. Inset: schematic depiction of twist angle in momentum space.[195] Panels (b) – (c) are reprinted with permission from ref. 195. Copyright 2017 American Chemical Society. (d) Rotation-angle-dependent electron energy loss spectra of excitonic transitions in WSe_2/MoS_2 bilayers.[196] (e) Rotation-angle-dependent lifetime (τ) of the WSe_2 A exciton in WSe_2/MoS_2 bilayers, as deduced from Heisenberg uncertainty analysis of EELS spectra shown in panel (d).[196] Panels (d) – (e) are reprinted with permission from ref. 196. Copyright 2019 American Chemical Society.

Zhu et al. studied the effect of the interlayer twist angle ($\Delta\phi$) on PCT and recombination dynamics in WSe_2/MoS_2 hetero-bilayers, where they measured the twist angle of mechanically stacked hetero-bilayers by the angular dependence of second harmonic generation (SHG).[195] The authors excited the WSe_2 layer at 710 nm and utilized transient reflectance to track electron transfer from WSe_2 to MoS_2 and subsequent charge recombination. Regardless of $\Delta\phi$, PCT occurred on an ultrafast time scale (<40 fs, Figure 13b). Although the recombination times varied significantly across the 12 different samples (from 47 ps to 3 ns), there was no clear correlation with $\Delta\phi$ (Figure 13c). In a conclusion that aligns with the hot exciton model of Chen,[194] the authors suggest that the excess energy available at the Type-II heterojunction allows electrons to circumvent momentum mismatch by sampling a wider range of K-space above the CB minimum, including the M point. Recombination lifetimes were insensitive to temperature, photoexcitation fluence, and gate-controlled carrier density, leading the authors to speculate that carrier recombination was dominated by defect-assisted (Shockley-Read-Hall) non-radiative recombination.

Another recent study took the unique approach of studying the effect of twist angle on the exciton absorption in MoS_2/WSe_2 hetero-bilayers using low-loss electron energy loss spectroscopy (EELS).[196] They observed that the intralayer absorption peaks were drastically broadened solely for 0° and 60° twist angles (Figure 13d). Using the analysis introduced by Rigosi et al.[170] (Section 8.1, Figure 9d-e), they interpret this broadening ($\Delta\Gamma$) within the framework of the Heisenberg uncertainty principle, $\tau = {\hbar}/{\Delta\Gamma}$, where broadened peaks arise from a shorter exciton lifetimes (τ). Assuming the decrease in exciton lifetime results primarily from PCT across the MoS_2/WSe_2 interface, the analysis shown in Figure 13e suggests that exceptionally fast charge transfer (τ < 10 fs) occurs for bilayers that are perfectly aligned ($\Delta\phi = 0°$) or anti-aligned ($\Delta\phi = 60°$). These results

suggest that, while misaligned TMDC hetero-bilayers still achieve very fast PCT on sub-100 fs timescales, near-perfect alignment can generate even faster rates (Figure 13e).

While standard optical studies (absorption, PL, TA, time-resolved PL—TRPL) can observe rapid charge transfer across TMDC heterojunctions, these studies are not *always* sensitive to the full progression of the exciton and charge carrier population in momentum space. For this reason, Liu and Zhu utilized time-resolved angle-resolved photoelectron spectroscopy (TR-ARPES) to probe the momentum dependence of the excited state population in a MoS_2/WS_2 hetero-bilayer produced by metal-assisted mechanical exfoliation.[197] To maintain valley polarization following PCT (e.g. valley-polarized ILEs, see also Section 8.4), interlayer coupling is needed for electron or hole transfer to the spin-polarized K or K' valley in the other TMDC without losing coherence *via* population transfer to other valleys. However, the wavefunctions at the K/K′ points are constructed primarily of in-plane metal atom d_{xy} and $d_{x^2-y^2}$ orbitals with little interlayer electronic interaction.[197] In contrast, first-principles calculations predict that the Q, M, and M/2 momentum points are comprised of mixed orbital character from each TMDC layer, resulting in much stronger interlayer interactions. Liu and Zhu show that PCT rates vary from momentum to momentum, where photoexcitation into the WS_2 K valley resulted in fast electron transfer to mixed-character M and M/2, valleys within ~70 fs, followed by slower population transfer to the MoS_2 K and mixed-character Q valleys over ~400 fs. This occurs because LO (longitudinal optical) phonon scattering is more prominent into M and M/2 than into Q, presumably due to the importance of energetic resonance for inter-valley scattering. Their results suggest that interlayer PCT is facilitated by phonon scattering into bands with mixed interlayer character, possibly explaining the general observation that ultrafast electron transfer depends little on the momentum mismatch associated with random twist angle between layers.

These intriguing results[197] suggest an intrinsic constraint to the *electron* valley polarization lifetime in TMDC/TMDC heterostructures. The near-degeneracy of the electron spin states in the CB at K/K′ suggests equal probability for scattering into K or K′, thus mixing the polarization of the resulting electron population in the acceptor. In contrast, the large VB spin-splitting suggests that the hole population is less prone to this phonon-scattering pathway for K/K′ valley depolarization. Therefore, the valley polarization lifetimes of holes should greatly exceed those of electrons. With this in mind, we turn to discuss the general strategy of using PCT to prolong the valley polarization lifetime.

8.4 Valley Polarization in PCT Events for TMDC/TMDC Heterostructures

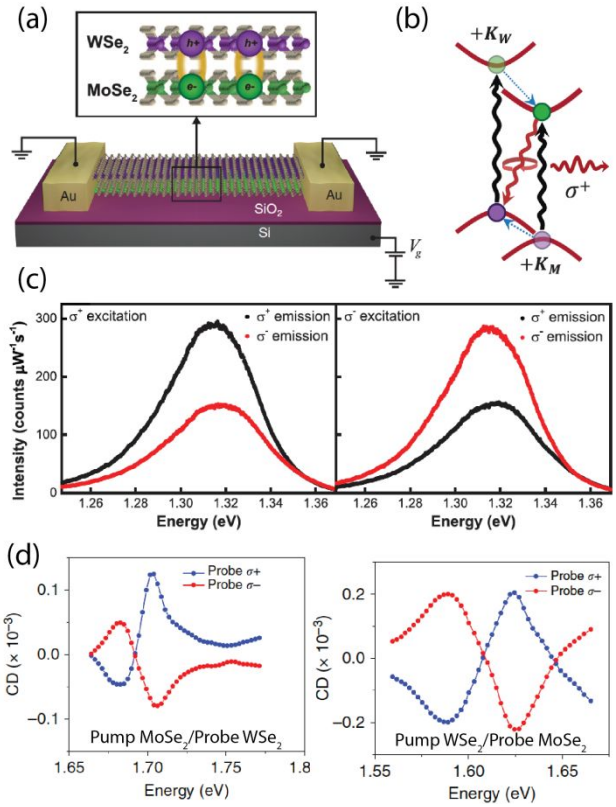

Figure 14. Valley polarized excitons in $MoSe_2/WSe_2$ hetero-bilayers. (a) Side view schematic of $MoSe_2/WSe_2$ heterostructure device, where photoexcitation produces electrons in the $MoSe_2$ layer and holes in the WSe_2 layer (inset).[109] (b) The resulting ILEs can be valley-polarized when generated with circularly polarized light (black wavy lines).[109] In the example given, fast interlayer charge transfer (blue dotted lines) forms the ILE in the +K valley. (c) Optical selection rules in the $+K_W$ and $+K_M$ valleys produce co-polarized PL for the ILE that can be modulated by the gate voltage (not shown).[109] Panels (a) – (c) are from Ref. 109. © The Authors, some rights reserved; exclusive licensee American Association for the Advancement of Science. (d) Pump-induced circular dichroism (CD) of the WSe_2 A exciton resonance when pumping $MoSe_2$ at 1.621 eV (left panel), and the $MoSe_2$ A exciton resonance when

pumping WSe_2 at 1.71 eV (right panel).[108] As expected for spin-valley polarization transfer in each charge transfer event, the CD response flips with probe helicity. Reprinted by permission from Springer Nature from ref. 108.

PCT across TMDC/TMDC heterojunctions can be an effective strategy for increasing the valley lifetime of valley-polarized carriers.[24, 108-109, 198] As discussed in Section 5, spin-valley locking should theoretically produce long valley lifetimes, since intervalley scattering requires both a large momentum change and a spin flip. For intra-layer excitons in most neat TMDC monolayers, however, valley polarization lifetimes are on the order of picoseconds.[15, 111-115] Thus, a number of recent studies utilize intelligently-designed TMDC/TMDC heterojunctions to facilitate (1) sustained valley polarization of the carriers residing on either side of the junction, and (2) long valley lifetimes due to spatial separation and reduced Coulomb attraction of the carriers.

For a mechanically stacked $MoSe_2/WSe_2$ bilayer, Rivera et al. utilized circularly polarized PL spectroscopy to determine the retention of initial valley polarization following interfacial PCT (Figure 14a-c).[109] At zero applied gate voltage, the authors found that 30 % of photons emitted by $MoSe_2^-/WSe_2^+$ ILEs retained the pump polarization. The loss of polarization was ascribed to valley depolarization of excitons on the femtosecond to picosecond timescale *preceding* PCT. The polarization percentage and lifetime were tuned by a gate voltage, with peak values around 40 % and 40 ns, respectively, at +60 V and 30 K. The long valley lifetime enabled spatial mapping of ILE drift-diffusion over micron length scales.

Schaibley et al. further studied $MoSe_2/WSe_2$ heterojunctions using transient reflectance (TR) spectroscopy to probe the retention of valley polarization following PCT.[108] The authors observed strong circular dichroism (CD) in the TR spectrum when pumping and probing with circularly polarized light, where the sign of the CD response flips upon changing the probe helicity (Figure 14d).[108] To characterize the degree of carrier valley polarization, the authors developed a detailed analysis that was further refined in the study by Kim et al. (see discussion below and

Figure 15).[24] Based on the TR spectra for the cases of co- and cross-polarized pump-probe pulses, the authors estimated 46% *electron* spin-valley polarization in the $MoSe_2$ layer following hole transfer to WSe_2. The retention of spin-valley polarization did not depend on twist angle.

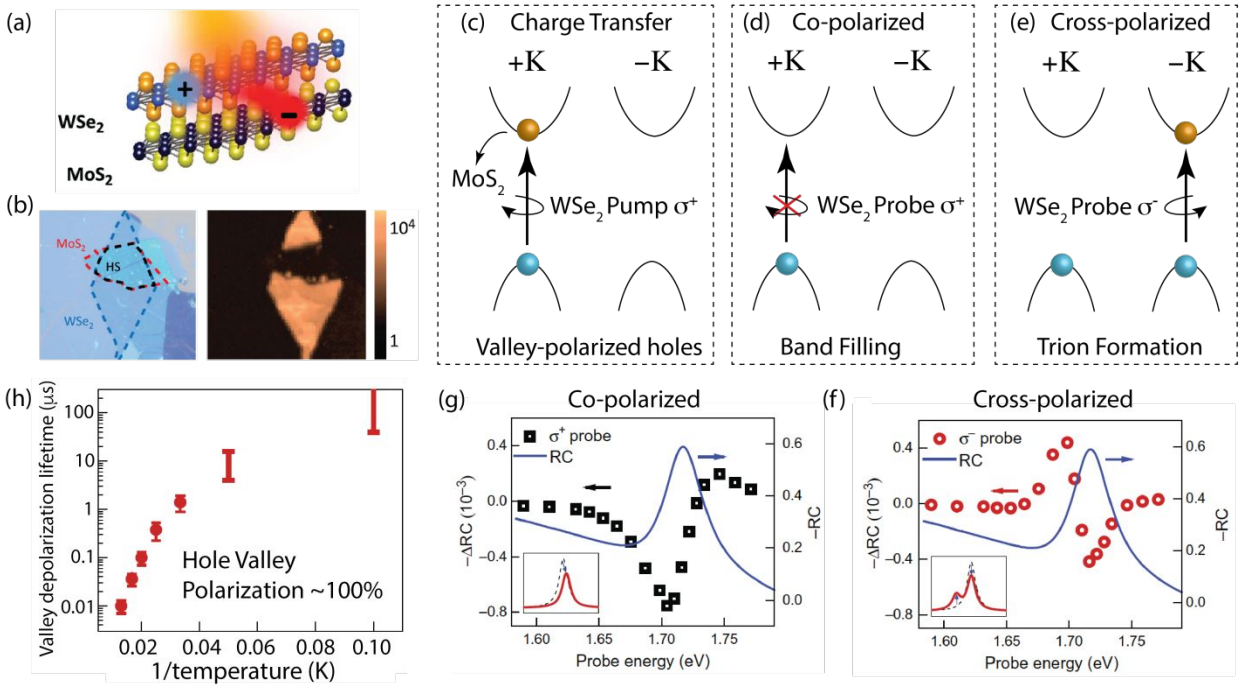

Figure 15. Long-lived hole valley polarization in WSe_2/MoS_2 hetero-bilayer. (a) Schematic of WSe_2/MoS_2, where photoexcitation produces electrons in MoS_2 and holes in WSe_2.[24] (b) Optical microscope image of heterostructure, where MoS_2, WSe_2, and the heterostructure are outlined with red, blue, and black dashed lines, respectively. Panels (c) through (e) summarize the expected sequence of events in the pump-probe measurements. (c) σ^+ photons create valley-polarized excitons in WSe_2. Rapid (<50 fs) electron transfer to MoS_2 leaves valley-polarized holes in WSe_2. (d) For co-polarized probe, holes remaining in the WSe_2 K^+ valley reduce exciton oscillator strength in the K^+ valley (band filling, arrow shown for σ^+ probe photons) and lead to a blue shift of the exciton transition (Moss-Burstein effect, not depicted). (e) For cross-polarized probe, σ^- probe photons create intervalley trions, transferring oscillator strength from the exciton transition to the trion transition. (f) and (g) Experimental results for the cross-polarized and co-polarized pump-probe configurations, respectively, for the WSe_2/MoS_2 bilayer. The blue lines in each figure show the reflectance contrast (RC) of the heterostructure, for comparison. Insets in panels (f) and (g) depict the expected spectral responses for these probe configurations, as outlined in panels (d) and (e). (h) shows ~100% hole valley polarization for the WSe_2/MoS_2 interface at 10 K. Panels (a), (b), (f), (g), and (h) from Ref. X.

Although Schaibley et al. were unable to determine *hole* polarization yields in their $MoSe_2/WSe_2$ heterojunctions due to overlapping TR spectral signatures,[108] Kim et al. demonstrated near-unity valley polarization and microsecond timescale valley lifetimes for WSe_2 holes in WSe_2/MoS_2 heterojunctions.[24] These combined results are consistent with the micro-

ARPES study discussed in Section 8.3 that suggested rapid decoherence of the electron valley polarization *via* phonon scattering,[197] which is not expected to strongly affect the hole population. Kim et al. demonstrated that 50 fs PCT time out-competed *intralayer* exciton valley depolarization in WSe_2/MoS_2, resulting in generation of perfectly valley-polarized carriers. The authors attributed the ultralong valley lifetimes of holes to carrier separation in real space *and* momentum space, which increases the recombination time and decreases the propensity of intervalley scattering mechanisms,[76, 199-201] such as the intervalley electron-hole exchange mechanism proposed by Maialle, Silva, and Sham.[202] This analysis relied on distinguishing between holes in the K versus K' valleys, where the authors measured different TA spectra following co-polarized or cross-polarized pump-probe measurements as shown in Figure 15c-e. The K-valley hole quenches and blue-shifts the exciton transition, due to a combination of phase-space filling and the Moss-Burnstein effect (Figures 15d and 15g). In contrast, the K′ valley does not experience phase-space filling and instead the probe pulse predominantly excites intervalley trions (Figures 15e and 15f). Using the analysis first demonstrated by Schaibley et al.,[108] the authors quantified near-unity K valley polarization with a temperature-dependent lifetime exceeding 100 μs at 10 K (Figure 15h).

8.5 TMDC Hetero-Trilayers

A number of groups have begun exploring complex multi-layer heterostructures to exert greater control over charge transfer directionality and charge separation lifetime. Ceballos and co-workers expanded upon their initial bilayer studies[171] by inserting a WS_2 monolayer in between MoS_2 and $MoSe_2$ monolayers, producing a mechanically exfoliated and stacked tri-layer with a "cascading" band alignment (Figure 16a).[203] The proposed band alignment should foster electron transfer from $MoSe_2$ to WS_2 to MoS_2 and hole transfer in the opposite direction, ultimately funneling electrons to MoS_2 and holes to $MoSe_2$. Indeed, selective excitation of the low-bandgap

$MoSe_2$ layer led to bleaching at the MoS_2 A exciton, with 1.5 +/- 0.2 ps electron transfer time (Figure 16b). Further experiments suggested that hole transfer occurred on a ~300 fs time scale.

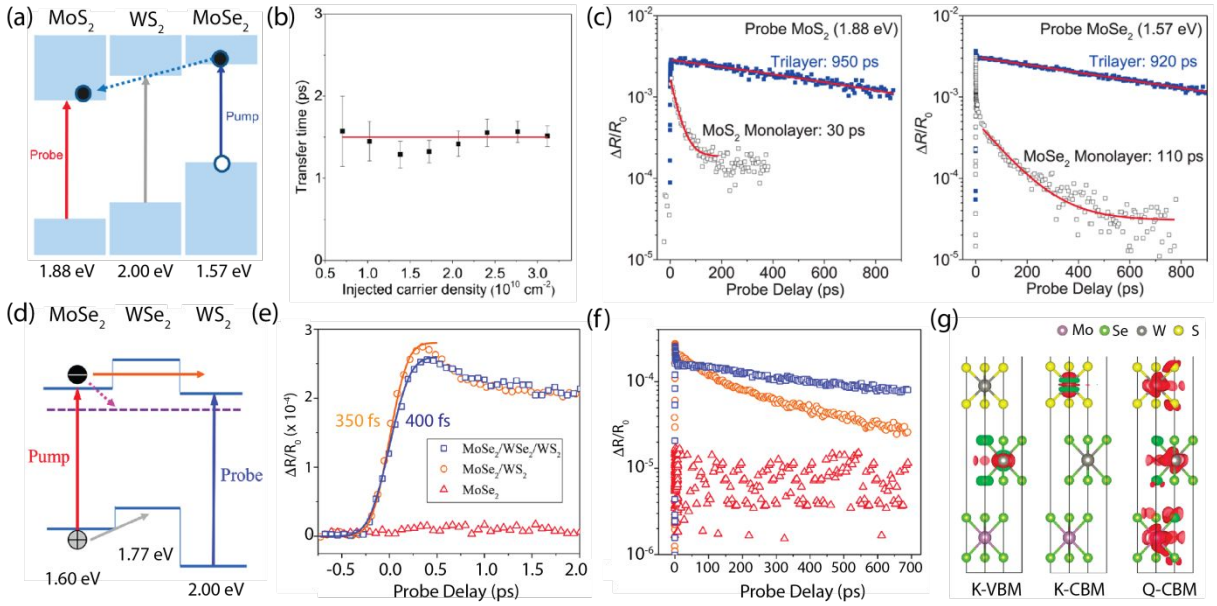

Figure 16. Photoinduced charge transfer in TMDC hetero-trilayers. (a) Band alignment of a $MoSe_2/WS_2/MoS_2$ trilayer, along with pump-probe details for transient reflectance study.[203] (b) Charge transfer time for same trilayer as a function of carrier density injected by pump pulse.[203] (c) Reflectance transients for trilayer sample (blue solid squares), probed at either 1.88 eV (left panel, MoS_2 optical bandgap) or 1.57 eV (right panel, $MoSe_2$ optical bandgap) after photoexcitation of $MoSe_2$ at 1.57 eV. Open symbols are transients for a MoS_2 monolayer with same probe energies, but pumped at 3.14 eV.[203] Red curves are exponential fits. Panels (a) – (c) are reprinted with permission from ref. 203. Copyright 2017 American Chemical Society. (d) Transient reflectance pump-probe configuration for a $MoSe_2/WSe_2/WS_2$ trilayer. A 1.60 eV pump pulse excites excitons in $MoSe_2$. Holes are expected to transfer to WSe_2 (gray arrow), while electrons may tunnel to WS_2 (orange arrow) or transfer to (pink arrow) layer-coupled states (dashed line). Electrons making it to WS_2 are probed by a 1.97 eV probe pulse.[204] (e) and (f) Differential reflection signal measured from the trilayer in different sample regions: $MoSe_2/WSe_2/WS_2$ (blue squares), $MoSe_2/WS_2$ (orange circles), and $MoSe_2$ (red triangles).[204] (g) Charge densities for trilayer in $MoSe_2$ (bottom), WSe_2 (middle), and WS_2 (top) for the VBM and CBM at the K- and Q-points.[204] The proposed delocalized layer-coupled states at the Q-point are theorized to facilitate ultra-fast charge transfer from $MoSe_2$ to WS_2. Panels (d) – (g) are reprinted with permission from ref. 204. Copyright 2018 American Chemical Society.

Following PCT, the lifetimes of separated charges (e^- in MoS_2 and h^+ in $MoSe_2$, $\tau \approx 920 – 950$ ps) was roughly an order of magnitude longer than the excited-state lifetimes in either neat monolayer ($\tau \approx 30 – 110$ ps), as shown in Figure 16c. The authors suggest that the extended lifetimes result from better spatial separation of charges than can be achieved in bilayer TMDC heterojunctions. Interestingly, the authors observed only a weak ground state bleach signal in the central WS_2 layer when $MoSe_2$ was excited. Based on control experiments on a WS_2 monolayer,

the authors concluded that this WS_2 bleach was too weak to arise from electrons temporarily populating the WS_2 conduction band during a stepwise charge transfer from $MoSe_2$ to WS_2 to MoS_2. The authors suggested coherent electron transfer from $MoSe_2$ to MoS_2, which they supported with nonadiabatic molecular dynamics simulations.

The same group studied another TMDC tri-layer ($MoSe_2/WSe_2/WS_2$) in which the band structure did not facilitate a "cascading" electron or hole transfer pathway from one side of the tri-layer to the other, as shown in Figure 16d.[204] In this case, exciting the low-bandgap $MoSe_2$ layer should transfer holes to the middle WSe_2 layer, while electrons have an energetic barrier for transfer to either WSe_2 or WS_2. Surprisingly, photoexcitation of $MoSe_2$ at 1.60 eV led to an ultrafast rise of the WS_2 ground-state bleach near 2.0 eV in the TA experiment (Figure 16e). The rise time of the WS_2 GSB was similar to the rise time observed in a $MoSe_2/WS_2$ bilayer, where electron transfer occurs over < 350 fs from photoexcited $MoSe_2$ to the WS_2 layer. Tunneling probability calculations suggested that the ultrafast time scale of electron transfer from $MoSe_2$ to WS_2 in the tri-layer sample did *not* correspond to tunneling through the intervening WSe_2 barrier (orange arrow, Figure 16d). Instead, the authors suggest formation of layer-coupled electronic states (purple dashed line, Figure 16d) that are lower in energy than the lowest-energy states at the K point that define the optical transitions of the isolated monolayers. The DFT calculations shown in Figure 16g suggested that the CBM at the Q-point (~100 meV below the K-valley in energy) was delocalized over all three monolayers in the tri-layer system, lending support to layer-coupled states facilitating ultrafast electron transfer from $MoSe_2$ to WS_2. The lifetimes of the resulting charges (hole in WSe_2 and electron in WS_2 or $MoSe_2$) were substantially longer than the lifetimes observed for either isolated monolayers or bilayers with the same charge population (Figure 16f).

8.6 Lateral TMDC/TMDC Heterojunctions

All of the TMDC/TMDC heterojunctions discussed so far are *vertical heterojunctions* where individual TMDC layers are grown or stacked on top of one another. *Lateral heterojunctions* (Figure 17) can also be fabricated by vapor phase synthesis routes (Figure 17a – 17c), whereby an atomically sharp or more gradual (alloyed) interface is formed between the two TMDCs within the lateral plane of a single crystal structure.[205-213] The atomic sharpness of the interface can be imaged by aberration-corrected and/or Z-contrast scanning transmission electron microscopy (Figure 17b), and the individual layers can also be spatially mapped over larger areas using PL (Figure 17c) and Raman (Figure 17d) mapping.

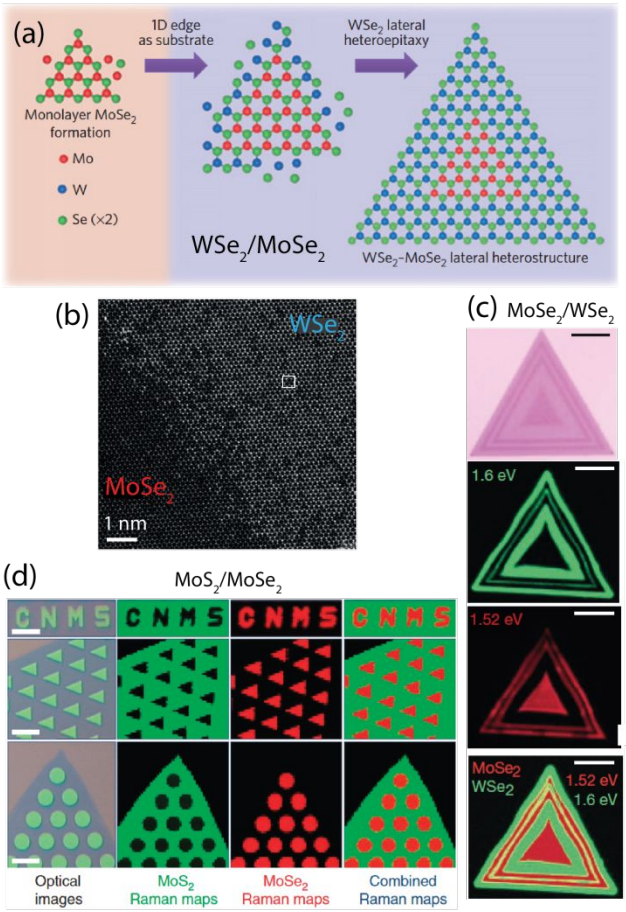

Figure 17. (a) Schematic illustration of in-plane epitaxial growth process for exemplary lateral $WSe_2/MoSe_2$ heterostructure.[207] (b) High-resolution ADF STEM image of an interface between $MoSe_2$ (darker) and WSe_2 (lighter). Scale bar, 2 nm.[207] Panels (a) – (b) are reprinted by permission from Springer Nature from ref. 207. (c) Photoluminescence intensity maps for WSe_2 (1.6 eV, top) and $MoSe_2$ (1.52 eV, middle) domains, and composite PL map (bottom) of a lateral $WSe_2/MoSe_2$ heterojunction.[213] Reprinted by permission from Springer Nature from ref. 213. (d) Optical images (left-most panels) and Raman mapping images (other panels) of lateral $MoS_2/MoSe_2$ heterojunction arrays formed within monolayer crystals by patterning and selective conversion process. In Raman

images, green areas correspond to MoS_2 (403 cm^{-1}) and red areas correspond to $MoSe_2$ (238 cm^{-1}).[209] Reprinted by permission from Springer Nature from ref. 209.

An interesting consideration is the degree to which lateral TMDC/TMDC heterojunctions retain the Type-II band alignment that is present in the same vertical heterostructure. Calculated band alignments can deviate significantly between vertical and lateral heterojunctions.[214-216] This difference results in lateral heterostructures tending to have significantly lower Δ_{CBO} and Δ_{VBO} relative to their vertical counterparts (see Figure 8).[208, 215-216] Calculations by Gong et al. suggest that, for the monolayer MoS_2/WS_2 lateral heterojunction, Δ_{CBO} is ~0 meV and Δ_{VBO} is ~70 meV.[208] This contrasts with the large Δ_{CBO} (930 meV) and Δ_{VBO} (720 meV) in vertical MoS_2/WS_2 from scanning tunneling spectroscopy (Figure 8a).[166] Similarly, Guo et al. highlight vertical MoS_2/WSe_2 junctions for which theory and experiment suggest very large Δ_{CBO} and Δ_{VBO} (Figure 18a, ~830 meV and ~760 meV, respectively),[165, 215] in contrast to <200 meV Δ_{CBO} and Δ_{VBO} in lateral heterojunctions.[215] Calculations by Yang et al. similarly suggest that both Δ_{CBO} and Δ_{VBO} nearly disappear in lateral junctions.[216]

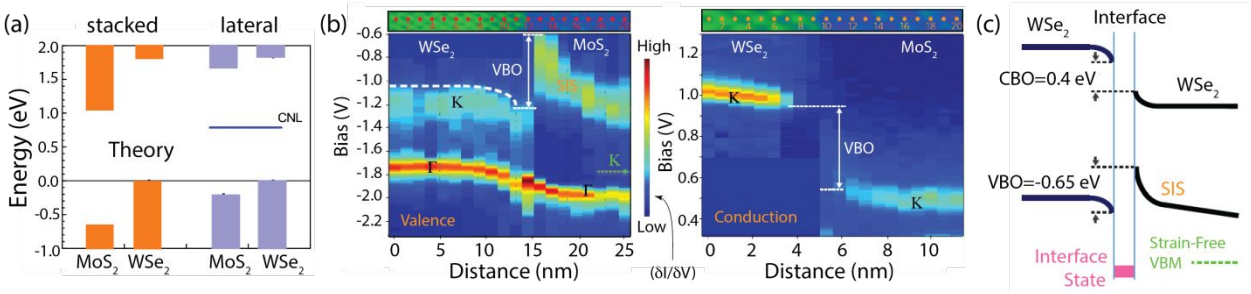

Figure 18. (a) Comparison of DFT-calculated band alignments for MoS_2/WSe_2 heterojunction, in the stacked (vertical) or lateral configuration.[215] CNL refers to charge-neutrality level. Reprinted from ref. 215, with the permission of AIP Publishing. (b) Differential current (δI/δV), as measured by scanning tunneling spectroscopy, for the valence band (left) and conduction band (right) of WSe_2/MoS_2 lateral heterojunction. VBO and CBO are the valence band and conduction band offsets, respectively, and SIS denotes strain-induced states.[217] (c) Type-I band alignment at the lateral WSe_2/MoS_2 interface deduced from scanning tunneling spectroscopy measurements.[217] Panels (b) – (c) are reprinted by permission from Springer Nature from ref. 217.

Recent experimental evidence lends credence to the predictions that the Type-II band alignments observed for vertical hetero-bilayers do not necessarily translate to Type-II alignment for lateral junctions. Zhang et al. used scanning tunneling spectroscopy/microscopy to directly

image the interfacial strain and band alignment in a MoS_2/WSe_2 lateral heterojunction.[217] Their measurements suggest that interfacial strain imparts significant band bending at the interface, resulting in a Type-I band alignment with large Δ_{CBO} and Δ_{VBO} (Figure 18b-c). This alignment differs remarkably from the Type-II alignment observed for the MoS_2/WSe_2 vertical heterojunction using the same technique (Figure 8b).[165]

Differences in Δ_{CBO} and Δ_{VBO} between vertical heterojunctions and lateral heterojunctions will likely have significant impact on PCT and carrier recombination. For example, theoretical studies suggest that lack of Type-II band alignment in MoS_2/WSe_2 lateral junctions leads to accelerated recombination dynamics compared to vertical heterojunctions (Figure 19a).[216] For the lateral junctions, Yang et al. found that the electron wave function was localized at the interface region between WSe_2 and MoS_2, and the hole was localized in WSe_2 close to the interface. The authors concluded that the highly localized exciton-like state at the lateral interface recombined significantly faster (191 ps) than in the vertical heterojunction (496 ps).

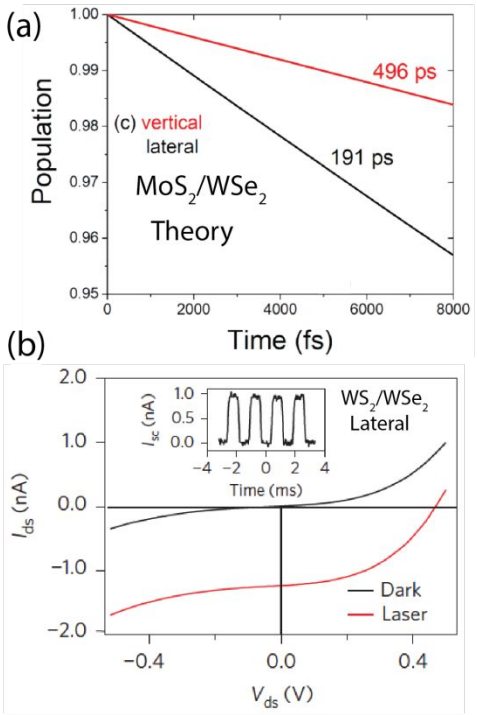

Figure 19. (a) Calculated electron-hole recombination times for vertical (red) and lateral (black) MoS_2/WSe_2 heterojunctions.[216] Reprinted with permission from ref. 216. Copyright 2017 American Chemical Society. (b) Current-voltage (I_{ds}-V_{ds}) output of lateral WSe_2/WS_2 heterojunction p-n diode in the dark (black line) and under illumination (red line; 514 nm, 30 nW power).[206] Reprinted by permission from Springer Nature from ref. 206.

Experimental studies of PCT across lateral TMDC/TMDC heterojunctions are still sparse. Bellus et al. report that the Type-I band alignment at the lateral $MoS_2/MoSe_2$ interface leads to ultrafast photoinduced *energy transfer* from MoS_2 to $MoSe_2$,[212] as opposed to the evidence of *charge transfer* and Type-II alignment observed by the same authors for the vertical $MoS_2/MoSe_2$ heterostructure.[171] Spatial PL measurements of lateral MoS_2/WS_2 heterojunctions demonstrated strong interface-localized enhancement of PL, at energies intermediate between the MoS_2 and WS_2 monolayer emission peaks, suggesting preferential recombination at the interface, in contrast to the near-infrared ILE observed for the same TMDCs in a vertical heterojunction.[208]

Despite these possible differences between vertical and lateral heterojunctions, some promising device results have been observed for lateral junctions. Duan et al. have shown rectifying p-n diodes for CVD-grown lateral WS_2/WSe_2 heterojunctions with a clear photovoltaic effect (Figure 19b),[206] and others have also observed varying degrees of PV effects in lateral heterostructures.[208, 213, 218] Several groups are working towards creating lateral heterostructures with more complex degrees of carrier/exciton localization, such as the lateral WS_2/WSe_2 quantum-well superlattices grown by Zhou et al.[211] Looking forward, there is clearly much more to learn about the band alignment within lateral TMDC heterostructures. The exact alignment likely depends on a host of factors, including carrier density and type in each layer, the degree of sharpness or alloying at the junction, the presence and density of interfacial defects, substrate effects, and more. As such, this area is ripe for future exploration, both for understanding and rationally tuning in-plane band alignment and for understanding the effects of this alignment on PCT.

9. TMDC Heterojunctions with Organic Semiconductors

Several complementary relationships exist between organic semiconductors (OSCs) and TMDCs, making heterojunctions between these classes of materials particularly attractive. For example, extensive work on intelligent molecular design has led to an impressive range of OSCs where the band gap, morphology, and the energy level alignment can be tuned by small chemical or processing variations.[39, 219-222] This OSC toolset can be employed to engineer functional TMDC heterojunctions with optimized interfacial charge separation. Additionally, OSCs offer strong optical absorption to increase photon harvesting, surfaces free of dangling bonds, and small spin-orbit coupling that could possibly facilitate retention of selective spin-valley excitations in TMDC-based spintronics. On the other hand, some OSCs tend to have low carrier mobilities, making the higher mobilities in TMDCs particularly beneficial for optimizing carrier separation and collection. Depositing organics onto TMDCs may also have unique benefits of inducing ordered structure in the organic molecules due to the TMDC-organic surface interactions.[223-224]

TMDC/organic interfaces have been investigated in several different contexts, such as using organics as TMDC surface treatments to passivate defects,[225-228] using organics for p-type or n-type doping of TDMCs,[229-231] or using thicker organic films to form TMDC/organic charge separating heterojunctions where both the molecular and TMDC layers are active components.[79, 81, 232-234] Here, we focus primarily on the case of PCT at TMDC-based heterojunctions, because this is a central component for future device applications including solar fuel generation, photocatalysis, photovoltaics, photodiodes, and phototransistors. We highlight TMDC/organic heterojunctions employing small molecules, carbon nanotubes, or polymers.

9.1 Photoinduced Charge Transfer at TMDC/Molecular Semiconductor Interfaces

PCT has been demonstrated in several TMDC/molecular systems, predominately including heterojunctions with phthalocyanines,[81, 226, 235-239] porphyrins,[240] acenes,[79, 232-233, 241-242] perylenes,[243-245] and fullerenes.[246-247] The competitive process of energy transfer has also been studied in heterojunctions with organic dyes.[248] While the optimization of carrier generation in TMDC/molecular heterojunctions is still in a nascent stage, molecular organic (small molecule) semiconductors are particularly attractive candidates for model systems to enable more detailed understanding of TMDC-based heterostructures. For example, in comparison to polymers, small molecules offer rigid and well-defined molecular units that can pack into lattice structures with potentially less disorder and more easily defined morphologies.[249] As we describe here, several examples exist where molecular control has played an important role in elucidating fundamental properties of TMDCs and TMDC/organic interfaces.[236]

9.1.1 Charge-Transfer Driving Force and Molecular Morphology

A crucial initial step for designing TMDC-based heterojunctions that exhibit interfacial charge transfer is proper energy level alignment to achieve sufficient driving force (ΔG) for PCT, as described in Sections 2 – 3 and Equations 4 – 6. As an example of ΔG_{CT} values in organic/TMDC heterojunctions, Table 3 shows estimated driving forces for electron transfer and hole transfer between a range of popular semiconducting molecules that could form a Type-II heterojunction with monolayer MoS_2. In practice, only a few of the molecules in Table 3 have been employed in organic/TMDC heterojunctions, and the actual IP_D, $EA_{A,}$ and $\Delta G_{ET/HT}$ values will vary depending on the substrate and sample characteristics.

Table 3. Estimated values for the driving force of electron transfer (ΔG_{ET}) and hole transfer (ΔG_{HT}) for a range of organic molecules that could act as electron donors in Type-II heterojunctions with monolayer MoS_2. References indicate the source of ionization potentials used in Equation 6, and MoS_2 electron affinity values were averaged from Refs. [12, 81, 215, 250] ($EA_{MoS2} \approx$ -4.1 ±0.1 eV) .

Organic Electron Donor	ΔG_{ET} (eV)	ΔG_{HT} (eV)
(6,5) SWCNT [163, 251]	0.02	-0.62

(7,5) SWCNT [46]	0.02	-0.67
(9,7) SWCNT [46]	0.14	-0.84
(11,9) SWCNT [46]	0.20	-0.94
$PC_{60}BM$ [252]	-0.29	-0.14
$PC_{70}BM$ [252]	-0.38	-0.12
ITIC [253]	0.01	-0.27
Pentacene (lying) [254]	-1.73	-1.16
Pentacene (standing) [254]	-1.25	-0.68
CuPc (lying) [255-256]	-0.48	-0.76
CuPc (standing) [255-256]	-1.04	-1.32
ZnPc [257]	-0.41	-0.74
SubPc [258]	-0.88	-0.45
SubNc [258]	-0.67	-0.67
α-6T [258]	-2.10	-1.17
Ruberene [252]	-1.54	-0.72
DTDCTB [259]	-0.27	-0.75
d-DTS$(PTT_2)_2$ [260]	-1.04	-1.22
p-DTS$(FBTT_2)_2$ [260]	-1.04	-1.22

The *IP* and *EA* values for molecular semiconductors can depend on molecular orientation, as indicated by the differing ΔG_{CT} values in Table 3 for lying (horizontally stacked) versus standing (vertically stacked) CuPc and pentacene. This opens opportunities for tuning the charge transfer yields and rates through modifying molecular packing and morphology. Changing morphology in the organic layer also affects the efficiency of free-carrier generation by varying the extent of carrier delocalization.[236] Indeed, Padgaonkar et al. has demonstrated that molecular orientation plays an important role in extending carrier lifetimes in TMDC/phthalocyanine (Pc) heterojunctions.[236] The authors found that face-on stacking of CuPc molecules facilitates hole diffusion away from the interface, extending charge separation up to 70 ns.[236] This long lifetime of separated carriers contrasts with the shorter sub-nanosecond decays in TMDC/H_2Pc heterojunctions, where the mix of edge-on and face-on H_2Pc orientation is suggested to yield inferior charge diffusion.[236] Theoretical calculations also support more efficient charge transfer at TMDC/Pc interfaces with face-on orientation.[237] In perylene systems, it has also been suggested that alkyl chain length can contribute to the molecular tilt angle on MoS_2 surfaces, which could

affect charge-transfer dynamics.[245] While charge generation and band bending has been investigated in perylene/MoS_2 systems,[243] establishing a link between molecular orientation and charge carrier kinetics in these systems requires additional characterization.

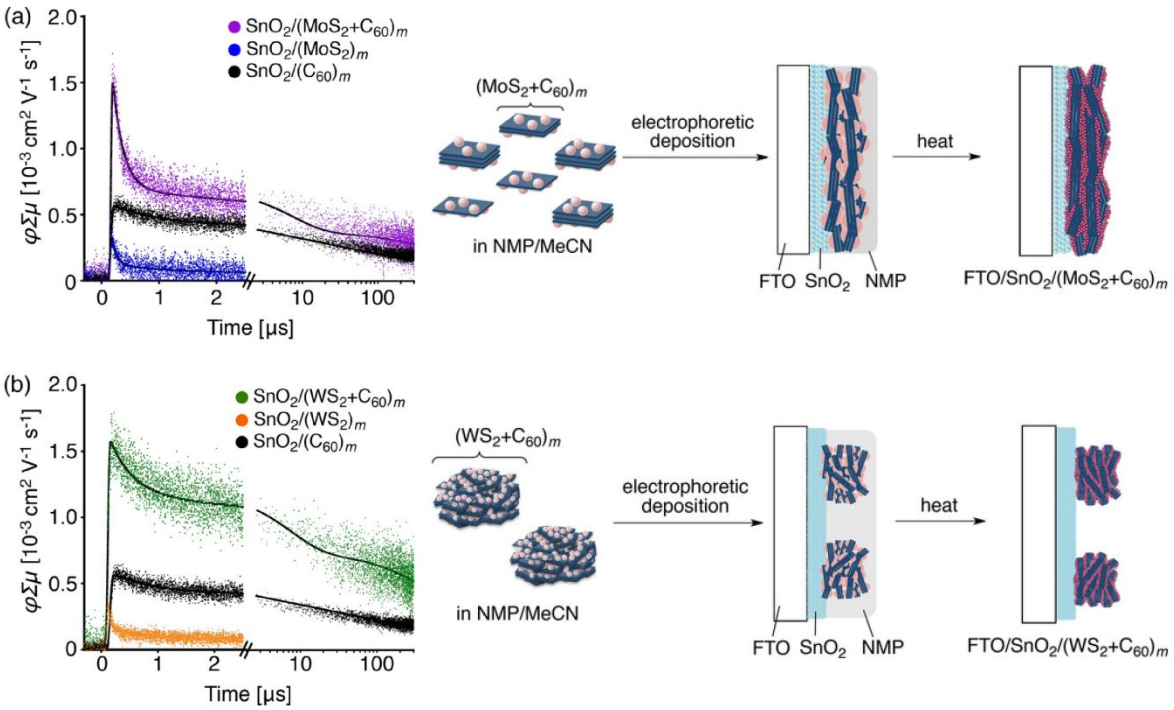

Figure 20. Transient photoconductivity ($\phi\Sigma\mu$), in which ϕ is the charge-separation quantum efficiency and $\Sigma\mu$ is the sum of carrier mobilities measured for (a) MoS_2/C_{60} composites on SnO_2 versus (b) WS_2/C_{60} composites on SnO_2, where heterojunction formation via solution self-assembly is schematically illustrated for each material. This figure is modified from Reference [246]. Reprinted with permission from ref. 246. Copyright 2018 Wiley.

In addition to controlling alignment and stacking orientation when molecules are deposited onto TMDCs, Figure 20 highlights another promising strategy for optimizing TMDC/organic interfacial contact using a 'one-pot synthesis' with self-assembly in solution.[246] In this process, rapid injection of a poor solvent (acetonitrile, MeCN) into a good solvent (N-methyl-2-pyrrolidone, NMP) containing the TMDCs and fullerenes yields TMDC-C_{60} aggregates that form due to a combination of the lyophobic effect and strong van der Waals interactions. Interestingly, the authors observed different aggregate formation behavior between MoS_2/C_{60} and WS_2/C_{60} structures, as schematically depicted in Figure 20. They hypothesize that larger WS_2/C_{60}

composites form in the NMP/MeCN solution due to a stronger attractive interaction between WS_2 and C_{60} (calculated as -0.97 eV)[261] compared to MoS_2 and C_{60} (calculated as -0.84 eV)[261]. The authors observed evidence for free carrier generation in these systems using time-resolved microwave conductivity (TRMC), which showed higher photoconductivity and longer carrier lifetimes for the heterojunctions compared to the neat materials. It should be noted, however, that a significant portion of the TRMC signal in this case is due to interactions with SnO_2 nanoparticles in addition to the TMDC-fullerene hybrid structures. Charge transfer was further evidenced by a photoelectrochemical response in both heterostructures, with an incident photo-to-current efficiency (IPCE) at 400 nm of 35% for FTO/SnO_2/(MoS_2+C_{60}) and 23% for FTO/SnO_2/(WS_2+C_{60}), where FTO is fluorine-doped tin oxide.

9.1.2 Charge-Transfer States

Even in systems with sufficient driving force for charge generation, opposite charge carriers often remain Coulombically bound at TMDC/organic interfaces due to spatial confinement and low dielectric screening, which can result in interfacial charge-transfer states with binding energies in the range of tens to hundreds of meV.[79, 244] Charge-transfer states at TMDC/organic interfaces have been demonstrated by emergence of sub-gap absorption features, as illustrated in Figure 21a.[235] In this case, the strong charge-transfer absorption peak is attributable to high oscillator strength for direct excitation of interfacial excitons across CuPc/MoS_2 interfaces, and the authors demonstrated similar sub-gap absorption peaks for a range of metal-center and metal-free phthalocyanines. The authors found that these charge-transfer states are primarily comprised of the π-character phthalocyanine HOMOs and the TMDC conduction band, so the peak energy of charge-transfer state absorption only weakly depends on the phthalocyanine metal center. However, the small shift observed in the charge-transfer state energy follows a trend based on the

phthalocyanine's non-frontier (HOMO-1) metal d-orbitals, suggesting enhanced orbital mixing occurs with closer energy alignment between the HOMO-1 and the MoS_2 valence band. This example demonstrates the promise of small variations in molecular structure for tuning interactions at organic/TMDC interfaces.

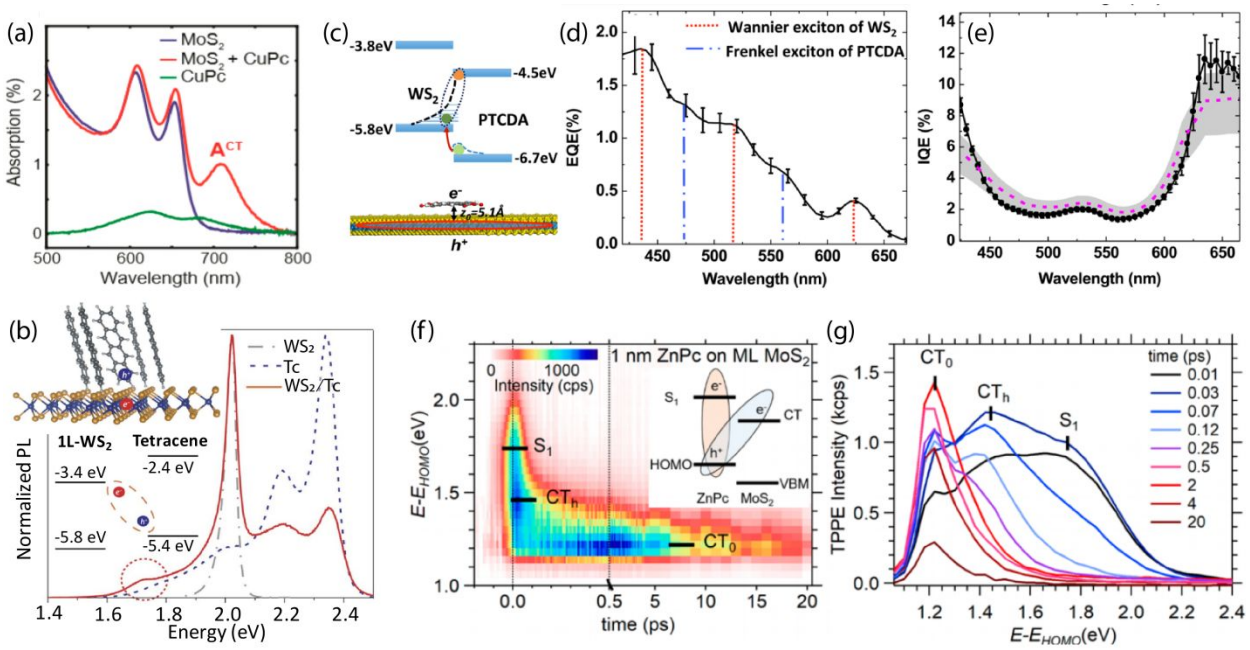

Figure 21. (a) Strong sub-gap charge-transfer state absorption in MoS_2/CuPc heterojunctions;[235] Reprinted with permission from ref. 235. Copyright 2019 American Chemical Society. (b) Evidence of charge-transfer state photoluminescence (PL) around 1.7 eV in WSe_2/tetracene heterojunctions;[79] From from Ref. 79. © The Authors, some rights reserved; exclusive licensee American Association for the Advancement of Science. (c) Illustration of energy level offsets, charge transfer, and delocalization at PTCDA/WS_2 heterojunctions;[244] (d) External quantum efficiency (EQE) for PTCDA/WS_2 where vertical lines indicate excitation of predominately WS_2 (red) or PTCDA (blue);[244] (e) Internal quantum efficiency (IQE) for PTCDA/WS_2;[244] Panels (c) – (e) are reprinted with permission from ref. 244. Copyright 2017 American Chemical Society. (f and g) Time-resolved two-photon photoemission TPPE) showing evolution of photoluminescence from ZnPc singlet exciton (S_1) to hot charge-transfer states (CT_h) to relaxed charge-transfer states (CT_0) in ZnPc/monolayer-MoS_2 heterojunctions.[81] Panels (f) – (g) are reprinted with permission from ref. 81. Copyright 2019 American Chemical Society.

Similar to the ILEs at TMDC/TMDC heterojunctions, interfacial charge-transfer states at TMDC/organic heterojunctions can be characterized by emission peaks at lower energies compared to the neat materials' photoluminescence. Figure 21b shows sub-gap luminescence at 1.7 eV from charge-transfer states in a 1L-WS_2/tetracene heterojunction.[79] The charge-transfer emission was longer-lived than the exciton lifetimes of either separate neat material, with a

stretched-exponential decay giving an average lifetime of 2.1 ns. The authors attributed the dispersion of the decay time constant (i.e. the stretching exponent in their fit of the charge-transfer lifetime) to a distribution of different charge-transfer state configurations. Using transient absorption microscopy, the authors measured diffusion of charge-transfer states away from the optical excitation. They fit their data to two diffusion constants of ~1 cm^2s^{-1} and ~0.4 cm^2s^{-1}, and they attributed the slower-moving population to trapped, low-energy charge-transfer states. They estimate these localized charge-transfer states to be ~10 meV lower energy than the delocalized states, suggesting that trapping/de-trapping at room temperature likely contributes to the stretched-exponential lifetime and broad emission profile for charge-transfer states at these heterojunctions.

As demonstrated by this WS_2/tetracene study,[79] as well as by extensive investigations of this topic in organic heterojunction systems,[39, 178-179] understanding the equilibrium between localized and delocalized charge-transfer states is essential for optimizing free-carrier generation. However, the spatial nature of charge-transfer states at organic/TMDC interfaces differs from organic-only heterojunctions, particularly due to the significant asymmetry of carrier polarizability and delocalization on either side of the heterojunction. For example, Liu et al. addressed the implications of more confined Frenkel excitons generated in the organic layer versus Wannier-Mott excitons generated in the 2D TMDC layer for a perylene (PTCDA)/WSe_2 system (Figure 21c – e).[244] They found that the differing degree of delocalization between the two layers results in an asymmetric charge-transfer state that can be modeled as a point charge in the organic that is bound to a hole with high in-plane delocalization in the TMDC (Figure 21c). They calculated 38.2 meV binding energy for the charge-transfer state, suggesting that it is stable at room temperature. Using this heterojunction in a device, the authors observed higher internal quantum efficiency (IQE) upon TMDC excitation as shown in Figure 21e. They attributed the higher IQE to greater exciton

dissociation when exciting delocalized states in the TMDC layer (~80%, from PL quenching) in comparison to the organic layer (~12%) that relies on exciton diffusion to the interface. Since the IQE is equal to the exciton quenching efficiency (from PL) multiplied by the charge-transfer state dissociation at the interface (η_{diss}) and subsequent charge collection (η_{CC}), the authors attribute low IQE values of 1-10% to low $\eta_{diss}\eta_{CC}$ of only 10.6 +/- 2.2 % (Figure 21e).

Kafle et al. further address delocalization by suggesting that charge separation at ZnPc/MoS_2 interfaces proceeds through delocalized hot charge transfer states (CT_h).[81] The authors use time-resolved two photon photoemission (TR-TPPE, Figure 21f-g) to track the processes that they attributed to ZnPc singlet exciton (S_1) quenching *via* charge transfer to MoS_2, followed by cooling within the charge-transfer state manifold.[81] They ascribed a time constant of 40 fs to PCT from ZnPc to MoS_2, after which CT_h at intermediate energy rose and decayed with a time constant of 120 fs. The authors suggested that this 120 fs decay of CT_h then gave rise to the relaxed, localized CT_0 state. This value is consistent with general charge-transfer time constants in organic/TMDC systems, which are reported in the range of sub-instrument-response to 10 ps. The value can be affected by factors such as the CT driving force, carrier delocalization, dielectric environment, and electronic coupling.[79, 232]

9.1.3 Effect of TMDC Thickness

TMDC thickness also plays an important role in the energy level alignment, charge transfer driving force, and prominence of energy transfer at TMDC/organic interfaces. For example, Figure 22a-b demonstrates the thickness dependence in WS_2/tetracene heterojunctions, where going from 1-layer to 2-layer WS_2 increases the valance band minimum and blocks hole transfer to the tetracene layer.[79] For the 1L-WS_2/tetracene Type-II junction, charge transfer occurs with a time constant of ~2.2 ps and out-competes energy transfer. As the WS_2 layer number (i.e., nL) increases,

the interface transitions from Type-II to Type-I, and energy transfer occurs upon selective tetracene excitation. The authors observed slower energy transfer with increasing thickness, ranging from 44 +/- 5ps for 2L-WS_2/Tc to 84.8 +/- 4.4 ps for 7L-WS_2/Tc.

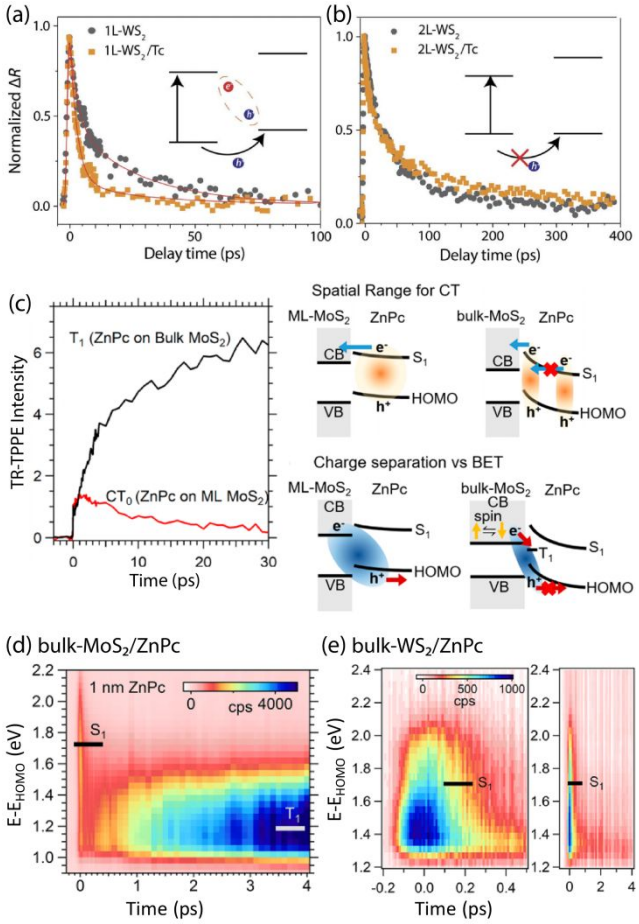

Figure 22. (a) Transient reflectance for neat 1L-WS_2 (grey circles) compared to 1L-WS_2/tetracene Type-II heterojunctions (yellow squares) where charge-transfer occurs versus (b) 2L-WS_2/tetracene Type-I heterojunctions where hole transfer is blocked and energy transfer occurs.[79] Panels (a) – (b) are from Ref. 79. © The Authors, some rights reserved; exclusive licensee American Association for the Advancement of Science. (c) TR-TPPE intensity for the ZnPc triplet (T_1, black) in ZnPc/bulk-MoS_2 heterojunctions compared to the relaxed charge-transfer state (CT_0, red) in ZnPc/monolayer-MoS_2 along with a schematic illustration of greater spatial range for the ZnPc singlet excitons near the interface in ZnPc/monolayer-MoS_2 compared to the bulk case, which results in charge separation in monolayer-MoS_2 heterojunctions versus back electron transfer (BET) that populates triplets in ZnPc for bulk-MoS_2 heterojunctions.[81] Reprinted with permission from ref. 81. Copyright 2019 American Chemical Society. (d) TR-TPPE shows triplet formation in ZnPc/bulk-MoS_2 heterojunctions.[80] (e) TR-TPPE shows singlet exciton decay and avoided ZnPc triplet formation in ZnPc/bulk-WSe_2 Type-I heterojunctions.[80] Panels (d) – (e) are reprinted with permission from ref. 80. Copyright 2017 American Chemical Society.

TMDC thickness variations can still affect heterojunction photophysics even when the energy level alignment remains favorable for charge transfer. For example, Kafle et al. addressed

thickness dependence of the TMDC layer using MoS_2/ZnPc interfaces (Figure 22c).[81] In this case, both 1L-MoS_2/ZnPc and nL-MoS_2/ZnPc interfaces have Type-II band alignment, despite the increase in MoS_2 valence band minimum with increasing thickness. The authors suggested that bulk-MoS_2/ZnPc heterojunctions are less efficient at free charge generation, which they attributed to strong band-bending in the ZnPc layer caused by HOMO energy pinning when ZnPc is deposited onto the bulk TMDC. The origin of this VB-HOMO pinning is still unclear, and further studies into such thickness-dependent interfacial interactions would be beneficial to the community. As depicted in Figure 22c, the authors suggest that this uneven energy landscape within the bulk TMDC causes (1) more localization of ZnPc excitons that suppresses singlet exciton dissociation, in addition to (2) more localization of interfacial charge-transfer states, where spin flipping on the TMDC side of the heterojunction results in triplet charge-transfer states that relax to low-energy ZnPc triplet excitons. Bulk-WSe_2/ZnPc heterojunctions were also investigated (Figure 22e) and found to form a Type-I junction, where singlet energy transfer from ZnPc to WSe_2 prevents low-energy ZnPc triplet formation by avoiding spin flipping within the charge-transfer mainfold.[80]

9.1.4 Triplet Excitons

Similar to the studies of recombination to triplets in ZnPc/TMDC heterojunctions by Kafel et al., the kinetic competition between charge separation/delocalization versus photocurrent loss to localized triplet excitons has been important for optimizing organic electronics.[262-264] However, TMDC-containing heterojunctions offer additional challenges for avoiding low-energy triplet excitons compared to organic-only systems. That is, the strong spin-orbit coupling associated with heavy metal atoms in TMDCs can expedite a spin flip to picosecond timescales in comparison to the nanosecond intersystem crossing times typical for neat organics. Indeed, the heavy-atom effect

in the TMDC layer likely contributes to the fast (<4 ps) conversion to triplets in TMDC/ZnPc heterojunctions, while intersystem crossing in neat ZnPc has been reported to proceed with >100 ps to nanosecond time constants.[80] In addition to exploring the effects of band bending as done by Kafle et al,[80] translating strategies from the OSC toolset to TMDC/organic heterojunctions may offer promise for future device optimization. For example, factors such as aggregation, functionalization, and molecular orientation have been found to alter the prevailing photophysical pathways in organic heterojunctions (i.e. charge separation versus loss to triplet states).[262-264]

We noted that, in some strategies envisioned for photovoltaics or solar fuels, triplet formation is desirable. In particular, singlet fission (SF) is a process by which one singlet exciton splits into two lower-energy triplet excitons, enabling greater than 100% photon-to-electron conversion.[265] High-efficiency SF has been demonstrated in a few molecular systems, most notably pentacene and tetracene.[266] Incorporating TMDCs as charge acceptors in SF devices requires proper energy level alignment to separate triplet excitons (produced by SF) into free carriers. While several studies have demonstrated photoactive pentacene/TMDC[232] or tetracene/TMDC[79] heterostructures, to our knowledge these heterojunctions generate carriers from TMDC singlet exciton dissociation and do not make use of SF or triplet dissociation. For example, Homan et al. showed that pentacene excitations in pentacene/MoS_2 systems do not contribute to photocurrent, which decreases the utility of this system as pentacene would be the primary light absorber in the active layer. Despite the Type-II energy alignment, dissociation of pentacene singlet excitons is out-competed by sub-picosecond SF, which rapidly produces two low-energy triplet excitons that are not extractable at the MoS_2 band energies.[232] Instead, the authors found that photocurrent generation is due to MoS_2 singlet exciton dissociation occurring on the time scale of 6.7 ps with 50% hole transfer yield to pentacene.[232] Computational studies provide further

insight, suggesting ultrafast hole transfer from MoS_2 to pentacene followed by carrier cooling and eventual slow interfacial charge recombination.[242] Further efforts to pair SF materials with different TMDCs may open new avenues for possible >100% charge generation yields if proper band alignment can be achieved to extract the SF-generated triplets that form on ultrafast timescales.

9.2 Photoinduced Charge Transfer at TMDC/Polymer Interfaces

Organic/TMDC heterojunctions that utilize semiconducting polymers rather than small molecules are promising due to the facile solution processing and scalability of polymer materials as well as benefits for exciton and charge transport offered by longer chain lengths. The organic photovoltaic community has explored charge generation in an extensive range of polymer structures, and Figure 23 demonstrates the transfer of this knowledge to organic/TMDC systems where heterojunctions were created using three common polymers from polymer:fullerene photovoltaics.[267] These polymers include P3HT (regioregular poly(3-hexylthiophene-2,5-diyl)), PCDTBT (poly[N-9′-heptadecanyl-2,7-carbazole-*alt*-5,5-(4′,7′-di-2-thienyl-2′,1′,3′-benzothiadiazole)]), and PTB7 (poly[4,8-bis[(2-ethylhexyl)oxy]benzo[1,2-b:4,5-b′] dithiophene-2,6-diyl][3-fluoro-2-[(2-ethylhexyl)-carbonyl]thieno [3,4-*b*]thiophenediyl])). All three polymers form Type-II heterojunctions with MoS_2 (Figure 23), suggesting that interfacial charge transfer is thermodynamically favorable. Using transient absorption spectroscopy, the authors suggested that charge transfer was faster from MoS_2 to PTB7 or PCDTBT (~120 fs) in comparison to P3HT (9 ps). Despite a slower charge-transfer time for P3HT/MoS_2 heterojunctions, the authors concluded that their MoS_2/P3HT samples were the most efficient due to increased carrier lifetime. Interestingly, the P3HT exciton luminescence increased three-fold in the heterojunction, which is not typically a sign of exciton dissociation to produce free carriers. Other studies have shown

quenched PL at MoS_2/P3HT interfaces, which has been attributed to charge transfer in these other samples.[268-270] The authors reported accelerated excited-state recombination in MoS_2/PTB7 and MoS_2/PCDTBT heterojunctions compared to the neat materials, suggesting the heterojunctions fabricated for this study require additional optimization to sustain free charge.

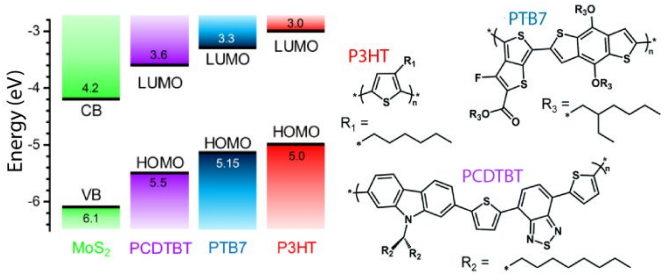

Figure 23. Energy levels for MoS_2 and polymers that were studied in heterojunctions with MoS_2 from Ref. [267]. Republished with permission of Royal Society of Chemistry, from ref. 267; permission conveyed through Copyright Clearance Center, Inc.

Studies by Zhong et al. provide further details on the photophysical mechanisms for ultrafast carrier generation and recombination at PTB7/MoS_2 heterojunctions, which are summarized in Figure 24a.[271] Similar to Petoukhoff et al,[267] the authors also observed charge transfer at timescales <250 fs, but Zhong et al. attributed the ultrafast process to a different origin, namely electron transfer from PTB7 to hot states in the MoS_2 conduction band (MoS_2^*) (Figure 24a).[271] Theoretical calculations support this assignment by showing ~10 fs electron transfer facilitated by delocalization across the PTB7 LUMO and MoS_2 conduction band (Figure 24b).[272] The different timescales between theory and experiment are likely due to the "perfect" nature of simulated interfaces that do not include disorder and defect sites. However, it is interesting to note that Garcia-Basabe et al. propose faster charge generation timescales in organic/TMDC systems than the timescales typically reported in studies using pump-probe spectroscopy.[268] They note that ultrafast processes may be masked by the instrument response function (IRF) in these laser-based characterization methods, and they use synchrotron-based spectroscopy (i.e. the core-hole clock

method) to measure charge transfer on femtosecond and sub-femtosecond timescales in P3HT/MoS_2 heterojunctions.[268]

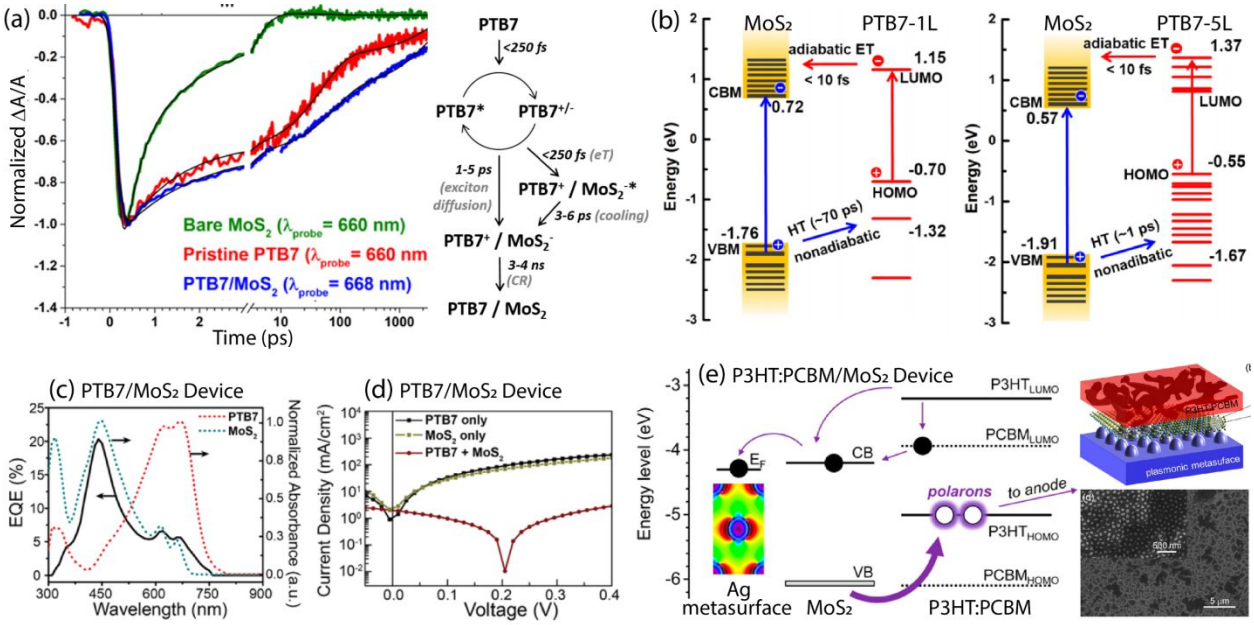

Figure 24. (a) Transient absorption showing longer-lived kinetics MoS_2/PTB7 heterojunctions compared to pristine MoS_2 or PTB7 along with the proposed photophysical pathways following excitation of PTB7 in the heterojunction.[271] Reprinted with permission from ref. 271. Copyright 2018 American Chemical Society. (b) Calculated energy alignment and photophysical processes in MoS_2/1L-PTB7 *versus* MoS_2/5L-PTB7.[272] MoS_2/PTB7 device data showing Reprinted with permission from ref. 272. Copyright 2019 American Chemical Society. (c) external quantum efficiency (EQE) and (d) current-voltage curves.[273] Panels (c) – (d) are reprinted with permission from ref. 273. Copyright 2016 American Chemical Society. (e) Photophysical pathways for charge generation in P3HT:PCBM/MoS_2 devices employing Ag metasurfaces, along with schematic illustration and scanning electron microscope image.[274] Reprinted with permission from ref. 274. Copyright 2016 American Chemical Society.

After the ultrafast, sub-IRF charge generation process, Zhong et al. further observe additional charge formation with a slower time constant (1-5 ps), which they attribute to both a exciton diffusion-limited electron transfer from PTB7 to MoS_2 as well as hole transfer from MoS_2 to PTB7.[271] Theoretical studies similarly suggest that the hole-transfer process proceeds on a slower timescale, ranging from 1 ps to 70 ps depending on the PTB7 thickness. As shown in Figure 24b, the calculations suggest accelerated hole transfer with increasing PTB7 thickness, which originates from a greater density of states in thicker PTB7 layers that can couple to the MoS_2 valence band.[271] This was suggested as a possible explanation for greater quenching of MoS_2 photoluminescence, which has been experimentally observed with increasing PTB7 thickness.[273]

In contrast to the studies of Petoukhoff et al.,[267] Zhong et al. did observe an increase in the excited-state lifetime in PTB7/MoS_2 heterojunctions compared to the neat materials (Figure 24a).[271] This contrast possibly stems from sample-to-sample variability and suggests room for better fundamental understanding of TMDC/organic interfaces. Zhong et al. attributed the longer lifetimes in the heterojunctions to free carrier formation at the interface and to a shift in the PTB7 equilibrium between excitons and polaron pairs. Shastry et al. similarly saw evidence for charge generation in PTB7/MoS_2 heterojunctions, including mutual PL quenching in the heterojunction and functional photovoltaic devices with 0.1% efficiency (Figure 24c-d). However, despite the charge generation observed in this system *via* spectroscopy, the PTB7/MoS_2 devices show minimal photocurrent originating from PTB7 light absorption (Figure 24c).[273] Zhong et al. suggest this may be caused by charge trapping at interfacial MoS_2 defects and recombination in PTB7 *via* polaron pair or triplet states.

Strategies to enhance light absorption in thin TMDC/organic device have been employed to increase charge photogeneration and power conversion efficiencies. For example, Petoukhoff et al. fabricated TMDC/polymer devices with plasmonic metasurfaces by patterning monolayer MoS_2 onto Ag nanoparticles and coating these surface with 1:1 P3HT:PCBM (Figure 24e).[274] The authors observed the greatest absorptance enhancement from the MoS_2 component, with 10-fold enhancement from 550-900 nm. MoS_2 to P3HT hole transfer was investigated with TR spectroscopy probing P3HT polaron and exciton states. The PCT processes are summarized in Figure 24e, where the enhanced MoS_2 absorptance led to greater PCT and higher P3HT polaron yields. Although the authors did not employ this structure in a device, other photovoltaic devices employing P3HT/PCBM/MoS_2 in various configurations show power conversion efficiencies (PCE) in the range of 1–4 %, slightly lower than PTB7/PCBM/MoS_2 devices with PCEs up to

~8%.[275] P3HT/PCBM/MoS_2 structures have also been employed in photocathodes for hydrogen evolution with photocurrent of 1.21 mA cm^{-2} at 0V vs. RHE under 1 Sun illumination.[276]

9.3 Photoinduced Charge Transfer at TMDC/SWCNT Interfaces

Beyond polymers and molecular semiconductors, semiconducting single-walled carbon nanotubes (s-SWCNTs) are another class of promising components for TMDC/organic heterojunctions. SWCNTs are intriguing for their very large aspect ratios with a rigid periodic lattice along the length of the tubes. These structures support features such as high carrier mobilities, low reorganization energies, sharp optical transitions, and diameter-dependent tunability of the energy landscape, while offering high photochemical stability.[277-278] Both photocurrent generation and hydrogen evolution have been demonstrated in TMDC/SWCNT heterojunctions.[279-282] For example, Figure 25a shows photocurrent generation in a heterojunction between monolayer MoS_2 and 1.4 nm diameter s-SWCNTs, where excitation of both MoS_2 (500-600 nm) and the SWCNT S_{22} (900-1100 nm) produce photocurrent.[279] However, it's important to note that there is still significant room for improvement through more systematic understanding of the charge generation, charge transfer, and recombination mechanisms.

Figure 25b-e shows recent investigations on the photophysics at interfaces between monolayer MoS_2 and highly-enriched 0.76 nm diameter (6,5) s-SWCNTs using transient absorption spectroscopy.[163] Sub-picosecond charge transfer at these Type-II interfaces was characterized by the SWCNT trion (X^+) induced-absorption signature shown in Figure 25b. Figure 25e shows exceptionally long carrier lifetimes in these heterojunctions, with an amplitude-averaged lifetime of 0.73 μs from components of 17.5 ns (43%), 233 ns (43%), and 4.4 μs (14%). These carrier lifetimes significantly exceed those observed for the TMDC/TMDC, TMDC/molecule, and TMDC/polymer heterojunctions discussed above. The high carrier

mobilities in SWCNT networks are suggested to facilitate charge motion away from SWCNT/TMDC interfaces and support these exceptionally long carrier lifetimes.[163] Despite the long carrier lifetimes, these heterojunctions could be further optimized by improving the charge-transfer yields, which were estimated as ~23% for electron transfer from the SWCNTs to MoS_2 and ~39% for hole transfer from MoS_2 to the SWCNTs.

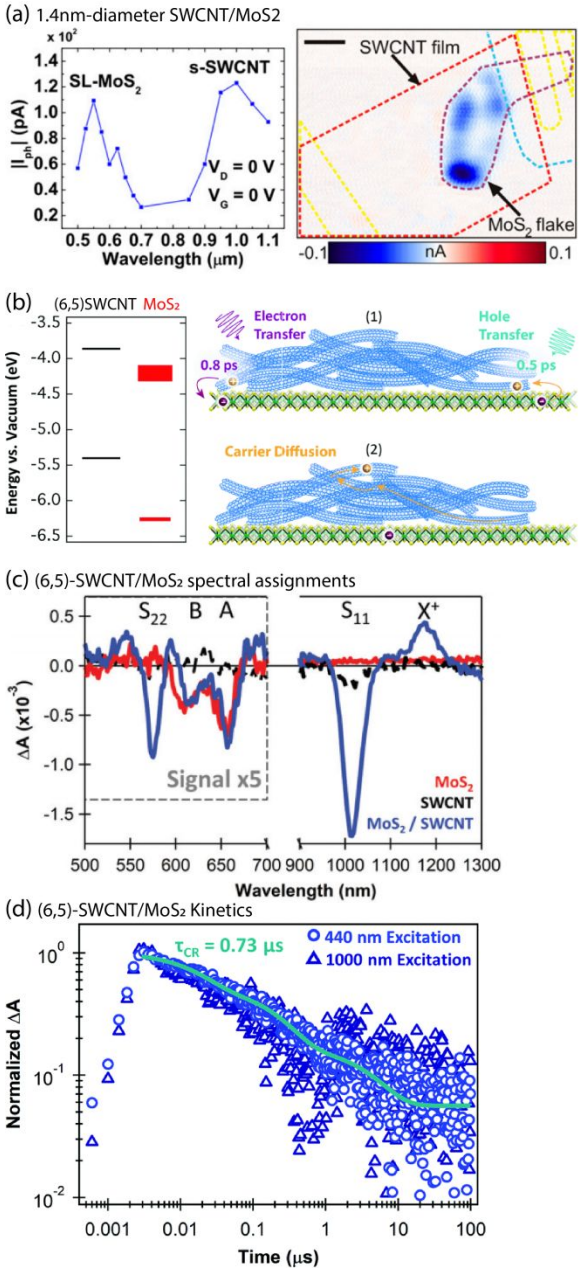

Figure 25. (a) Wavelength-dependent photocurrent (I_{ph}) and photocurrent map for 1.4 nm-diameter SWCNT/MoS_2 devices.[279] Republished with permission of Royal Society of Chemistry, from ref. 279; permission conveyed through Copyright Clearance Center, Inc. (b) Type II energy-level offsets and schematic illustration of charge transfer in

(6,5)SWCNT/MoS_2 heterojunctions along with (c) assignment of spectral features in TA spectra and (d) demonstration of exceptionally long-lived charge carriers with charge recombination time constant (τ_{CR}) of 0.73 μs.[163] Panels (b) – (d) are republished with permission of Royal Society of Chemistry, from ref. 163; permission conveyed through Copyright Clearance Center, Inc.

With a goal of achieving controlled, clean interfaces and strong electronic coupling in TMDC/SWCNT hybrid systems, recent studies have begun to explore CVD-based methods for conformal TMDC growth.[283-284] Figure 26a–c shows a study by Xiang et al.[283] where low-pressure CVD or metal-organic CVD was used to conformally grow MoS_2 single-walled nanotubes around SWCNTs within a free-standing network. MoS_2 only grew on SWCNTs with diameters >3 nm, and the MoS_2 nanotube yield was very low (<1%) in this procedure due to the strain associated with MoS_2 nanotubes <4 nm. A CVD-grown BN coating around the initial SWCNT enabled higher yield of MoS_2 nanotube growth due to a reduction in the strain. Liu et al. recently demonstrated the CVD growth of MoS_2 single crystals on SWCNTs that were grown prior on a quartz substrate.[284] The authors found that MoS_2 flakes grew over top of the SWCNTs instead of underneath the SWCNTs (Figure 26d). Identical polarized second harmonic generation (SHG) patterns were observed in multiple spots of the interfaced MoS_2 flakes (Figure 26f), indicating that the whole MoS_2 domains were single crystal. While both of these studies demonstrated PL quenching of the CVD-grown MoS_2 by proximal SWCNTs, there is a large degree of polydispersity in interface energetics due to the uncontrolled electronic structure of these SWCNTs (i.e. metallic and semiconducting SWCNTs both present). The quenching likely originated from energy transfer in both studies due to the large SWCNT diameters. Looking forward, such growth techniques may be useful for creating Type-II TMDC/SWCNT heterojunctions if the starting SWCNTs are small-diameter highly enriched s-SWCNTs.

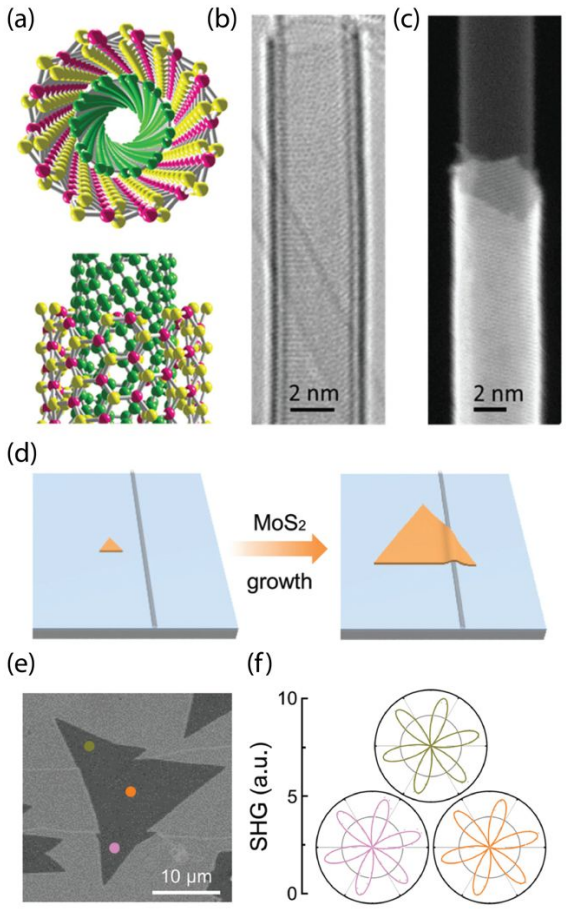

Figure 26. CVD-grown MoS_2/SWCNT Heterojunctions. (a) Atomic model, (b) high-resolution TEM image, and (c) high-angle annular dark field STEM image of single-walled MoS_2 nanotube grown on a SWCNT.[283] Panels (a) – (c) are Ref. 283. © The Authors, some rights reserved; exclusive licensee American Association for the Advancement of Science. (d) Schematic of MoS_2 growing over top of SWCNT where the CVD MoS_2 growth occurs on pre-grown SWCNTs on a quartz substrate.[284] (e) SEM image MoS_2 monolayer grown across SWCNTs where discontinuous edges are formed at two sides of the nanotubes. (f) Polarized SHG patterns taken at positions labeled in panel (e) indicate the MoS_2 domain is a single crystal. Panels (d) – (f) are republished with permission of Royal Society of Chemistry, from ref. 284; permission conveyed through Copyright Clearance Center, Inc.

10. TMDC/Quantum Dot Interfaces

Semiconductor nanocrystals (quantum dots, QDs) are an interesting class of 0D excitonic nanomaterials, where the optical band gap can be synthetically tuned across a wide spectral range (e.g. UV to IR) through appropriate material selection and QD size. The size-tunable bandgap has made QDs versatile components in commercialized light-emitting diode (QLED) displays, a wide spectral range of photodetectors, PV applications, and photocatalysis.[36, 285-289] Here, we discuss the unique photophysics that occur in 0D/2D QD/TMDC structures.

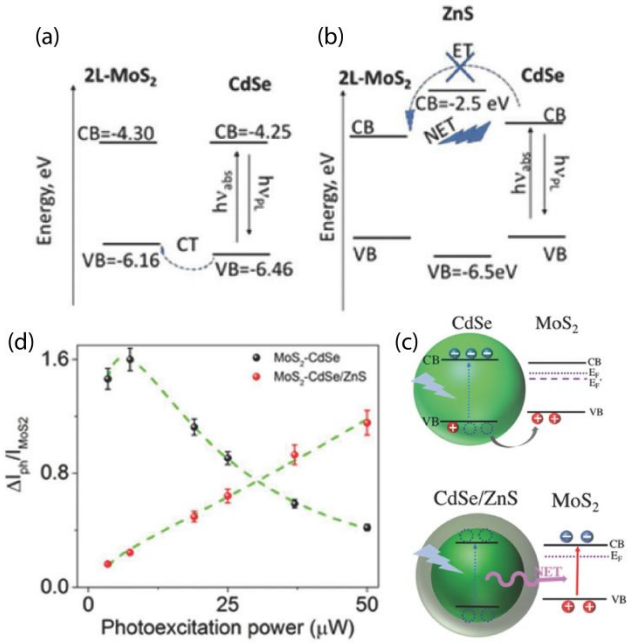

Figure 27. Interfacial transfer of bilayer MoS_2 with CdSe (core only) or CdSe/ZnS (core/shell) QDs. (a) Energy level diagram for MoS_2/CdSe where photoexcited CdSe transfer holes to MoS_2 and can have excess negative charge accumulate on CdSe at higher photoexcitation powers (photogating). (b) Energy level diagram of MoS_2/CdSe/ZnS systems where nonradiative energy transfer (NET) occurs. (c) Illustration of the charge transfer and NET processes. (d) Photocurrent as a function of laser power, where the positive slope versus photoexcitation power in MoS_2-$CdSe_2$/ZnS is better for photovoltaics and the negative slope due to photogating from electron accumulation in MoS_2/$CdSe_2$ system is better for photodetectors at low light exposure.[290] All panels reprinted with permission from ref. 290. Copyright 2018 Wiley.

Because the photophysical processes at semiconductor interfaces determine their best-suited device applications, it is important to differentiate between various interfacial charge-transfer and energy-transfer pathways that may take place. Li et al. addressed this in 2L-MoS_2/QD devices, where charge transfer dominated in heterojunctions with core-only CdSe QDs, and nonradiative energy transfer (FRET) dominated when using core/shell CdSe/ZnS QDs (Figure 27a-c).[290] In both cases, the authors observed significant interfacial interactions resulting in >95% quenching of the QD PL lifetimes when used in heterojunctions (from 15 ns to 430 ps in core-only and from 19 ns to 320 ps in core/shell). While a driving force for PCT would exist between 2L-MoS_2 and CdSe in both cases, the ZnS shell blocks charge transfer in the heterojunction with core-shell QDs, which

enables the competitive FRET process to dominate. Interestingly, the authors observed different trends in photocurrent response with increasing photoexcitation power between the two heterojunctions (Figure 27d). In the case of PCT (MoS_2/CdSe heterojunction), the authors attributed decreasing photocurrent with fluence to a photogating effect where accumulation of negative charge on the QD decreases MoS_2 band bending to inhibit hole collection. Such charge accumulation and resulting photogating does not occur in the 2L-MoS_2/CdSe/ZnS system where energy transfer dominates. Based on the differences in fluence dependence, the authors suggest that the 2L-MoS_2/CdSe/ZnS system would be useful for photovoltaic applications, which operate under higher fluences, and MoS_2/CdSe heterojunctions can be used for photodetectors under lower light intensities.

Boulesbaa et al. studied interfacial charge transfer between monolayer WS_2 and CdSe/ZnS (core/shell) QDs (Figure 28).[291] The authors demonstrated mutual PL quenching in this system, suggesting that charge transfer (rather than energy transfer) takes place. To highlight the effect of driving force for electron transfer from photoexcited WS_2 to the QD, the authors increased the QD core diameter, which lowers the *EA* while keeping the *IP* constant (Figure 28a). The higher driving force for electron transfer resulted in a greater quenching of the PL lifetime (Figure 28b), consistent with Equation 6 (Marcus Theory). Using TA spectroscopy, the authors showed WS_2 to QD electron transfer in <45 fs to yield an interfacial exciton (HX) with ~140 meV binding energy that decays on picosecond time scales. Interestingly, based on the change in ground-state absorption spectrum (Figure 28c-d), the authors postulate the formation of two HXs, where the lower-energy HX1 involves a hole in WS_2 band that gives rise to B excitons, and the higher-energy HX2 involves a hole in WS_2 band that gives rise to C excitons (Figure 28e).

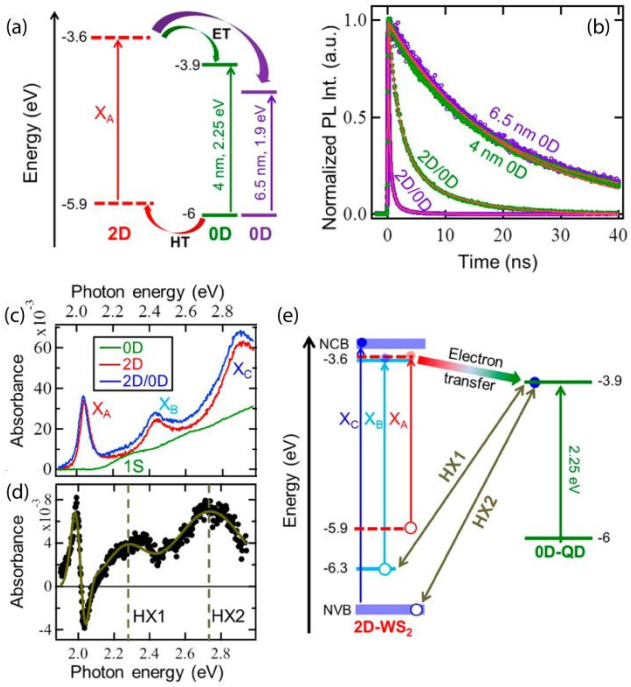

Figure 28. Monolayer WS_2 and CdSe/ZnS (core/shell) QDs dynamics. (a) Energy schematic showing increased driving force for electron transfer (ET) from WS_2 (labeled as 2D) to 0D QDs with larger core diameter while hole transfer (HT) is unaffected. (b) The heterojunction with larger driving force shows faster PL decay compared to neat QDs. (c) Comparison of steady-state absorption spectra of the heterojunction with the separate WS_2 and QD layers where (d) the difference shows new absorption features labeled as hybrid excitons HX1 and HX2. (e) Illustration of the HX states in the 2D/0D hybrid system, showing the single-particle states making up the A (red), B (cyan), and C (purple) excitons (X_i) of WS_2. QD states are shown in green.[291] All panels reprinted with permission from ref. 291. Copyright 2016 American Chemical Society.

Similar to the studies of PCT driving force by varying QD diameter in Figure 28a-b, Chen et al. [44]varied the PCT driving force in two ways – (1) by pairing a single size of PbS/CdS QDs with MoS_2 having variable numbers of layers (Figure 29a), where the driving force increases with increasing layer number, and (2) by pairing MoS_2 bilayers with PbS/CdS QDs having variable diameters (Figure 29b), where the driving force increases with decreasing QD diameter. In both cases, the authors used TRPL to demonstrate that the PCT rate (k_{ET}) increased with increasing thermodynamic driving force (Figure 29c – d). These results can be understood within the Marcus formulation of charge transfer, as discussed in Section 1 (Equation 6).

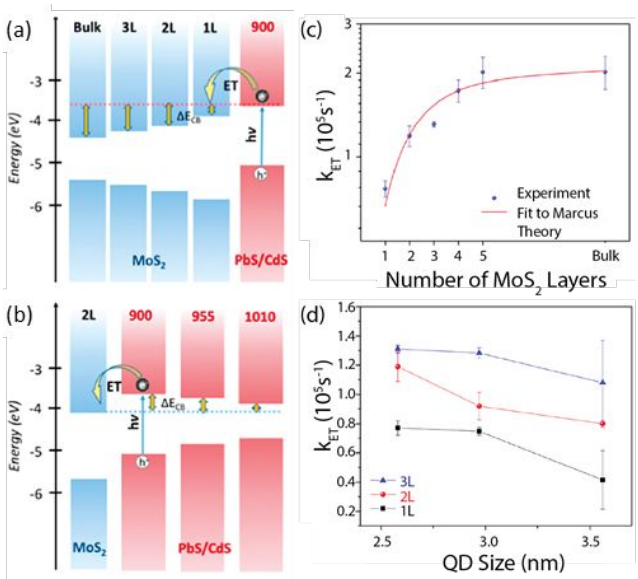

Figure 29. (a) Interfacial charge transfer kinetics are tied to the thermodynamic driving force for photoexcited electron transfer from PbS/CdS QD to MoS_2.[44] The energetics of (a) MoS_2 with variable numbers of layers interfaced with PbS/CdS QDs at a single diameter or (b) bilayer MoS_2 interfaced with variable diameters of PbS/CdS QDs. (c) The photoinduced electron transfer rate increases with the number of MoS_2 layers due to an increase in the driving force. (d) The photoinduced electron transfer rate decreases with QD size due to a decrease in the driving force. Reprinted with permission from ref. 44. Copyright 2019 American Chemical Society.

Monolayer WS_2 interfaced with InGaN QDs (Figure 30a) has unique emission properties that are attributed to an interfacially-bound negative trion, where Coulombically-bound WS_2 excitons couple to electrons accumulated at the QD surface (Figure 30b).[285] This interfacial state (X, Figure 30) is lower in energy than the WS_2 exciton (A) and higher in energy than the WS_2 trion (T). Interestingly, the WS_2 spin-valley physics are transferred to the electrons of the QD. Specifically, the emission from both the WS_2 exciton (A) and interfacial trion (X) are influenced by circularly polarized light (Figure 30c). That is, the emission intensity depends on the detection polarization (i.e., left-left: LL or left-right: LR) with circularly polarized emission intensity ratios $((I_{LL} - I_{LR})/(I_{LL} + I_{LR}))$ of 16% for both X and A.

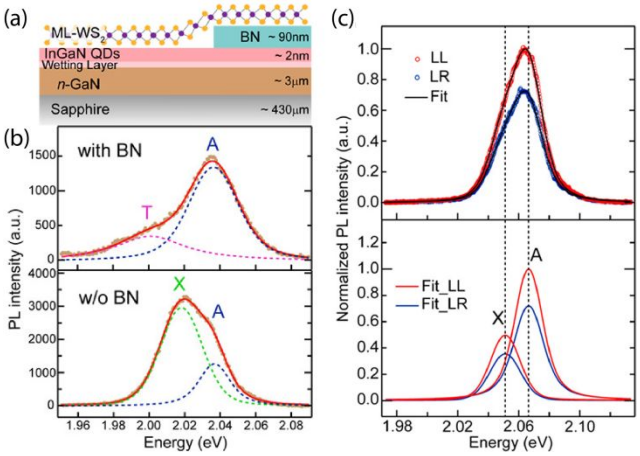

Figure 30. Interfacially-bound negative trion between monolayer WS_2 and InGaN QDs. (a) Schematic of the WS_2/InGaN device design where BN is boron nitride. (b) PL from the WS_2/BN/InGaN QD region showing WS_2 exciton (A) and trion (T) emission. PL in the WS_2/InGaN QD region without BN shows quenched WS_2 T emission with additional interfacial negative trion (X) emission. (c) Left circularly polarized excitation with left/right circularly polarized emission detection (LL or LR, respectively) for WS_2/InGaN interfaces. The circular polarization is 16% for both X and A.[285] Reprinted with permission from ref. 285. Copyright 2018 American Chemical Society.

TMDC/QD interfaces have recently been commissioned for infrared (IR) photodetectors. These have benefits over graphene/QD systems because the dark current is reduced by the TMDC band gap and devices can be switched on/off with gating.[292] In 2015, Kufer et al. reported on a few-layer MoS_2/p-type PbS QD phototransistor, that exhibited photoexcited electron transfer from the PbS QDs to TMDC with a photoresponse up to ~1.2 μm (Figure 31a and 31b).[292] The responsivity of the phototransistor was greatly improved by interfacing PbS QDs with MoS_2 compared to PbS QDs only, where the responsivity improved to 6 x 10^5 A/W from 4.3 x 10^2 A/W. Moreover, the spectral range extended much further into the IR compared to the MoS_2 only (Figure 31b), and the hybrid system had a typical decay time of 350 ms and a detectivity of 5 x 10^{11} Jones (detectivity figure of merit). Similarly, PbS QDs have also been coupled with 2D WSe_2 to be a broadband transistor with high performance. Hu et al. demonstrated this 2D TMDC/PbS QD interface also gives good responsivity (Figure 31c, 2 x 10^5 A/W) and can be used in the IR with a respectable decay time of 480 ms and detectivity of 10^{13} Jones.[293]

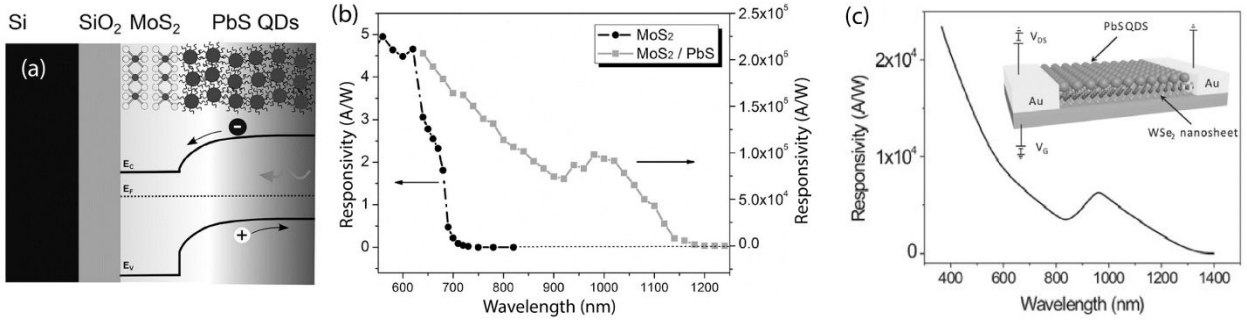

Figure 31. Photodetectors using few-layered MoS_2 with n-type PbS quantum dots (QDs). (a) Energetic depiction of the MoS_2/PbS interface.[292] (b) Responsivity of the MoS_2-only or MoS_2/PbS QDs.[292] Panels (a) – (b) are reprinted with permission from ref. 292. Copyright 2015 Wiley. (c) Responsivity of WSe_2/PbSQD.[293] Reprinted with permission from ref. 293. Copyright 2017 Wiley.

In 2019, Özdemir et al. demonstrated TMDC/QD interfaces with photodetection up to 2 μm. The authors found that few-layered WS_2/PbS QD detectors outperformed few-layered MoS_2/PbS QD detectors due to a greater driving force for electron transfer from PbS to WS_2.[294] The WS_2/QD system showed responsivity of 1400 A/W at 1.8 μm and 1 V bias with 10^{12} Jones at room temperature. Moreover, the WS_2/PbS QD device decay time was improved by an order of magnitude compared to the MoS_2-based device (Figure 32a). The authors suggested that band bending at the MoS_2/QD interface results in a barrier for electron transfer, enhancing interfacial recombination for this system and a poorer photoresponse. (Figure 32b)

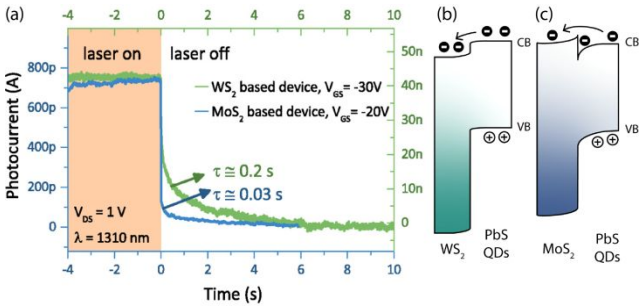

Figure 32. TMDC/QD infrared detectors. (a) Few-layered WS_2/PbS QD system has longer photocurrent lifetimes than few-layered MoS_2/PbS QD systems. (b) and (c) band energetics and charge transfer in WS_2 and MoS_2-based hybrid devices, respectively.[294] All panels are reprinted with permission from ref. 294. Copyright 2019 American Chemical Society.

MoS_2 has also been explored for photodetector applications in heterojunctions with ZnCdSe/ZnS core/shell QDs.[287] These photodetectors showed improved response over MoS_2 by 3

orders of magnitude, with 10^4 A/W and detectivity of 10^{12} Jones at wavelengths >700 nm. Interestingly, the inner ZnCdSe core of the QD would form a Type-II band offset with MoS_2, but the wide-gap ZnS shell forms a Type-I junction with both ZnCdSe and MoS_2 components. For this reason, electron transfer from photoexcited QDs to MoS_2 occurs via tunneling, and simultaneous exciton energy transfer from the ZnCdSe core to MoS_2 is also proposed. The authors find that photocurrent improves when going from few-layer to monolayer MoS_2, consistent with a report by Prins et al. showing greater nonradiative energy transfer from photoexcited CdSe QDs to monolayer versus few layer MoS_2.[295] They attribute higher energy transfer efficiency to lower dielectric screening as the MoS_2 layer thickness decreases. Another example of MoS_2/QD hybrids is dodecanethiol-functionalized MoS_2 nanosheets coupled to dodecanethiol-functionalized $CuInS_2$ QDs. Ahmad et al. showed improved photocurrent response of MoS_2/$CuInS_2$ QD hybrids compared to the QD or nanosheet only, which they attribute to charge transfer at the Type-II heterojunction.[296]

A recent study by Wang et al. suggests that heterostructures between exfoliated few-layer MoS_2 and PbS nanoplatelets can enable long-lived infrared-responsive photoconductivity.[297] In this case, phototransistors made from the heterostructures generated photocurrent upon NIR excitation of the PbS nanosheets, driven by photoinduced electron transfer from PbS to MoS_2. Band bending at the interface produced a small recombination barrier, so that cooling the system to 180 K or lower led to a persistent photoconductivity that showed little decay over the ~10^4 second experimental time frame. Such results demonstrate the potential applicability of TMDC-based heterostructures to optical information processing applications such as nonvolatile memory or neuromorphic computing.

11. TMDC/Perovskite Heterojunctions

Metal-halide based perovskites are a fascinating class of solution-processable semiconductors that are being explored for a variety of optoelectronic and energy applications. Perovskite is a general crystal structure with ABX_3 stoichiometry. In metal-halide perovskites, A is an organic (e.g. methyl ammonium, MA) or inorganic (e.g. cesium) cation, B is a transition metal (most typically lead), and X is a halide anion. Based in part on exceptionally high free carrier yields and diffusion lengths, solar cells based on these materials have rapidly increased in efficiency over the past decade, with certified power conversion efficiencies now surpassing 25%.[298-299] High PL quantum yields enable efficient light-emitting diodes (LEDs) across widely tunable ranges of emission energy.[300-301] In addition to these more traditional optoelectronic applications, the existence of strong spin-orbit coupling, long spin coherence lifetimes,[302] and Rashba spin-splitting[303] has spurred interest in perovskites for spintronic applications.[304]

Thus far, TMDC/perovskite interfaces have been studied primarily in the context of photovoltaics[305-308] and photodetectors,[309-312] with $MoS_2/MAPbI_3$ interfaces receiving the most attention (Figure 33a). Perovskite solar cells use an electron transport layer (ETL) and hole transport layer (HTL) to extract electrons and holes, respectively.[313-316] Interestingly, despite MoS_2 typically serving as an n-type material and electron acceptor,[310] these perovskite PV studies have primarily (but not exclusively)[306] utilized MoS_2 as an HTL.[305, 307-308] This brings up important questions about the energetics of this interface, since the typically reported range for the VBM of MoS_2 (-6.2 to -6.3 eV vs. vacuum) would not appear to favor hole transfer from the valence band of $MAPbI_3$, which is typically reported in the range of -5.4 to -5.8 eV vs. vacuum.[314] Indeed, using ultraviolet photoelectron spectroscopy, Peng et al. concluded that a pristine MoS_2 monolayer forms a Type-I band alignment with $MAPbI_3$ (Figure 33b), consistent with transient absorption results that suggest negligible hole transfer from the perovskite to the TMDC.[317]

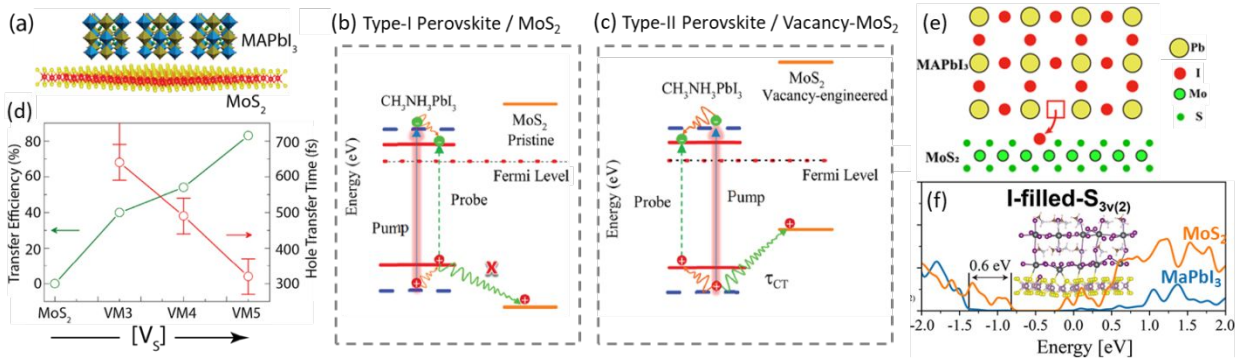

Figure 33. (a) Schematic of MoS_2/$MAPbI_3$ heterjunction.[317] (b) Schematic of MoS_2/$MAPbI_3$ interfacial energetics that result in Type-I offset in comparison to (c) Type-II offset when MoS_2 is treated by O_2 plasma to create sulfur vacancies. (d) Hole transfer efficiency (left axis) and hole transfer time (right axis) from $MAPbI_3$ to MoS_2, measured by transient absorbance spectroscopy, for MoS_2 with varying sulfur vacancy density [V_S].[317] Panels (a) – (d) are reprinted with permission from ref. 317. Copyright 2016 American Chemical Society. (e) Schematic of MoS_2/$MAPbI_3$ interfaces where MoS_2 sulfur vacancies induce $MAPbI_3$ iodine vacancies at the interface, leading to (f) calculated band offsets with Type-II energy alignment.[32] Panels (e) – (f) are reprinted with permission from ref. 32. Copyright 2020 American Chemical Society.

To determine the degree to which interfacial atomic structure may impact the thermodynamics and kinetics, the same authors used a mild O_2 plasma treatment to create sulfur vacancies in MoS_2.[317] First-principles calculations indicated that S vacancies produce mid-gap states, making the "vacancy-engineered" MoS_2 monolayer p-type, consistent with the experimental observation of a large (~1.1 eV) increase in the MoS_2 work function (Figure 33c). This significantly larger work function changed the interfacial band alignment at the vacancy-engineered MoS_2/$MAPbI_3$ to Type-II. TA measurements showed a delayed rise time of the perovskite bleach that was interpreted as arising from ~490 fs hole transfer from the photoexcited $MAPbI_3$ to the vacancy-engineered MoS_2. The extracted hole transfer time decreased and the hole transfer efficiency increased with increasing MoS_2 S vacancy density (Figure 33d),[317] providing a potential means for improving the efficacy of MoS_2 hole transport layers in perovskite solar cells.[307]

Shi et al. followed up on the impact of vacancies for interfacial alignment with a detailed molecular dynamics study of the monolayer MoS_2/$MAPbI_3$ interface (Figure 33e-f).[32] Their simulations suggested that sulfur vacancies alone are not sufficient to reverse the VBM offset to favor hole transfer from perovskite to TMDC. Instead, they find that sulfur vacancies attract iodide

anions from the $MAPbI_3$, which in turn creates adjacent iodine vacancies at the interface. The resulting interface dipole moment lifts the VBM of MoS_2 above $MAPbI_3$ by 0.2 – 0.6 eV, creating a thermodynamic driving force for hole extraction by MoS_2 and a Type-II interface (Figure 33f). Hole transfer was found to proceed in a biphasic manner, with an adiabatic component (20 fs) and a non-adiabatic component (200 – 800 fs). These studies suggest that MoS_2 effectiveness as a HTL in perovskite solar cells may depend on the exact atomic structure of each component and the resulting reconstruction upon interface formation.

Recent studies have expanded the initial work on the prototypical $MoS_2/MAPbI_3$ interface to a variety of different TMDC/perovskite interfaces. Bauer et al. used transient reflectivity to study the interface between CVD-grown monolayer WS_2 and a thin film of bulk $MAPbI_3$ perovskite.[318] When exciting this heterojunction at 3.1 eV, higher in energy than the optical gap of both the perovskite (1.6 eV) and the WS_2 (2.0 eV), the perovskite PL was quenched by ~85% and the WS_2 PL was entirely quenched. Since energy transfer is not possible from $MAPbI_3$ to WS_2 *and* the $MAPbI_3$ is quenched instead of enhanced, the authors concluding that quenching occurred primarily *via* charge transfer and not energy transfer. The band alignment suggests electron transfer from WS_2 to $MAPbI_3$, with a time constant shorter than the instrument response (< 45 fs). Charge separation inhibited recombination, with the slowest recombination time around 2.2 ns.

As with the $MoS_2/MAPbI_3$ interfaces discussed above, theoretical studies of TMDC/perovskite nanocrystal interfaces similarly suggest interfacial atomic structure plays an important role in the heterojunction photophysics. Several *experimental* studies indicate that relatively high bandgap perovskites such as $CsPbBr_3$ nanocrystals undergo efficient energy transfer to TMDCs like WS_2, significantly enhancing the TMDC PL quantum yield.[36, 319] Theoretical calculations, however, suggest that the dynamics at this interface depend on the $CsPbBr_3$ surface termination.[320] In

particular, $PbBr_2$ termination led to a Type-I interface, consistent with the energy transfer observed in experimental studies, while Cs/Br^- terminated surfaces generated Type-II interfaces. Nonadiabatic molecular dynamics simulations of the Type-II heterojunction suggested sub-picosecond PCT, after which the separated charges live for ~2 ns.

Fang et al. studied the dynamics of charge separation and recombination in heterojunctions between $CsPbBr_3$ perovskite nanowires (PNWs) and either monolayer MoS_2 or monolayer WSe_2 (Figure 34a).[321] X-ray photoelectron spectroscopy suggested Type-I band alignment for $CsPbBr_3/MoS_2$ and Type-II alignment for $CsPbBr_3/WSe_2$ (Figure 34b). As such, selective photoexcitation of the $CsPbBr_3$ NWs initiated energy transfer to MoS_2 with an estimated efficiency of 71% and rate of 1 x 10^9 s^{-1}. Selective excitation of WSe_2 in $CsPbBr_3/WSe_2$ resulted in electron transfer from WSe_2 to $CsPbBr_3$ at an estimated 70% efficiency. The authors characterized electron transfer via the rise in PNW TA signal with a time constant of ~7 ps, followed by decay over ~59 ps representing the recombination of carriers across the interface (Figure 34c).

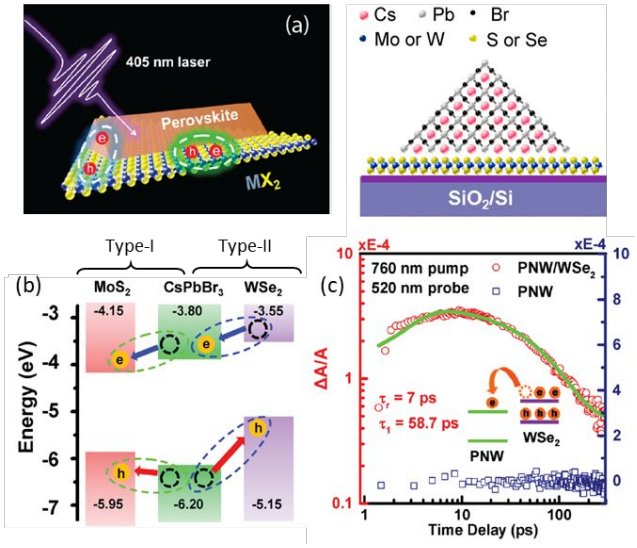

Figure 34. (a) Schematic of heterojunction between $CsPbBr_3$ perovskite nanowire (PNW) and MX_2 monolayer. (b) Photoelectron spectroscopy suggests Type-I band alignment for interface with MoS_2 and Type-II alignment for WSe_2. (c) Transient absorbance dynamics showing 7 ps rise time for photoinduced electron transfer from WSe_2 to $CsPbBr_3$ NW, followed by 59 ps recombination of separated charges. All panels are reprinted with permission from ref. 321. Copyright 2018 American Chemical Society.

12. 2D TMDC Hybrid Redox Systems for Water Splitting

2D TMDCs have several advantages for use in photoredox systems. In particular, the large surface area and ultrathin nature minimize the distance that an excited carrier must travel to reach the surface, where electrolyte and reactants can be readily available to interact. Interaction between TMDCs with adsorbates and electrolytes is critical for many chemical processes, such as photoactivated H_2 and O_2 generation from water,[13-14, 322-324] CO_2 photoreduction,[325-328] and N_2 photofixation.[151, 329] To optimize these reactions, it is important to control the catalytic TMDC interface and to generate long-lived charge carriers to drive the desired photochemical reactions. Some strategies for optimizing and extending carrier lifetimes in TMDC-based photoredox systems, which we discuss in this section, include (i) making hybrid interfaces that separate photoexcited charge carriers through Type-II heterojunctions and Z-schemes, (ii) modifying the TMDC through surface functionalization or internal strain, (iii) employing both semiconducting 2H and metallic 1T TMDCs phases to optimize both light absorption and conductivity, and (iv) utilizing plasmon interactions for band-bending, energy level alignment, or enhancing light absorption. Here, we discuss PCT in several hybrid TMDC-based photoredox systems for water splitting.

In water splitting, the two half reactions of interest are the hydrogen evolution reaction (HER) and oxygen evolution reaction (OER), which are given by Equations 7 and 8, respectively, in Section 3. For HER to occur, the semiconductor's CBM must be at a more reducing potential (closer to vacuum) than the reduction potential of HER (Equation 7). For OER to occur, the VBM must be at a more oxidizing potential (further away from vacuum) than the oxidation potential of OER (Equation 8). For overall water splitting, the semiconductor's CBM and VBM straddle the HER and OER potentials with a bandgap that exceeds 1.23 eV.[330] The relationship between the

band energetics of a semiconductor in vacuum and HER/OER stem from a 1986 report by Trasatti.[331] Based on this report, 0 V vs NHE (HER) corresponds to -4.44 eV with respect to vacuum, and therefore, 1.23 V vs NHE (OER) correlates to -5.67 eV with respect to vacuum.

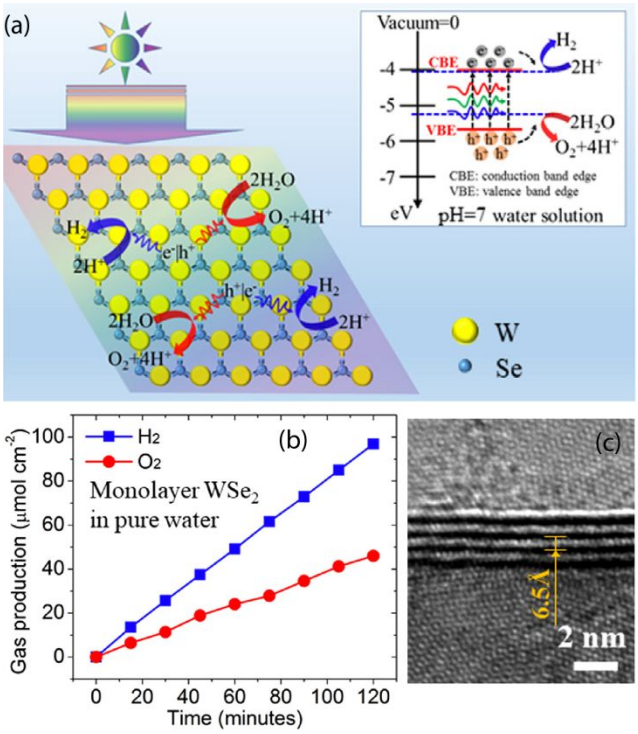

Figure 35. (a) Schematic representation of monolayer WSe_2 being photoactive for overall water splitting, where the CBM (or conduction band edge -CBE) and VBM (or valance band edge-VBE) are properly aligned. (b) Measured H_2 and O_2 gas production from water splitting by monolayer WSe_2. (c) lateral view of layer stacking of photoactive WSe_2 samples.[322] Reprinted with permission from ref. 322. Copyright 2018 Elsevier.

Experimental and theoretical reports suggest several TMDCs to be good HER and/or OER materials.[13-14, 118, 323-324, 332-333] For example, one candidate for carrying out overall photoinduced water splitting is monolayer WSe_2. Figure 35 shows an example in which Wang et al. grew wafer-scale WSe_2 monolayers via molecular beam epitaxy on SiO_2 substrates.[322] The authors found that at pH 7 the WSe_2 monolayers could be photocatalytic for both HER and OER, which experimentally demonstrated that the VBM and CBM are properly aligned for water splitting. The 1.65 eV band gap of monolayer WSe_2, results in a ~0.1 eV and ~0.3 eV driving force for proton

reduction and water oxidation, respectively. The fact that monolayer WSe_2 photocatalytically splits water contradicts some theoretical reports (e.g. Figure 7a). This highlights the need to execute experiments while using the theoretical TMDC band energetics primarily as a rough guide. Indeed, the band energetics are highly influenced by many factors including experimental conditions, doping, ambient environment, substrate, and strain.

12.1

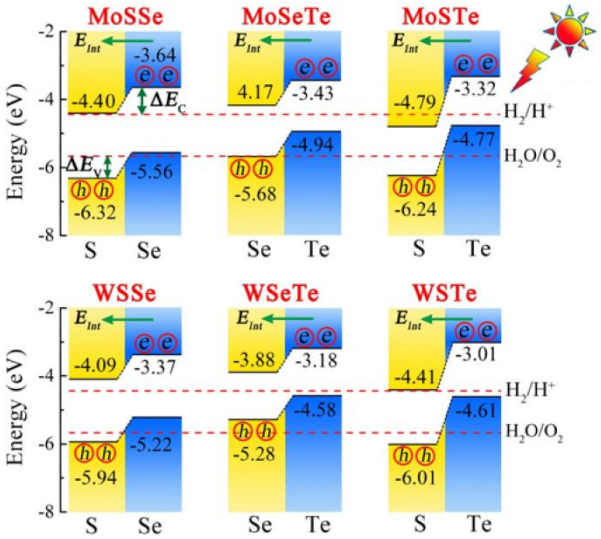

Figure 36. Calculated band energies for Janus TMDCs with comparison to the HER and OER half reaction energies.[334] Reprinted with permission from ref. 334. Copyright 2018 by the American Physical Society.

One possible disadvantage for HER and OER reactions both occurring on the same 2D semiconductor is that recombination of opposite charge carriers in close proximity could kinetically out-compete the water-splitting half reactions Engineering internal electric fields can help separate charges and extend carrier lifetimes. An interesting way to tune the band energetics and achieve some separation of opposite carriers even within a monolayer is to create Janus TMDC monolayers, where the chalcogenides on each side of the transition metal are different. Xia et al. calculated the band structure and energetics for such systems.[334] The authors predicted that Janus monolayers would have an inherent electric field produced by the asymmetric surfaces, which keeps holes and electrons spatially separated (Figure 36). They proposed MSTe (M=Mo, W) to be

the best photocatalyst for water splitting due to the large driving force for HER and OER along with the large dipole moment caused by the difference in electronegativity between S and Te atoms. The Janus monolayer MoSSe has been experimentally synthesized and found to be good for dark H_2 evolution on the basal sites due to the inherent defects and strain induced by the asymmetry.[335] The MoSSe outperforms MoS_2 or $MoSe_2$ when using dark electrochemistry. To the best of our knowledge, Janus particles have not been tested for photocatalytic activity.

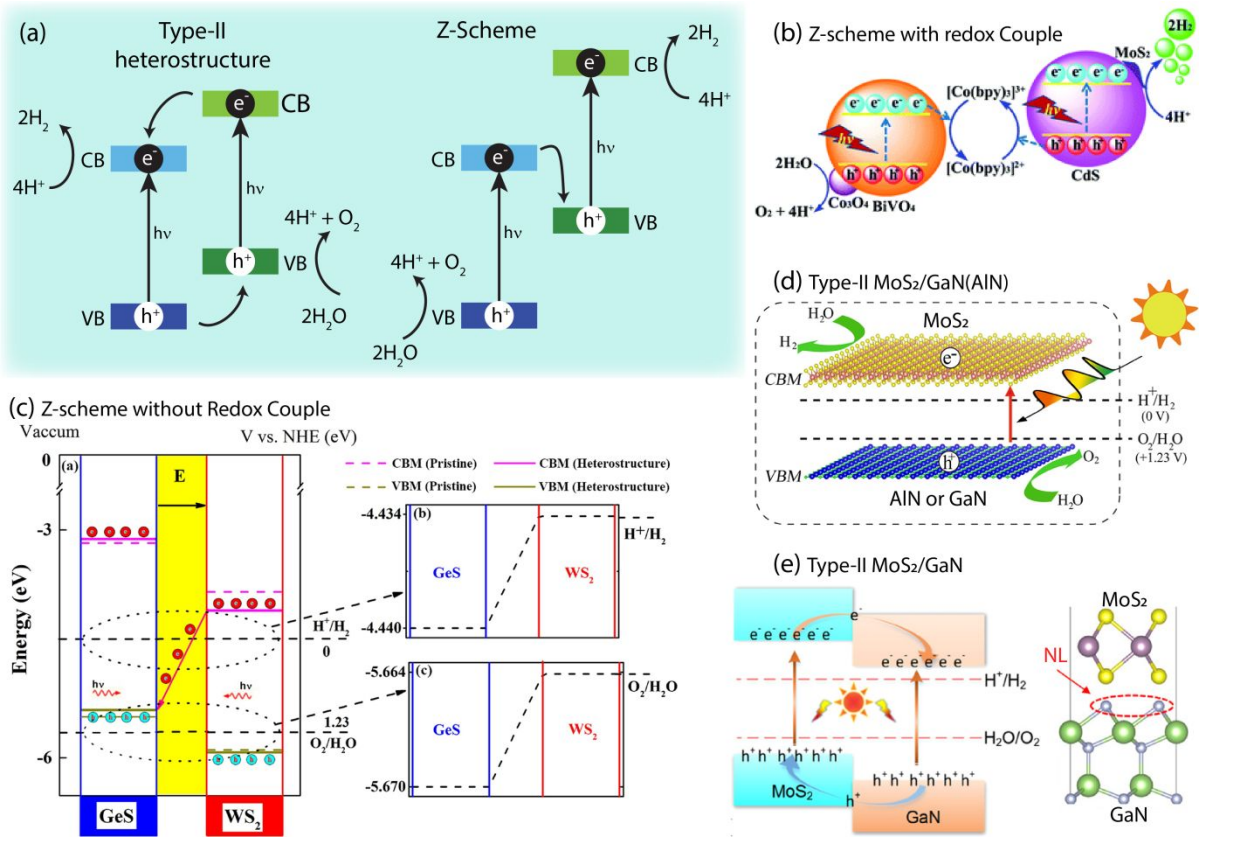

Figure 37. (a) Schematic showing the difference between a Type-II heterostructure and a Z-scheme. (b) Schematic of a Z-scheme emphasizing the redox couple that connects the two semiconductors.[336] Republished with permission of Royal Society of Chemistry, from ref. 336; permission conveyed through Copyright Clearance Center, Inc. (c) Heterostructure between GeS and WS_2 where the band gap decreases when the 2D layers are interfaced and an internal electric field drives charge separation for HER at GeS and OER at WS_2.[337] Reprinted with permission from ref. 337. Copyright 2018 by Elsevier. (d) Schematic of photocatalytic water splitting for MoS_2/GaN, where HER occurs at the MoS_2 side (top) and OER at the nitride side (bottom).[338] Reprinted with permission from ref. 338. Copyright 2014 American Chemical Society. (e) Contradicting theoretical/experimental work predicts that the MoS_2/GaN would have HER on the GaN side and OER on the MoS_2 side, where the interface is optimized by including a nitridation layer (NIL).[339] Reprinted with permission from ref. 339. Copyright 2018 American Chemical Society.

Another way to suppress carrier recombination is to create heterojunction systems where charge separation results in OER/HER evolution from different components within a hybrid system. This can be accomplished by Type-II band alignment of two semiconductors or creating a "Z-scheme", where the conduction band of one semiconductor is typically close in energy to the valance band of the other semiconductor. As illustrated in Figure 37a, Z-schemes offer the advantage of higher oxidation and reduction potentials compared to a typical Type-II heterojunction. Figure 37b shows an example of a Z-scheme in which MoS_2 nanosheets on CdS are used for HER, and $Co_3O_4/BiVO_4$ are used for OER, where the two half reactions are connected by a $[Co(bpy)_3]^{3+}/[Co(bpy)_3]^{2+}$ redox couple.[336] This system produced 14.5 and 7.1 μmol/h of H_2 and O_2, respectively, for 12 h with a quantum yield of 1.04%. This is a noble-metal-free Z-scheme for water splitting, where the CdS and $BiVO_4$ are the light absorbers and charges are transferred to the MoS_2 and Co_3O_4 catalysts. The large driving force for electron transfer from CdS to MoS_2 (~0.77 eV) and hole transfer from $BiVO_4$ to $Co3O_4$ enables the overall water splitting.

While some Z-schemes involve a redox couple between the HER and OER photocatalysts (e.g. Figure 37b), there is interest in eliminating the redox mediator and creating two-component Z-schemes with the semiconductors in direct contact. For example, Ju et al. investigated several GeS/WX_2 systems (X = O, S, Se, Te) and calculated that only GeS/WS_2 has proper band alignment for photocatalytic water splitting.[337] The authors suggest that this system forms a Z-scheme as indicated in Figure 37c, where HER occurs at the GeS CB and OER occurs at the WS_2 VB. Interestingly, the authors suggest that the Z-scheme is possible because ground-state charge transfer across the GeS/WS_2 heterojunction generates an internal electric field perpendicular to the interface that prevents relaxation of photoexcited electrons from the GeS CB to the WS_2 CB and relaxation of photoexcited holes from the WS_2 VB to the GeS VB.

In addition to Z-schemes, Type-II heterojunctions have also been investigated for TMDC-based water splitting systems. For example Liao et al. predicted that MoS_2/AlN or MoS_2/GaN would be good photocatalysts for water splitting.[338] The calculated energetics predict that HER would occur on the MoS_2 side and OER on the nitride side (Figure 37d). However, this 2014 report is contradicted by a 2017 report by Zhang et al. that construct MoS_2/GaN band diagrams using X-ray photoelectron spectroscopy data to conclude that HER occurs on the nitride side and OER on the MoS_2 side (Figure 37e).[339] Zhang et al. also suggest that the interface could be optimized by adding a nitridation layer (NIL, Figure 37e). A recent 2019 report calculated the energetic shifts with the GaN surface termination at the MoS_2 interface and found changes to the band structure where the interface energetics depended on the number of MoS_2 layers.[340] However, these theoretical reports have yet to be experimentally verified and photocatalytic experiments should be conducted to verify the charge separation and half reactions at the interface.

Other Type-II TMDC heterostructures are also productive for water splitting. For example, Type-II TMDC/carbon nitride heterostructures take advantage of the high catalytic activity of TMDCs, the abundant active area of carbon nitrides, and the long-term stability of both nanomaterials.[341-344] Theoretical predictions suggest that C_2N/WS_2 interfaces form Type-II heterostructures with the correct energetics to photocatalytically split water.[342] In the photoexcited system, electrons transfer to C_2N and holes to WS_2, enabling water oxidation on the WS_2 side and proton reduction on the C_2N side.

Despite the predicted ability of MoS_2/carbon nitride systems to carry out overall water splitting, experimental demonstrations are thus far focused on the hydrogen evolution half reaction in this hybrid system.[341, 344-346] Indeed, we note that it is often challenging to design one system that performs both HER and OER, so an alternative strategy is to separate the half reactions and

optimize each half reaction individually. Several studies have reported photocatalytic hydrogen evolution in WS_2/graphitic carbon nitride (g-C_3N_4)[345-346] and MoS_2/g-C_3N_4,[341, 344] which has been attributed to charge separation across the interface that suppresses recombination and extends carrier lifetimes. Interestingly, Figure 38 shows that g-C_3N_4 with 0.01 wt% loading of WS_2 was found to outperform the same loading of Pt catalyst, which suggests that TMDC-based heterojunctions may be a viable route toward avoiding expensive and scarce noble metal photocatalysts.[346] Indeed, other TMDC-based systems have also shown improved performance compared to Pt-loaded systems, such as $CuInS_2$ photocatalysts with 3 wt% MoS_2 loading.[347] Photoinduced charge separation is also suggested to occur in this system based on significant improvement (28x) in HER for hybrid MoS_2/$CuInS_2$ compared to the separated components.

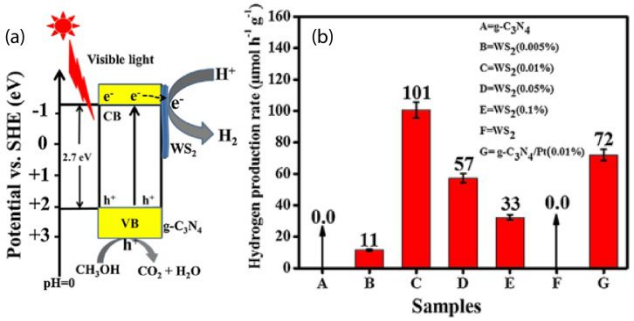

Figure 38. (a) Schematic of g-C_3N_4 with WS_2 co-catalyst to enhance H_2 evolution. (b) Hydrogen production rates for different samples, where 0.01 wt% loading of WS_2 on g-C_3N_4 gave the highest rate. The samples include A=g-C_3N_4, B=WS_2(0.005%), C=WS_2(0.01%), D=WS_2(0.05%), E=WS_2(0.1%), F=WS_2, G=g-C_3N_4/Pt(0.01%).[346] All panels are reprinted with permission from ref. 346. Copyright 2015 by Elsevier.

Photocatalytic HER in TMDC/g-C_3N_4 systems have also been explored using 1T/1T' metallic phase TMDCs. In dark electrochemistry, the metallic (1T/1T') phase of TMDCs have been shown to outperform the semiconducting phase for HER due to an increase in catalytic sites on the basal plane;[348-350] therefore, the 1T/1T' TMDCs can also contribute to HER in hybrid systems. 1T WS_2/g-C_3N_4 outperformed semiconducting 2H WS_2/g-C_3N_4 due to the lack of active sites on the 2H phase basal plane.[25] Photoexcitation of the g-C_3N_4 transfers photogenerated electrons to WS_2, and the high electrical conductivity on the metallic WS_2 improves charge

transport and HER. A similar conclusion was reached for MoS_2 on nitrogenated graphene oxide, where the metallic MoS_2 outperformed the semiconducting MoS_2.[351]

The potential advantages of using metallic 1T TMDCs for hybrid reduction systems are not limited to g-C_3N_4. This concept can be leveraged in mixed-phase TMDC layers for solar water splitting. Peng et al. exfoliated single-layer MoS_2 and prepared heterostructures containing the semiconducting (2H), metallic (1T), and quasi-metallic (1T'—where the small band gap material still behaves very similar to the metallic phase) states and performed photo-initiated HER.[129] They found that a monolayer heterostructure of semiconducting and quasi-metallic MoS_2 is photoactive for HER. The semiconducting portion of the monolayer absorbs light and the photogenerated electron transfers to the metallic portion (Figure 39a), where the interface between the two phases drives the charge separation and the basal sites of the metallic MoS_2 enable HER. Alternatively, MoS_2 can be partially converted from the semiconducting to the metallic phase by incorporating supercritical CO_2, after which the metallic phase demonstrated improved photoelectrochemical production of O_2 from H_2O oxidation.[109] These examples demonstrate how sensitive TMDCs are to their environment and how they can be used in various capacities.

Mahler et al. also demonstrated increased photocatalytic H_2 evolution of TiO_2 nanoparticles by adding metallic (1T) WS_2 nanosheets as a co-catalyst.[352] However, when semiconducting (2H) WS_2 nanosheets are added to TiO_2 nanoparticles, the HER activity decreased (Figure 39b). The authors attributed the difference in co-catalyst performance to the band energetics shown in Figure 39c. That is, electron transfer from the photoexcited TiO_2 to 1T WS_2 has a favorable driving force for charge separation, while it is unfavorable to transfer electrons to 2H WS_2. The authors further suggest that 2H WS_2 introduces recombination centers for photoexcited TiO_2 electrons and holes.

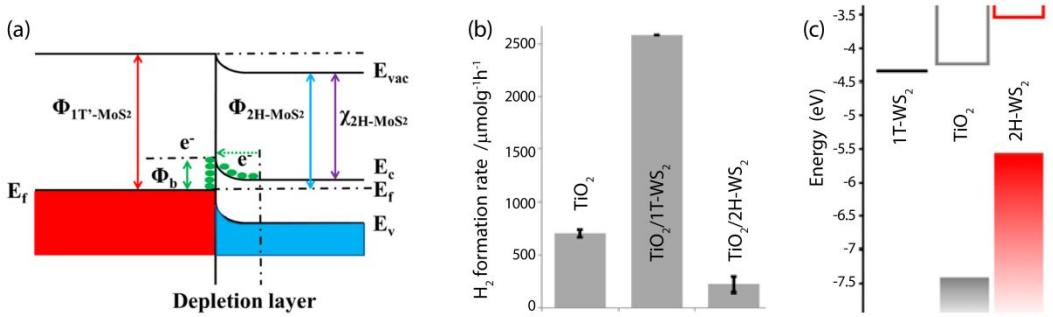

Figure 39. (a) Band diagram of mixed-phase MoS_2: (left, red) metallic/quasi-metallic and (right, blue) semiconducting. Photoexcited electrons from the semiconducting portion of MoS_2 transfer to the metallic MoS_2 phase and enhance HER.[129] Reprinted with permission from ref. 129. Copyright 2016 American Chemical Society. (b) The H_2 formation rate and (c) band energetics for TiO_2 with WS_2 co-catalyst in the metallic (1T) or semiconducting (2H) state.[352] Panels (b) and (c) are reprinted with permission from ref. 352. Copyright 2014 American Chemical Society.

Given the successful demonstration of PCT in TMDC/QD systems (Section 10), these systems have also been demonstrated for HER and overall water splitting. As an example, HER can be achieved from CdS QDs coupled with WS_2 nanosheets.[288, 353] The QD size can be tuned to create proper band alignment with the TMDC conduction band, which allows for electron transfer from the photoexcited CdS to WS_2. The optimal QD size of 7 – 8 nm diameter resulted in 14 mmol/h H_2 evolved with 58% quantum efficiency at 420 nm excitation (Figure 40a). Another report similarly coupled TMDCs to CdS for HER by integrating WS_2-MoS_2 nanosheets with CdS nanorods.[354] They found superior H_2 generation in the dual-TMDC/CdS nanorods (209.79 mmol g^{-1} h^{-1} H_2) in comparison to WS_2/CdS nanorods (169.82 mmol g^{-1} h^{-1} H_2) and MoS_2/CdS nanorods (123.31 mmol g^{-1} h^{-1} H_2)(Figure 40b). Notably, this system outperformed Pt/CdS nanorods (34.98 mmol g^{-1} h^{-1} H_2). The authors suggest that the increased H_2 generation was due to photoinduced charge separation within the dual-TMDC co-catalyst (Figure 40c).

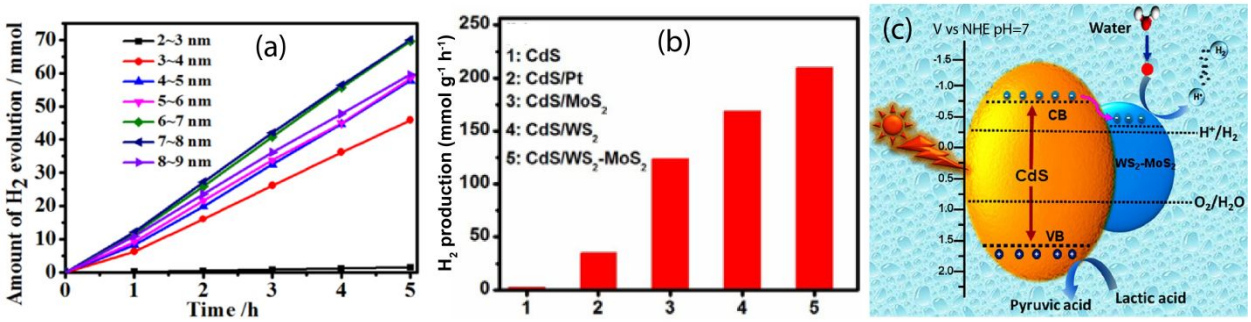

Figure 40. (a) Amount of H_2 evolved as a function of CdS QD size when coupled to WS_2 nanosheets.[288] Reprinted with permission from ref. 288. Copyright 2017 Elsevier. (b) WS_2-MoS_2 co catalysts for CdS nanorods show superior HER activity compared to the other tested configurations. (c) Schematic of photoexcited CdS charge transfer to WS_2-MoS_2 for H_2 generation.[354] Reprinted with permission from ref. 354. Copyright 2017 Wiley.

Producing H_2 with near-infrared (NIR) photoexcitation is an exciting avenue because it utilizes a lower energy portion of the solar energy spectrum. For example, 2D black phosphorous (BP) absorbs NIR light (Figure 41a), and heterojunctions between BP and WS_2 were found to generate 21 and 50 times greater amount of H_2 compared to the bare WS_2 and BP counterparts, respectively (Figure 41b).[355] The increased HER activity is attributed to charge separation at the 2D interface. The photocurrent response is greater, and the interfacial electron transfer is faster with IR irradiation for the black phosphorous/WS_2 interface. The transient absorption spectroscopy of BP only and BP/WS_2 heterojunction had lifetimes of 241 ps and 90.4 ps, respectively, where the faster lifetime of BP/WS_2 is attributed to the electron transfer from BP to WS_2.

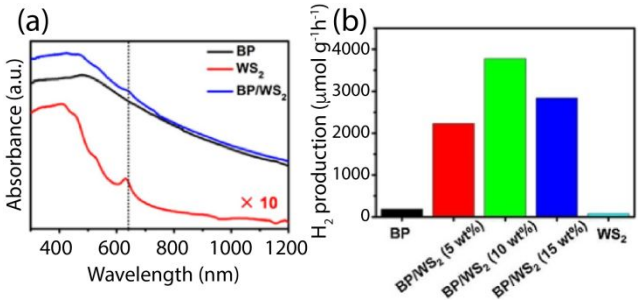

Figure 41. (a) 2D black phosphorous (BP)/WS_2 can be photoexcited in the near-infrared (NIR) region. (b) NIR excitation leads to significantly increased H_2 production over the isolated 2D materials.[355] All panels are reprinted with permission from ref. 355. Copyright 2018 Elsevier.

Although a greater number of systems have been studied for HER, OER is also challenging and requires attention. Pesci et al. studied MoS_2/WS_2 photoanodes for OER,[356] observing photoinduced water oxidation to O_2 and an n-type photocurrent of 0.45 mA/cm^2. They found a 10-fold increase in incident-photon-to-current-efficiency (~0.1% at 600 nm) in the hybrid system versus separate MoS_2 or WS_2 exfoliated nanosheets. The authors attribute this increased performance to improved charge carrier lifetime *via* charge separation at the MoS_2/WS_2

heterojunction. This same group expanded the study in 2019 to include salt-water oxidation using CVD grown large-area MoS_2/WS_2, where they found that reducing defect density improved OER efficiency.[357] This interface creates an incident photon conversion efficiency of 1.6% and photocurrent density of 1.7 mA/cm^2, an order of magnitude improvement over exfoliated 2D interfaces. The authors attribute the observation of reduced charge recombination and better OER performance for the CVD-grown architecture to lower edge site density and atomically sharp and clean interfaces.

12.2 *Functionalization and Strain*

Methods such as TMDC surface functionalization and modifying internal strain can impact both the ability of the TMDC system to split water and the interfacial interactions and energetics in hybrid systems that undergo PCT. Adding surface functional groups to TMDCs has been shown to alter the optoelectronic and catalytic properties because the surface energetics can be tuned and/or catalytic sites blocked.[229] Functional groups can be physisorbed to the surface or covalently bound via basal and/or edge sites, which affect the properties differently.[229] For example, theoretical studies by Pan et al. suggest that $C_6H_5CH_2NH_2$ functionalized MoS_2 structures are good candidates for photoelectrical water splitting.[358] The calculated energetics for bare MoS_2 are not favorable for overall water splitting; however, the energetics can be tuned by putting a dipole on the surface. For most coverages studied, $C_6H_5CH_2NH_2$ on MoS_2 properly tuned the energetics for water splitting whereas C_6H_5CN was only good for water splitting at 18.75% coverage (Figure 42a). Suo et al. further calculated the band energies of MoS_2 with other physisorbed organics (C_6H_5COOH and $C_6H_5OCH_3$) in addition to $C_6H_5CH_2NH_2$ and C_6H_5CN at various coverages.[359] They calculated better energetic alignment for overall water splitting (Figure 42b) along with improved absorption and photoinduced charge separation with the organic layer. Note that in both

the Pan and Suo et al. calculations,[358-359] the MoS_2 is calculated to have band energetics that are not favorable for HER or overall water splitting which contradicts other theoretical reports (e.g., Figure 7).

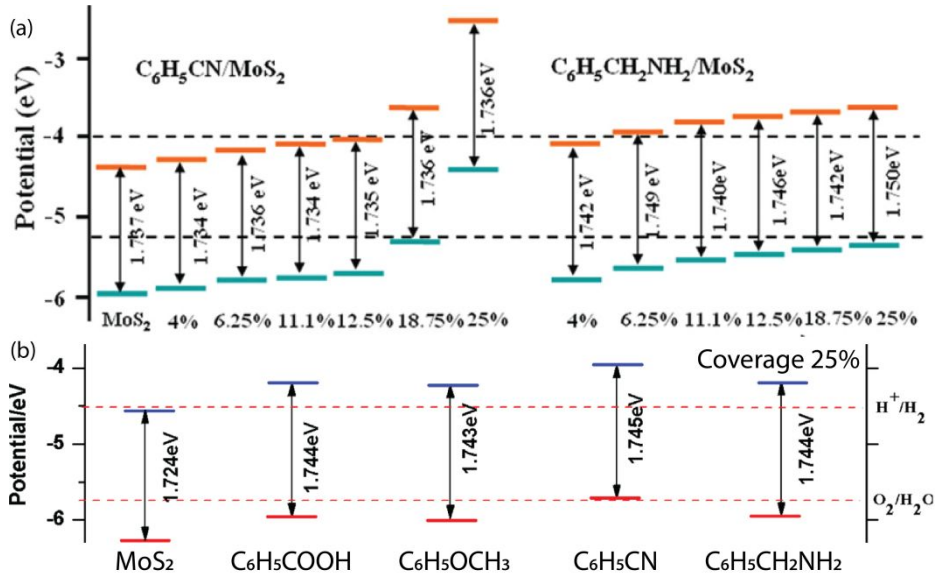

Figure 42. (a) Band energetics of MoS_2 and MoS_2 functionalized with C_6H_5CN and $C_6H_5CH_2NH_2$ at various coverages.[358] Republished with permission of Royal Society of Chemistry, from ref. 358; permission conveyed through Copyright Clearance Center, Inc. (b) Band energetics for MoS_2 and MoS_2 functionalized with 25% coverage of various organic molecules.[359] Reprinted with permission from ref. 359. Copyright 2018 Elsevier.

Similar to the ability to tune band energies with functionalization, strain engineering in both vertical and lateral dimensions has attracted interest as a strategy to alter band positions, improve conductivity, and modify surface interactions.[360] For example, bending strain in MoS_2 scrolls fabricated by Hwang et al. was suggested to induce a 2H/1T transition that resulted in improved catalytic activity for HER.[361] Mechanical strain in MoS_2 has been suggested to activate the basal plane and improve hydrogen evolution through strained S vacancies.[362] Pak et al. also suggested that strain can mediate the interlayer coupling between MoS_2 and WS_2 layers, which could have important implications for optimizing carrier generation in heterojunction systems (Figure 43a).[363]

In addition to mechanically-induced strain, a report by Carroll et al. suggests that strain in TMDCs can be induced by an external voltage.[364] Using in-situ spectroelectrochemistry, the authors correlated the change in exciton absorption with structural information from Raman spectroscopy, concluding that MoS_2 becomes more strained and transitions to a lower bandgap material under applied potential. This study suggests differences between the dynamic response of an ideal p-type semiconductor electrode versus a 2D layered p-type MoS_2 electrode, which is insightful for understanding TMDC electrochemical catalytic reactions (Figure 43b).

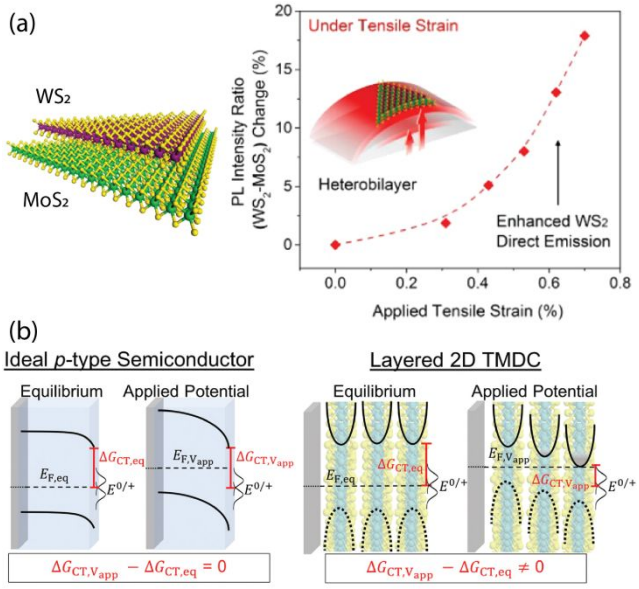

Figure 43. (a) WS_2/MoS_2 heterojunctions (left) are influenced differently by tensile and compressive strain, where tensile strain enhances WS_2 direct emission compared to MoS_2 (right).[363] Reprinted with permission from ref. 363. Copyright 2017 American Chemical Society. (b) Band energetics for an ideal p-type semiconductor (left) and 2D MoS_2 (right) photoelectrode at equilibrium and while applying a potential. The TMDC photoelectrode shows different PCT driving force with applied potential due to a change in band edge positions.[131] Republished with permission of Royal Society of Chemistry, from ref. 131; permission conveyed through Copyright Clearance Center, Inc.

12.3 2D protection layers for photoelectrodes

Protecting Si and other photoelectrodes during catalytic reactions is important for improved and durable catalytic performance, in particular for HER in acidic conditions. For example, few-layer $MoSe_2$ was shown to protect high-efficiency Si photoanodes, where 3 nm of $MoSe_2$ was grown by molecular beam epitaxy (MBE) on a p+-n Si substrate.[365] The applied bias photon-to-current

efficiency at ~0.5 V vs. RHE increased from <0.1 % to 13.8 % with the $MoSe_2$ layer. The protected photoanode had a stable current density of 2 mA/cm^2 for ~14 hours at 0.38 V vs. RHE under AM 1.5G one sun illumination. Similarly, Si photoanodes have been protected with MoS_2. By preparing a layering of $MoS_2/MoO_x/Mo_xSi/SiO_2$ on Si, the Si photoanode was protected for up to 2 months when operating under acidic conditions.[366] Eventually the MoS_2 becomes oxidized and no longer present as MoS_2, which likely leads to the failure of the photoanode. These conclusions are in agreement with earlier work by Laursen et al. which also demonstrated additional stability of Si photocathodes with a MoS_2 protection layer.[367]

Metallic MoS_2 has also been shown to enhance HER of p-type Si photoelectrodes by driving electrons to the surface and providing catalytic sites.[368] Ding et al. achieved 17.6 mA/cm^2 at 0 V vs RHE under 1 Sun illumination and found long term stability (23% decrease in current density over 3 hours).[368] They compared CVD-1T MoS_2 versus chemically-exfoliated 1T MoS_2 nanosheets and found that CVD-1T MoS_2 was far superior to exfoliated MoS_2 (Figure 44a). They attribute the difference to lower charge-transfer resistance, both at the interface between CVD-grown 1T MoS_2 and the Si substrate and at the MoS_2-electrolyte interface. Using surface photoresponse spectroscopy, the authors showed slow carrier recombination at the CVD 1T MoS_2/Si interface (Figure 44b).

Recently, Si nanowires have been improved and stabilized by 2D NbS_2 nanosheets, which are group V TMDCs.[369] In addition to >10,000 s stability in strong acid medium, adding NbS_2 co-catalysts to Si nanowires generated a 300 mV anodic shift for photocatalysis and H_2 evolution, where the onset potential is 0.34 eV vs RHE (Figure 44c). The improved NbS_2-Si nanowires hybrid PEC performance is 20x and 5x greater than bare Si nanowires and the NbS_2/Si structure,

respectively (Figure 44d). NbS_2 provides a lower energy barrier for HER and increases the carrier separation and transport within the hybrid structure.

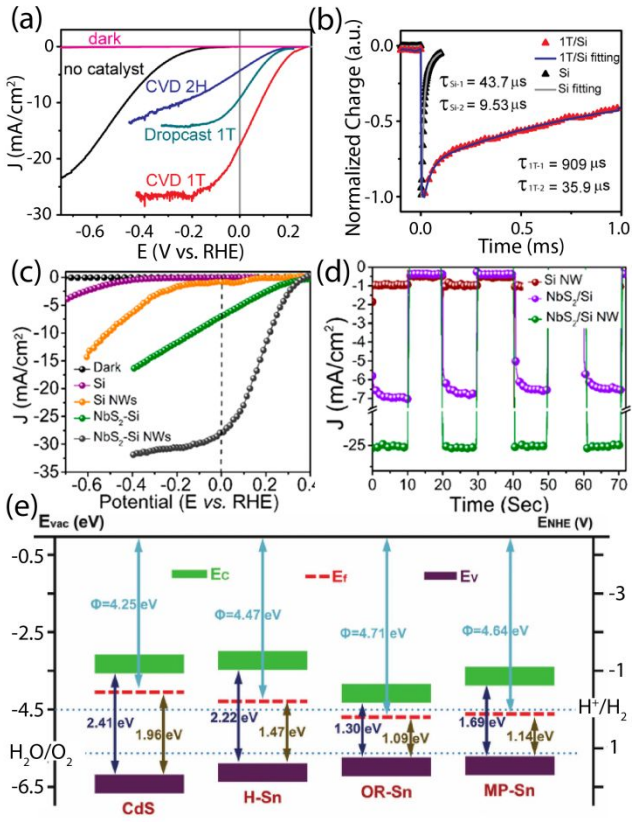

Figure 44. (a) Metallic (1T) MoS_2 interfaced with p-type Si enhances HER and is more durable than p-type Si only. CVD 1T MoS_2 has better HER performance than chemically exfoliated 1T MoS_2. (b) Time-resolved surface photoresponse spectroscopy yields the carrier recombination times that are slower for CVD 1T MoS_2/Si than Si only that leads to better HER performance.[368] Panels (a) – (b) are reprinted with permission from ref. 368. Copyright 2014 American Chemical Society. (c) NbS_2/Si nanowires for improved photoelectrochemistry. Linear sweep voltammetry curves for photoinduced HER show that the NbS_2/Si nanowires give the lowest overpotential. (d) Photoresponse of the NbS_2/Si nanowires gives the highest current density and is stable over many cycles.[369] Panels (c) – (d) are reprinted with permission from ref. 369. Copyright 2019 American Chemical Society. (e) Measured band energies of CdS nanowires and different phases of SnS_X, where H is hexagonal SnS_2, OR is orthorhombic SnS, and MP is mixed phases of orthorhombic and zinc blende.[370] Reprinted with permission from ref. 370. Copyright 2018 Wiley.

CdS nanowires should have the proper band energetics for HER (Figure 44e), but they do not produce a stable photoanode and corrode by holes accumulating at the surface.[370] However, Fu et al. have interfaced CdS nanorods with SnS_X nanosheets to improve the HER by reducing hole accumulation.[370] The authors explored the effect of tuning SnS_X nanosheet phase from hexagonal SnS_2 (band gap ~2.4 eV) to orthorhombic SnS (band gap ~1.0 – 1.5 eV) to mixed phases

of orthorhombic/zinc blende SnS (band gap ~1.72 – 1.76 eV). Figure 44e summarizes how the different phases control the band alignment to decrease hole accumulation in CdS. The SnS orthorhombic phase forms a Type-I band alignment with CdS and does not remove holes from the CdS, but both hexagonal and mixed phase SnS_X have Type-II band alignment that separates charge. Of these two, the authors conclude that the hexagonal phase is the best for water splitting due to a larger driving force for both electron and hole transfer. The hexagonal phase SnS_2/CdS photoanodes demonstrated IPCE of 31.5% at 340 nm and current density of 1.59 mA/cm^2 at 1.23 V vs. RHE, performing stably over 2 hours of testing.

12.4 Plasmon Interactions

Plasmon interactions can be used to enhance the local electric field around nanoscale metallic features, with possible implications for improving photocatalysis. For example, Chen and Cronin et al. found enhanced photocatalysis in a system of WSe_2 coupled to 5 nm Au nanoislands.[371] They observed 7x enhancement of the photocurrent (20 nA to 140 nA) over bare WSe_2 and large charge-separating fields over the monolayer. The surface area of WSe_2 decreased by 70%, but the overall photoconversion efficiency improved from 3.5 to 24.7 % due to effective coupling of incident light by the Au plasmons.

Plasmons have also been shown to enhance OER for MoS_2 photoandoes.[372-374] Figure 45a shows an example of Au plasmons enabling electron transfer and charge separation.[374] In this study, Xu et al. showed that Au plasmons improved OER in MoS_2 nanosheets on carbon fiber cloth. The Au plasmons modified band bending at the interface between MoS_2 and the carbon fiber cloth, eliminating the barrier for electron transfer from MoS_2 to the electrode (Figure 45a). Photoconversion efficiency improved up to 1.27%, with 10 mA/cm^2 at 1.23 V vs. RHE. Pan et al. showed plasmon-enhanced OER in MoS_2 using a p-n heterojunction photoelectrode with

$MoS_2/BiVO_4$ coupled to Ag plasmons (Figure 45b and 45c).[375] This system produced 2.72 (4.02) mA/cm^2 photocurrent at 0.6 V (1.23 V) vs. RHE, with IPCE of 51% at 420 nm. The $BiVO_4$–Ag – MoS_2 configuration outperformed all other tested configurations, where the next best performing configuration was $BiVO_4$–Ag (~1.7 mA/cm^2 at 0.6 vs. RHE and 32% IPCE at 420 nm).

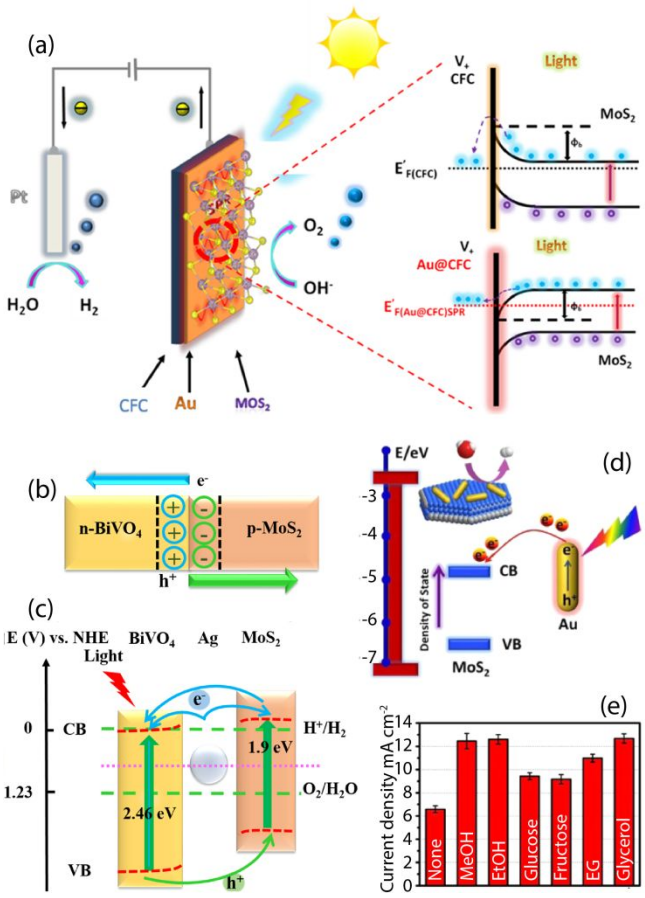

Figure 45. (a) Au plasmons coupled to MoS_2 nanosheets enhance OER compared to MoS_2 without Au plasmons due to better electron transfer to the carbon fiber cloth (CFC) and charge separation at the electrode/electrolyte interface.[374] Reprinted with permission from ref. 374. Copyright 2017 American Chemical Society. (b) Schematic of charge separation at $BiVO_4/MoS_2$ heterojunctions with Ag plasmons. (c) The band alignment enables OER at the MoS_2 side and electron transfer to the electrode assembly through $BiVO_4$, with Ag plasmons enhancing OER activity.[375] Panels (b) – (c) are reprinted with permission from ref. 375. Copyright 2018 American Chemical Society. (d) MoS_2 coupling to Au nanorods improves HER performance and photocurrent density. (e) The MoS_2 photocurrent can be further enhanced if a hole scavenger is used.[376] Panels (d) – (e) are reprinted with permission from ref. 376. Copyright 2015 American Chemical Society.

Researchers have also coupled plasmons to TMDCs for HER. For example, Figure 45d shows enhanced HER for MoS_2 nanosheets attributed to hot electron injection from Au

nanorods.[376] The MoS_2/Au nanorods show ~3-fold increase in current density at 808 nm illumination (~6 mA/cm^2) compared to the dark current (~2 mA/cm^2), whereas the MoS_2 produces very little photocurrent at 808 nm. The authors showed that hole scavengers further increase HER activity (Figure 45e), where the current density nearly doubles when using methanol, ethanol, or glycerol hole scavengers. They attributed this enhanced photocurrent generation to decreased charge recombination and increased photogenerated electron lifetimes.

13. Future Prospects

In this review, we highlighted PCT properties at TMDC hetero-interfaces that can enable TMDCs to be used in quantum computers, photodetectors, photovoltaics, and water splitting. However, practical TMDC-based devices are still in nascent stages of development, and additional lengths will have to be taken to effectively harness their unique photophysics on larger scales. Here, we've discussed how the fundamental properties of TMDCs—such as band energetics, the types and lifetimes of quasi particles, spin and valley degrees of freedom, and crystal structure—must be leveraged to improve photoinduced charge generation at interfaces with a goal of enabling functional devices. We further identified interfacial PCT driving force and kinetics as important factors for optimizing carrier separation, which can be achieved by changing the components on each side of the interface. To this end, we discussed various promising TMDC heterojunctions: TMDCs coupled to other TMDCs, organic semiconductors (small organic molecules, polymers, and single-walled carbon nanotubes), quantum dots, perovskites, and electrolyte solutions. While each class of materials has unique challenges and target applications, in all cases researchers strive to optimize the interface to achieve performance metrics such as high photocurrent response, suitable voltages, long-lived carriers, wavelength-specific photoresponse, durable operation, and spin selectivity.

At this early stage of development, practical challenges remain for the future prospects of TMDCs in device applications. Most studies thus far investigate photophysical processes on small spatial scales and under well-controlled environmental conditions. In reality, the developing state of synthetic methods often results in spatial variations in active material properties (e.g. defect states, doping, layer thickness, crystal structure, and band gap), where many of these factors can simultaneously affect performance as device sizes increase. Fabrication of heterojunctions further complicates syntheses, especially when the device geometry requires TMDCs to be grown on top of the heterojunction material rather than onto a standard substrate. External environment and atmospheric conditions also drastically affect photophysics and the resulting performance metrics of ultrathin TMDCs.[230, 377] In some cases, this environmental sensitivity can be harnessed to create gas detectors and humidity sensors,[230, 377] but in other cases it may have less-desirable effects for energy conversion. Furthermore, differing dielectric properties of device-relevant layers like electrodes or encapsulants may impact the mix of TMDC excited states, phase, and conductivity.[230] While fundamental studies are important to benchmark the impacts of TMDC inhomogeneities, heterojunction material interactions, and atmospheric or chemical exposure, development of real-world devices will depend on long-term strategies for controlling their fabrication, stabilization, encapsulation, and operating environment/temperature.

Despite these challenges, the studies outlined in this review have shown great strides toward functional photoresponsive TMDC-based heterojunction devices on the lab scale. As outlined in Section 12, both photocatalytic hydrogen and oxygen evolution from water splitting have been achieved with visible light at reasonable over-potentials for a wide range of different TMDC nanostructures and heterojunctions. TMDC heterojunctions have similarly shown promise in photocatalytic CO_2 reduction,[326-328, 378-379] and N_2 reduction.[380-381] These results promise cost-

saving advantages if efficiencies are improved and TMDCs can be used as effective photocatalysts (for example to overcome the scarcity and high cost of Pt that currently limits the spread of water splitting technology). However, further development based on the fundamental principles identified in this review is needed to design efficient TMDC-based Type-II or Z-scheme systems for overall water splitting without the use of sacrificial agents.

In photovoltaics, the use of 2D TMDCs as active absorber layers has thus far been limited to low overall efficiencies (~0.1-10%), though these devices offer advantages worth further pursuing such as the ultrathin, semi-transparent nature, high thickness-normalized performance, and good stability. While some studies in this review have shown that texturing and plasmonic effects can enhance absorption even in ultrathin layers,[274] lower current densities in semi-transparent devices are to some extent acceptable. However, significant effort is still needed to increase voltages and improve charge collection from the lower percentage of photons that are absorbed. Creating heterojunctions to decrease recombination and extend carrier lifetimes is an important step toward these goals. While several heterojunctions have been tested for photovoltaics and photodetectors (Sections 8-11), further effort is needed to address the fundamental phenomena behind the wide variation in literature results that can be obtained even for nominally similar heterostructures.

2D TMDCs are also promising candidates for the rapidly emerging fields of neuromorphic and quantum computing. Neuromorphic computing attempts to emulate the nonlinear dynamical functions of the brain by using materials that can transform small electrical or optical inputs into large conductance modulations with fast switching speeds and tunable conductance lifetimes (volatility). While TMDCs have been explored for a broad variety of electrically-induced switching behaviors, recent studies have begun exploring ways in which optical switching in

TMDC-based heterojunctions can enable synaptic or neuronal emulation.[297, 382] It will be critical to understand and manipulate dynamic excited-state processes in TMDC heterojunctions to fully exploit the rapid switching and persistent photoconductivity needed to enable complex neuromorphic functions, and the field is just beginning to take on these challenges. Quantum information processing relies upon the manipulation of quantum-mechanical phenomena to perform computations, communication, encryption, and simulations. A critical component for quantum information processing is the spin-photon interface where quantum information can be transformed between these two degrees of freedom.[383] Such interfaces are attractive applications for TMDCs, due to the inherent spin-valley locking of TMDCs, whereby the valley pseudo-spin is directly tied to the photon circular polarization (Sections 8.3 and 8.4). Heterojunctions are viewed as particularly promising for achieving the long valley coherence lifetimes needed to enable practical quantum information applications such as quantum logic gates and quantum repeaters.[384] As the field moves forward, some key advances will be to improve valley coherence lifetimes via efficient photoinduced charge separation and to further increase operation temperatures to avoid the energy impact of cryogenic operation.

Overall, 2D TMDC-based heterojunctions are proving to be promising components in future energy harvesting, energy storage, and computational applications, where photogenerated charges need to be directed through a device to perform work or retain memory. The strategy of engineering PCT from a standpoint of controlling the fundamental photophysics in TMDC-based heterostructures will continue to serve an important role in the rational design of high-performance quantum-confined systems.

Conflicts of Interest

There are no conflicts of interest to declare.

Acknowledgement

This work was authored by the National Renewable Energy Laboratory, operated by Alliance for Sustainable Energy, LLC, for the U.S. Department of Energy (DOE) under Contract No. DE-AC36-08GO28308. Funding provided by the U.S. DOE, Office of Science, Office of Basic Energy Sciences, Division of Chemical Sciences, Geosciences, and Biosciences, Solar Photochemistry Program. The views expressed in the article do not necessarily represent the views of the DOE or the U.S. Government. The U.S. Government retains and the publisher, by accepting the article for publication, acknowledges that the U.S. Government retains a nonexclusive, paid-up, irrevocable, worldwide license to publish or reproduce the published form of this work, or allow others to do so, for U.S. Government purposes.

References

1. K. F. Mak, C. Lee, J. Hone, J. Shan and T. F. Heinz, Atomically Thin MoS2: A New Direct-Gap Semiconductor, *Phys. Rev. Lett.,* 2010, **105**, 136805.
2. H. Zhao and F. Rosei, Colloidal Quantum Dots for Solar Technologies, *Chem,* 2017, **3**, 229-258.
3. X. Du, I. Skachko, A. Barker and E. Y. Andrei, Approaching Ballistic Transport in Suspended Graphene, *Nat. Nanotechnol.,* 2008, **3**, 491-495.
4. A. Javey, J. Guo, Q. Wang, M. Lundstrom and H. Dai, Ballistic Carbon Nanotube Field-Effect Transistors, *Nature,* 2003, **424**, 654-657.
5. H. Wang, C. Zhang and F. Rana, Surface Recombination Limited Lifetimes of Photoexcited Carriers in Few-Layer Transition Metal Dichalcogenide MoS2, *Nano Lett.,* 2015, **15**, 8204-8210.
6. M. Seo, H. Yamaguchi, A. D. Mohite, S. Boubanga-Tombet, J.-C. Blancon, S. Najmaei, P. M. Ajayan, J. Lou, A. J. Taylor and R. P. Prasankumar, Ultrafast Optical Microscopy of Single Monolayer Molybdenum Disulfide Flakes, *Sci. Rep.,* 2016, **6**, 21601.
7. W. Feng, Y. Yao, W. Zhu, J. Zhou, W. Yao and D. Xiao, Intrinsic Spin Hall Effect in Monolayers of Group-VI Dichalcogenides: A First-Principles Study, *Phys. Rev. B,* 2012, **86**, 165108.
8. X. Xu, W. Yao, D. Xiao and T. F. Heinz, Spin and Pseudospins in Layered Transition Metal Dichalcogenides, *Nat. Phys.,* 2014, **10**, 343-350.
9. J. R. Schaibley, H. Yu, G. Clark, P. Rivera, J. S. Ross, K. L. Seyler, W. Yao and X. Xu, Valleytronics in 2D Materials, *Nat. Rev. Mater.,* 2016, **1**, 16055.
10. N. Huo, Y. Yang, Y.-N. Wu, X.-G. Zhang, S. T. Pantelides and G. Konstantatos, High Carrier Mobility in Monolayer CVD-Grown MoS2 through Phonon Suppression, *Nanoscale,* 2018, **10**, 15071-15077.
11. Y. Liu, J. Guo, E. Zhu, L. Liao, S.-J. Lee, M. Ding, I. Shakir, V. Gambin, Y. Huang and X. Duan, Approaching the Schottky–Mott Limit in Van der Waals Metal–Semiconductor Junctions, *Nature,* 2018, **557**, 696-700.
12. S. Park, N. Mutz, T. Schultz, S. Blumstengel, A. Han, A. Aljarb, L.-J. Li, E. J. W. List-Kratochvil, P. Amsalem and N. Koch, Direct Determination of Monolayer MoS2 and WSe2 Exciton Binding Energies on Insulating and Metallic Substrates, *2D Mater.,* 2018, **5**, 025003.

13. D. M. Andoshe, J.-M. Jeon, S. Y. Kim and H. W. Jang, Two-Dimensional Transition Metal Dichalcogenide Nanomaterials for Solar Water Splitting, *Eletron. Mater. Lett.,* 2015, **11**, 323-335.
14. A. K. Singh, K. Mathew, H. L. Zhuang and R. G. Hennig, Computational Screening of 2D Materials for Photocatalysis, *J. Phys. Chem. Lett.,* 2015, **6**, 1087-1098.
15. M. M. Glazov, E. L. Ivchenko, G. Wang, T. Amand, X. Marie, B. Urbaszek and B. L. Liu, Spin and Valley Dynamics of Excitons in Transition Metal Dichalcogenide Monolayers, *physica status solidi (b),* 2015, **252**, 2349-2362.
16. J. G. Roch, G. Froehlicher, N. Leisgang, P. Makk, K. Watanabe, T. Taniguchi and R. J. Warburton, Spin-Polarized Electrons in Monolayer MoS2, *Nat. Nanotechnol.,* 2019, **14**, 432-436.
17. D. Canfield and B. A. Parkinson, Improvement of Energy Conversion Efficiency by Specific Chemical Treatments of Molybdenum Selenide (N-MoSe2) and Tungsten Selenide (N-WSe2) Photoanodes, *J. Am. Chem. Soc.,* 1981, **103**, 1279-1281.
18. R. Tenne and A. Wold, Passivation of Recombination Centers in N-WSe2 Yields High Efficiency (>14%) Photoelectrochemical Cell, *Appl. Phys. Lett.,* 1985, **47**, 707-709.
19. W. Kautek, H. Gerischer and H. Tributsch, The Role of Surface Orientation in the Photoelectrochemical Behavior of Layer Type D-Band Semiconductors, *Berichte der Bunsengesellschaft für physikalische Chemie,* 1979, **83**, 1000-1008.
20. S. Manzeli, D. Ovchinnikov, D. Pasquier, O. V. Yazyev and A. Kis, 2D Transition Metal Dichalcogenides, *Nat. Rev. Mater.,* 2017, **2**, 17033.
21. C. Tan, X. Cao, X.-J. Wu, Q. He, J. Yang, X. Zhang, J. Chen, W. Zhao, S. Han, G.-H. Nam, M. Sindoro and H. Zhang, Recent Advances in Ultrathin Two-Dimensional Nanomaterials, *Chem. Rev.,* 2017, **117**, 6225-6331.
22. G. Wang, C. Robert, A. Suslu, B. Chen, S. Yang, S. Alamdari, I. C. Gerber, T. Amand, X. Marie, S. Tongay and B. Urbaszek, Spin-Orbit Engineering in Transition Metal Dichalcogenide Alloy Monolayers, *Nat. Commun.,* 2015, **6**, 10110.
23. L. Yuan, T. Wang, T. Zhu, M. Zhou and L. Huang, Exciton Dynamics, Transport, and Annihilation in Atomically Thin Two-Dimensional Semiconductors, *J. Phys. Chem. Lett.,* 2017, **8**, 3371-3379.
24. J. Kim, C. Jin, B. Chen, H. Cai, T. Zhao, P. Lee, S. Kahn, K. Watanabe, T. Taniguchi, S. Tongay, M. F. Crommie and F. Wang, Observation of Ultralong Valley Lifetime in WSe2/MoS2 Heterostructures, *Sci. Adv.,* 2017, **3**, e1700518.
25. P. Rivera, H. Yu, K. L. Seyler, N. P. Wilson, W. Yao and X. Xu, Interlayer Valley Excitons in Heterobilayers of Transition Metal Dichalcogenides, *Nat. Nanotechnol.,* 2018, **13**, 1004-1015.
26. U. Rau, Reciprocity Relation between Photovoltaic Quantum Efficiency and Electroluminescent Emission of Solar Cells, *Phys. Rev. B,* 2007, **76**, 085303.
27. J. Nelson, *The Physics of Solar Cells*. Imperial College Press: London, 2003; p 384.
28. P. D. Cunningham, K. M. McCreary, A. T. Hanbicki, M. Currie, B. T. Jonker and L. M. Hayden, Charge Trapping and Exciton Dynamics in Large-Area CVD Grown MoS2, *J. Phys. Chem. C,* 2016, **120**, 5819-5826.
29. K. Chen, R. Ghosh, X. Meng, A. Roy, J.-S. Kim, F. He, S. C. Mason, X. Xu, J.-F. Lin, D. Akinwande, S. K. Banerjee and Y. Wang, Experimental Evidence of Exciton Capture by Mid-Gap Defects in CVD Grown Monolayer MoSe2, *npj 2D Mater. Appl.,* 2017, **1**, 15.

30. L. Li, R. Long, T. Bertolini and O. V. Prezhdo, Sulfur Adatom and Vacancy Accelerate Charge Recombination in MoS2 but by Different Mechanisms: Time-Domain Ab Initio Analysis, *Nano Lett.,* 2017, **17**, 7962-7967.
31. H. Nan, Z. Wang, W. Wang, Z. Liang, Y. Lu, Q. Chen, D. He, P. Tan, F. Miao, X. Wang, J. Wang and Z. Ni, Strong Photoluminescence Enhancement of MoS2 through Defect Engineering and Oxygen Bonding, *ACS Nano,* 2014, **8**, 5738-5745.
32. Y. Shi, O. V. Prezhdo, J. Zhao and W. A. Saidi, Iodine and Sulfur Vacancy Cooperation Promotes Ultrafast Charge Extraction at MAPbI3/MoS2 Interface, *ACS Energy Lett.,* 2020, 1346-1354.
33. G. Li, D. Zhang, Q. Qiao, Y. Yu, D. Peterson, A. Zafar, R. Kumar, S. Curtarolo, F. Hunte, S. Shannon, Y. Zhu, W. Yang and L. Cao, All the Catalytic Active Sites of MoS2 for Hydrogen Evolution, *J. Am. Chem. Soc.,* 2016, **138**, 16632-16638.
34. X. Wang, Y. Zhang, H. Si, Q. Zhang, J. Wu, L. Gao, X. Wei, Y. Sun, Q. Liao, Z. Zhang, K. Ammarah, L. Gu, Z. Kang and Y. Zhang, Single-Atom Vacancy Defect to Trigger High-Efficiency Hydrogen Evolution of MoS2, *J. Am. Chem. Soc.,* 2020, **142**, 4298-4308.
35. W. Xu, D. Kozawa, Y. Liu, Y. Sheng, K. Wei, V. B. Koman, S. Wang, X. Wang, T. Jiang, M. S. Strano and J. H. Warner, Determining the Optimized Interlayer Separation Distance in Vertical Stacked 2D WS2:hBN:MoS2 Heterostructures for Exciton Energy Transfer, *Small,* 2018, **14**, 1703727.
36. H. Li, X. Zheng, Y. Liu, Z. Zhang and T. Jiang, Ultrafast Interfacial Energy Transfer and Interlayer Excitons in the Monolayer WS2/CsPbBr3 Quantum Dot Heterostructure, *Nanoscale,* 2018, **10**, 1650-1659.
37. D. Kozawa, A. Carvalho, I. Verzhbitskiy, F. Giustiniano, Y. Miyauchi, S. Mouri, A. H. Castro Neto, K. Matsuda and G. Eda, Evidence for Fast Interlayer Energy Transfer in MoSe2/WS2 Heterostructures, *Nano Lett.,* 2016, **16**, 4087-4093.
38. T. Főrster, 10th Spiers Memorial Lecture. Transfer Mechanisms of Electronic Excitation, *Discussions of the Faraday Society,* 1959, **27**, 7-17.
39. D. B. Sulas, K. Yao, J. J. Intemann, S. T. Williams, C.-Z. Li, C.-C. Chueh, J. J. Richards, Y. Xi, L. D. Pozzo, C. W. Schlenker, A. K. Y. Jen and D. S. Ginger, Open-Circuit Voltage Losses in Selenium-Substituted Organic Photovoltaic Devices from Increased Density of Charge-Transfer States, *Chem. Mater.,* 2015, **27**, 6583-6591.
40. K. Vandewal, K. Tvingstedt, A. Gadisa, O. Inganäs and J. V. Manca, Relating the Open-Circuit Voltage to Interface Molecular Properties of Donor:Acceptor Bulk Heterojunction Solar Cells, *Phys. Rev. B,* 2010, **81**, 125204.
41. T. M. Burke, S. Sweetnam, K. Vandewal and M. D. McGehee, Beyond Langevin Recombination: How Equilibrium between Free Carriers and Charge Transfer States Determines the Open-Circuit Voltage of Organic Solar Cells, *Adv. Energy Mater.,* 2015, **5**, 1500123.
42. K. Vandewal, J. Widmer, T. Heumueller, C. J. Brabec, M. D. McGehee, K. Leo, M. Riede and A. Salleo, Increased Open-Circuit Voltage of Organic Solar Cells by Reduced Donor-Acceptor Interface Area, *Adv. Mater.,* 2014, **26**, 3839-3843.
43. K. Tvrdy, P. A. Frantsuzov and P. V. Kamat, Photoinduced Electron Transfer from Semiconductor Quantum Dots to Metal Oxide Nanoparticles, *Proc. Natl. Acad. Sci.,* 2011, **108**, 29-34.

44. J.-S. Chen, M. Li, Q. Wu, E. Fron, X. Tong and M. Cotlet, Layer-Dependent Photoinduced Electron Transfer in 0D–2D Lead Sulfide/Cadmium Sulfide–Layered Molybdenum Disulfide Hybrids, *ACS Nano,* 2019, **13**, 8461-8468.
45. Y. Kunai, A. T. Liu, A. L. Cottrill, V. B. Koman, P. Liu, D. Kozawa, X. Gong and M. S. Strano, Observation of the Marcus Inverted Region of Electron Transfer from Asymmetric Chemical Doping of Pristine (N,M) Single-Walled Carbon Nanotubes, *J. Am. Chem. Soc.,* 2017, **139**, 15328-15336.
46. R. Ihly, K. S. Mistry, A. J. Ferguson, T. T. Clikeman, B. W. Larson, O. Reid, O. V. Boltalina, S. H. Strauss, G. Rumbles and J. L. Blackburn, Tuning the Driving Force for Exciton Dissociation in Single-Walled Carbon Nanotube Heterojunctions, *Nat. Chem.,* 2016, **8**, 603.
47. L. Majidi, P. Yasaei, R. E. Warburton, S. Fuladi, J. Cavin, X. Hu, Z. Hemmat, S. B. Cho, P. Abbasi, M. Vörös, L. Cheng, B. Sayahpour, I. L. Bolotin, P. Zapol, J. Greeley, R. F. Klie, R. Mishra, F. Khalili-Araghi, L. A. Curtiss and A. Salehi-Khojin, New Class of Electrocatalysts Based on 2D Transition Metal Dichalcogenides in Ionic Liquid, *Adv. Mater.,* 2019, **31**, 1804453.
48. R. A. Marcus, Relation between Charge Transfer Absorption and Fluorescence Spectra and the Inverted Region, *J. Phys. Chem.,* 1989, **93**, 3078-3086.
49. J. Kang, S. Tongay, J. Zhou, J. Li and J. Wu, Band Offsets and Heterostructures of Two-Dimensional Semiconductors, *Appl. Phys. Lett.,* 2013, **102**, 012111.
50. U. Ulmer, T. Dingle, P. N. Duchesne, R. H. Morris, A. Tavasoli, T. Wood and G. A. Ozin, Fundamentals and Applications of Photocatalytic CO2 Methanation, *Nat. Commun.,* 2019, **10**, 3169.
51. J. W. Erisman, M. A. Sutton, J. Galloway, Z. Klimont and W. Winiwarter, How a Century of Ammonia Synthesis Changed the World, *Nat. Geosci.,* 2008, **1**, 636.
52. X. Xue, R. Chen, C. Yan, P. Zhao, Y. Hu, W. Zhang, S. Yang and Z. Jin, Review on Photocatalytic and Electrocatalytic Artificial Nitrogen Fixation for Ammonia Synthesis at Mild Conditions: Advances, Challenges and Perspectives, *Nano Res.,* 2019, 1-21.
53. R. V. Gorbachev, J. C. W. Song, G. L. Yu, A. V. Kretinin, F. Withers, Y. Cao, A. Mishchenko, I. V. Grigorieva, K. S. Novoselov, L. S. Levitov and A. K. Geim, Detecting Topological Currents in Graphene Superlattices, *Science,* 2014, **346**, 448.
54. D. Xiao, W. Yao and Q. Niu, Valley-Contrasting Physics in Graphene: Magnetic Moment and Topological Transport, *Phys. Rev. Lett.,* 2007, **99**, 236809.
55. Y. Shimazaki, M. Yamamoto, I. V. Borzenets, K. Watanabe, T. Taniguchi and S. Tarucha, Generation and Detection of Pure Valley Current By electrically Induced Berry Curvature in Bilayer graphene, *Nat. Phys.,* 2015, **11**, 1032.
56. Y. Jiang, T. Low, K. Chang, M. I. Katsnelson and F. Guinea, Generation of Pure Bulk Valley Current in Graphene, *Phys. Rev. Lett.,* 2013, **110**, 046601.
57. W. Yao, D. Xiao and Q. Niu, Valley-Dependent Optoelectronics from Inversion Symmetry Breaking, *Phys. Rev. B,* 2008, **77**, 235406.
58. J. Kang, L. Zhang and S.-H. Wei, A Unified Understanding of the Thickness-Dependent Bandgap Transition in Hexagonal Two-Dimensional Semiconductors, *J. Phys. Chem. Lett.,* 2016, **7**, 597-602.
59. I. Kylänpää and H.-P. Komsa, Binding Energies of Exciton Complexes in Transition Metal Dichalcogenide Monolayers and Effect of Dielectric Environment, *Phys. Rev. B,* 2015, **92**, 205418.

60. Y. Lin, X. Ling, L. Yu, S. Huang, A. L. Hsu, Y.-H. Lee, J. Kong, M. S. Dresselhaus and T. Palacios, Dielectric Screening of Excitons and Trions in Single-Layer MoS2, *Nano Lett.,* 2014, **14**, 5569-5576.
61. T. Li and G. Galli, Electronic Properties of MoS2 Nanoparticles, *J. Phys. Chem. C,* 2007, **111**, 16192-16196.
62. A. Splendiani, L. Sun, Y. Zhang, T. Li, J. Kim, C.-Y. Chim, G. Galli and F. Wang, Emerging Photoluminescence in Monolayer MoS2, *Nano Lett.,* 2010, **10**, 1271-1275.
63. C. Gong, H. Zhang, W. Wang, L. Colombo, R. M. Wallace and K. Cho, Band Alignment of Two-Dimensional Transition Metal Dichalcogenides: Application in Tunnel Field Effect Transistors, *Appl. Phys. Lett.,* 2013, **103**, 053513.
64. L.-S. Lu, G.-H. Chen, H.-Y. Cheng, C.-P. Chuu, K.-C. Lu, C.-H. Chen, M.-Y. Lu, T.-H. Chuang, D.-H. Wei, W.-C. Chueh, W.-B. Jian, M.-Y. Li, Y.-M. Chang, L.-J. Li and W.-H. Chang, Layer-Dependent and in-Plane Anisotropic Properties of Low-Temperature Synthesized Few-Layer PdSe2 Single Crystals, *ACS Nano,* 2020, **14**, 4963-4972.
65. R. A. B. Villaos, C. P. Crisostomo, Z.-Q. Huang, S.-M. Huang, A. A. B. Padama, M. A. Albao, H. Lin and F.-C. Chuang, Thickness Dependent Electronic Properties of Pt Dichalcogenides, *npj 2D Mater. Appl.,* 2019, **3**, 2.
66. M. Goryca, J. Li, A. V. Stier, T. Taniguchi, K. Watanabe, E. Courtade, S. Shree, C. Robert, B. Urbaszek, X. Marie and S. A. Crooker, Revealing Exciton Masses and Dielectric Properties of Monolayer Semiconductors with High Magnetic Fields, *Nat. Commun.,* 2019, **10**, 4172.
67. A. V. Stier, K. M. McCreary, B. T. Jonker, J. Kono and S. A. Crooker, Exciton Diamagnetic Shifts and Valley Zeeman Effects in Monolayer WS2 and MoS2 to 65 Tesla, *Nat. Commun.,* 2016, **7**, 10643.
68. A. Chernikov, T. C. Berkelbach, H. M. Hill, A. Rigosi, Y. Li, O. B. Aslan, D. R. Reichman, M. S. Hybertsen and T. F. Heinz, Exciton Binding Energy and Nonhydrogenic Rydberg Series in Monolayer WS2, *Phys. Rev. Lett.,* 2014, **113**, 076802.
69. Z. Ye, T. Cao, K. O'Brien, H. Zhu, X. Yin, Y. Wang, S. G. Louie and X. Zhang, Probing Excitonic Dark States in Single-Layer Tungsten Disulphide, *Nature,* 2014, **513**, 214-218.
70. A. V. Stier, N. P. Wilson, G. Clark, X. Xu and S. A. Crooker, Probing the Influence of Dielectric Environment on Excitons in Monolayer WSe2: Insight from High Magnetic Fields, *Nano Lett.,* 2016, **16**, 7054-7060.
71. K. He, N. Kumar, L. Zhao, Z. Wang, K. F. Mak, H. Zhao and J. Shan, Tightly Bound Excitons in Monolayer WSe2, *Phys. Rev. Lett.,* 2014, **113**, 026803.
72. M. M. Ugeda, A. J. Bradley, S.-F. Shi, F. H. da Jornada, Y. Zhang, D. Y. Qiu, W. Ruan, S.-K. Mo, Z. Hussain, Z.-X. Shen, F. Wang, S. G. Louie and M. F. Crommie, Giant Bandgap Renormalization and Excitonic Effects in a Monolayer Transition Metal Dichalcogenide Semiconductor, *Nat. Mater.,* 2014, **13**, 1091-1095.
73. M. Z. Bellus, F. Ceballos, H.-Y. Chiu and H. Zhao, Tightly Bound Trions in Transition Metal Dichalcogenide Heterostructures, *ACS Nano,* 2015, **9**, 6459-6464.
74. K. F. Mak, K. He, C. Lee, G. H. Lee, J. Hone, T. F. Heinz and J. Shan, Tightly Bound Trions in Monolayer MoS2, *Nat. Mater.,* 2013, **12**, 207-211.
75. J. S. Ross, S. Wu, H. Yu, N. J. Ghimire, A. M. Jones, G. Aivazian, J. Yan, D. G. Mandrus, D. Xiao, W. Yao and X. Xu, Electrical Control of Neutral and Charged Excitons in a Monolayer Semiconductor, *Nat. Commun.,* 2013, **4**, 1474.

76. A. M. Jones, H. Yu, N. J. Ghimire, S. Wu, G. Aivazian, J. S. Ross, B. Zhao, J. Yan, D. G. Mandrus, D. Xiao, W. Yao and X. Xu, Optical Generation of Excitonic Valley Coherence in Monolayer WSe2, *Nat. Nanotechnol.,* 2013, **8**, 634-638.
77. M. Drüppel, T. Deilmann, P. Krüger and M. Rohlfing, Diversity of Trion States and Substrate Effects in the Optical Properties of an MoS2 Monolayer, *Nat. Commun.,* 2017, **8**, 2117.
78. M. Barbone, A. R. P. Montblanch, D. M. Kara, C. Palacios-Berraquero, A. R. Cadore, D. De Fazio, B. Pingault, E. Mostaani, H. Li, B. Chen, K. Watanabe, T. Taniguchi, S. Tongay, G. Wang, A. C. Ferrari and M. Atatüre, Charge-Tuneable Biexciton Complexes in Monolayer WSe2, *Nat. Commun.,* 2018, **9**, 3721.
79. T. Zhu, L. Yuan, Y. Zhao, M. Zhou, Y. Wan, J. Mei and L. Huang, Highly Mobile Charge-Transfer Excitons in Two-Dimensional WS2/Tetracene Heterostructures, *Sci. Adv.,* 2018, **4**, eaao3104.
80. T. R. Kafle, B. Kattel, S. D. Lane, T. Wang, H. Zhao and W.-L. Chan, Charge Transfer Exciton and Spin Flipping at Organic–Transition-Metal Dichalcogenide Interfaces, *ACS Nano,* 2017, **11**, 10184-10192.
81. T. R. Kafle, B. Kattel, P. Yao, P. Zereshki, H. Zhao and W.-L. Chan, Effect of the Interfacial Energy Landscape on Photoinduced Charge Generation at the ZnPc/MoS2 Interface, *J. Am. Chem. Soc.,* 2019, **141**, 11328-11336.
82. M.-C. Heissenbüttel, P. Marauhn, T. Deilmann, P. Krüger and M. Rohlfing, Nature of the Excited States of Layered Systems and Molecular Excimers: Exciplex States and Their Dependence on Structure, *Phys. Rev. B,* 2019, **99**, 035425.
83. H. Fang, C. Battaglia, C. Carraro, S. Nemsak, B. Ozdol, J. S. Kang, H. A. Bechtel, S. B. Desai, F. Kronast, A. A. Unal, G. Conti, C. Conlon, G. K. Palsson, M. C. Martin, A. M. Minor, C. S. Fadley, E. Yablonovitch, R. Maboudian and A. Javey, Strong Interlayer Coupling in Van der Waals Heterostructures Built from Single-Layer Chalcogenides, *Proc. Natl. Acad. Sci.,* 2014, **111**, 6198.
84. B. Miller, A. Steinhoff, B. Pano, J. Klein, F. Jahnke, A. Holleitner and U. Wurstbauer, Long-Lived Direct and Indirect Interlayer Excitons in Van der Waals Heterostructures, *Nano Lett.,* 2017, **17**, 5229-5237.
85. P. Rivera, J. R. Schaibley, A. M. Jones, J. S. Ross, S. Wu, G. Aivazian, P. Klement, K. Seyler, G. Clark, N. J. Ghimire, J. Yan, D. G. Mandrus, W. Yao and X. Xu, Observation of Long-Lived Interlayer Excitons in Monolayer MoSe2–WSe2 Heterostructures, *Nat. Commun.,* 2015, **6**, 6242.
86. E. V. Calman, M. M. Fogler, L. V. Butov, S. Hu, A. Mishchenko and A. K. Geim, Indirect Excitons in Van der Waals Heterostructures at Room Temperature, *Nat. Commun.,* 2018, **9**, 1895.
87. T. Deilmann and K. S. Thygesen, Interlayer Trions in the MoS2/WS2 Van der Waals Heterostructure, *Nano Lett.,* 2018, **18**, 1460-1465.
88. E. V. Calman, L. H. Fowler-Gerace, D. J. Choksy, L. V. Butov, D. E. Nikonov, I. A. Young, S. Hu, A. Mishchenko and A. K. Geim, Indirect Excitons and Trions in MoSe2/WSe2 Van der Waals Heterostructures, *Nano Lett.,* 2020, **20**, 1869-1875.
89. J. R. Schaibley, H. Yu, G. Clark, P. Rivera, J. S. Ross, K. L. Seyler, W. Yao and X. Xu, Valleytronics in 2D Materials, *Nat. Rev. Mater.,* 2016, **1**, 16055.
90. D. Xiao, G.-B. Liu, W. Feng, X. Xu and W. Yao, Coupled Spin and Valley Physics in Monolayers of MoS2 and Other Group-VI Dichalcogenides, *Phys. Rev. Lett.,* 2012, **108**, 196802.

91. M. Koperski, R. Molas Maciej, A. Arora, K. Nogajewski, O. Slobodeniuk Artur, C. Faugeras and M. Potemski, Optical Properties of Atomically Thin Transition Metal Dichalcogenides: Observations and Puzzles, *Nanophotonics,* 2017, **6**, 1289.
92. X. Xu, W. Yao, D. Xiao and T. F. Heinz, Spin and Pseudospins in Layered Transition Metal Dichalcogenides, *Nat. Phys.,* 2014, **10**, 343.
93. A. Kormányos, G. Burkard, M. Gmitra, J. Fabian, V. Zólyomi, N. D. Drummond and V. Fal'ko, K · P Theory for Two-Dimensional Transition Metal Dichalcogenide Semiconductors, *2D Mater.,* 2015, **2**, 022001.
94. J. M. Riley, F. Mazzola, M. Dendzik, M. Michiardi, T. Takayama, L. Bawden, C. Granerød, M. Leandersson, T. Balasubramanian, M. Hoesch, T. K. Kim, H. Takagi, W. Meevasana, P. Hofmann, M. S. Bahramy, J. W. Wells and P. D. C. King, Direct Observation of Spin-Polarized Bulk Bands in an Inversion-Symmetric Semiconductor, *Nat. Phys.,* 2014, **10**, 835-839.
95. Y. Zhang, T.-R. Chang, B. Zhou, Y.-T. Cui, H. Yan, Z. Liu, F. Schmitt, J. Lee, R. Moore, Y. Chen, H. Lin, H.-T. Jeng, S.-K. Mo, Z. Hussain, A. Bansil and Z.-X. Shen, Direct Observation of the Transition from Indirect to Direct Bandgap in Atomically Thin Epitaxial MoSe2, *Nat. Nanotechnol.,* 2014, **9**, 111-115.
96. G.-B. Liu, W.-Y. Shan, Y. Yao, W. Yao and D. Xiao, Three-Band Tight-Binding Model for Monolayers of Group-VIB Transition Metal Dichalcogenides, *Phys. Rev. B,* 2013, **88**, 085433.
97. J. A. Reyes-Retana and F. Cervantes-Sodi, Spin-Orbital Effects in Metal-Dichalcogenide Semiconducting Monolayers, *Sci. Rep.,* 2016, **6**, 24093.
98. Z. Y. Zhu, Y. C. Cheng and U. Schwingenschlögl, Giant Spin-Orbit-Induced Spin Splitting in Two-Dimensional Transition-Metal Dichalcogenide Semiconductors, *Phys. Rev. B,* 2011, **84**, 153402.
99. K. Kośmider, J. W. González and J. Fernández-Rossier, Large Spin Splitting in the Conduction Band of Transition Metal Dichalcogenide Monolayers, *Phys. Rev. B,* 2013, **88**, 245436.
100. J. A. Miwa, S. Ulstrup, S. G. Sørensen, M. Dendzik, A. G. Čabo, M. Bianchi, J. V. Lauritsen and P. Hofmann, Electronic Structure of Epitaxial Single-Layer MoS2, *Phys. Rev. Lett.,* 2015, **114**, 046802.
101. L. Sun, J. Yan, D. Zhan, L. Liu, H. Hu, H. Li, B. K. Tay, J.-L. Kuo, C.-C. Huang, D. W. Hewak, P. S. Lee and Z. X. Shen, Spin-Orbit Splitting in Single-Layer MoS2 Revealed by Triply Resonant Raman Scattering, *Phys. Rev. Lett.,* 2013, **111**, 126801.
102. X. Fan, D. J. Singh and W. Zheng, Valence Band Splitting on Multilayer MoS2: Mixing of Spin–Orbit Coupling and Interlayer Coupling, *J. Phys. Chem. Lett.,* 2016, **7**, 2175-2181.
103. Q. Wang, J. Li, J. Besbas, C.-H. Hsu, K. Cai, L. Yang, S. Cheng, Y. Wu, W. Zhang, K. Wang, T.-R. Chang, H. Lin, H. Chang and H. Yang, Room-Temperature Nanoseconds Spin Relaxation in WTe2 and MoTe2 Thin Films, *Adv. Sci.,* 2018, **5**, 1700912.
104. K. Marinov, A. Avsar, K. Watanabe, T. Taniguchi and A. Kis, Resolving the Spin Splitting in the Conduction Band of Monolayer MoS2, *Nat. Commun.,* 2017, **8**, 1938.
105. H. Yuan, Z. Liu, G. Xu, B. Zhou, S. Wu, D. Dumcenco, K. Yan, Y. Zhang, S.-K. Mo, P. Dudin, V. Kandyba, M. Yablonskikh, A. Barinov, Z. Shen, S. Zhang, Y. Huang, X. Xu, Z. Hussain, H. Y. Hwang, Y. Cui and Y. Chen, Evolution of the Valley Position in Bulk Transition-Metal Chalcogenides and Their Monolayer Limit, *Nano Lett.,* 2016, **16**, 4738-4745.

106. X.-X. Zhang, T. Cao, Z. Lu, Y.-C. Lin, F. Zhang, Y. Wang, Z. Li, J. C. Hone, J. A. Robinson, D. Smirnov, S. G. Louie and T. F. Heinz, Magnetic Brightening and Control of Dark Excitons in Monolayer WSe2, *Nat. Nanotechnol.,* 2017, **12**, 883.
107. Z. Ye, D. Sun and T. F. Heinz, Optical Manipulation of Valley Pseudospin, *Nat. Phys.,* 2016, **13**, 26.
108. J. R. Schaibley, P. Rivera, H. Yu, K. L. Seyler, J. Yan, D. G. Mandrus, T. Taniguchi, K. Watanabe, W. Yao and X. Xu, Directional Interlayer Spin-Valley Transfer in Two-Dimensional Heterostructures, *Nat. Commun.,* 2016, **7**, 13747.
109. P. Rivera, K. L. Seyler, H. Yu, J. R. Schaibley, J. Yan, D. G. Mandrus, W. Yao and X. Xu, Valley-Polarized Exciton Dynamics in a 2D Semiconductor Heterostructure, *Science,* 2016, **351**, 688.
110. C. Jiang, W. Xu, A. Rasmita, Z. Huang, K. Li, Q. Xiong and W.-b. Gao, Microsecond Dark-Exciton Valley Polarization Memory in Two-Dimensional Heterostructures, *Nat. Commun.,* 2018, **9**, 753.
111. K. Hao, G. Moody, F. Wu, C. K. Dass, L. Xu, C.-H. Chen, L. Sun, M.-Y. Li, L.-J. Li, A. H. MacDonald and X. Li, Direct Measurement of Exciton Valley Coherence in Monolayer WSe2, *Nat. Phys.,* 2016, **12**, 677.
112. T. Jakubczyk, V. Delmonte, M. Koperski, K. Nogajewski, C. Faugeras, W. Langbein, M. Potemski and J. Kasprzak, Radiatively Limited Dephasing and Exciton Dynamics in MoSe2 Monolayers Revealed with Four-Wave Mixing Microscopy, *Nano Lett.,* 2016, **16**, 5333-5339.
113. Q. Wang, S. Ge, X. Li, J. Qiu, Y. Ji, J. Feng and D. Sun, Valley Carrier Dynamics in Monolayer Molybdenum Disulfide from Helicity-Resolved Ultrafast Pump–Probe Spectroscopy, *ACS Nano,* 2013, **7**, 11087-11093.
114. R. Schmidt, G. Berghäuser, R. Schneider, M. Selig, P. Tonndorf, E. Malić, A. Knorr, S. Michaelis de Vasconcellos and R. Bratschitsch, Ultrafast Coulomb-Induced Intervalley Coupling in Atomically Thin WS2, *Nano Lett.,* 2016, **16**, 2945-2950.
115. C. Mai, A. Barrette, Y. Yu, Y. G. Semenov, K. W. Kim, L. Cao and K. Gundogdu, Many-Body Effects in Valleytronics: Direct Measurement of Valley Lifetimes in Single-Layer MoS2, *Nano Lett.,* 2014, **14**, 202-206.
116. C. Ataca, H. Şahin and S. Ciraci, Stable, Single-Layer MX2 Transition-Metal Oxides and Dichalcogenides in a Honeycomb-Like Structure, *J. Phys. Chem. C,* 2012, **116**, 8983-8999.
117. H. Y. Hwang and S.-W. Cheong, Enhanced Intergrain Tunneling Magnetoresistance in Half-Metallic CrO2 Films, *Science,* 1997, **278**, 1607-1609.
118. E. E. Benson, H. Zhang, S. A. Schuman, S. U. Nanayakkara, N. D. Bronstein, S. Ferrere, J. L. Blackburn and E. M. Miller, Balancing the Hydrogen Evolution Reaction, Surface Energetics, and Stability of Metallic MoS_2 Nanosheets via Covalent Functionalization, *J. Am. Chem. Soc.,* 2018, **140**, 441-450.
119. H. Pan and Y.-W. Zhang, Tuning the Electronic and Magnetic Properties of MoS2 Nanoribbons by Strain Engineering, *J. Phys. Chem. C,* 2012, **116**, 11752-11757.
120. K.-L. Tai, G.-M. Huang, C.-W. Huang, T.-C. Tsai, S.-K. Lee, T.-Y. Lin, Y.-C. Lo and W.-W. Wu, Observing Phase Transformation in CVD-Grown MoS2 via Atomic Resolution Tem, *Chem. Commun.,* 2018, **54**, 9941-9944.
121. Y. H. V. D. F. T. Eda G and M. C. Chen, *Nano Lett.,* 2011, **11**, 5111.

122. A. Castellanos-Gomez, R. Roldán, E. Cappelluti, M. Buscema, F. Guinea, H. S. J. van der Zant and G. A. Steele, Local Strain Engineering in Atomically Thin MoS_2, *Nano Lett.,* 2013, **13**, 5361-5366.
123. K. C. Knirsch, N. C. Berner, H. C. Nerl, C. S. Cucinotta, Z. Gholamvand, N. McEvoy, Z. Wang, I. Abramovic, P. Vecera and M. Halik, Basal-Plane Functionalization of Chemically Exfoliated Molybdenum Disulfide by Diazonium Salts, *ACS nano,* 2015, **9**, 6018-6030.
124. Q. Liu, Q. Fang, W. Chu, Y. Wan, X. Li, W. Xu, M. Habib, S. Tao, Y. Zhou, D. Liu, T. Xiang, A. Khalil, X. Wu, M. Chhowalla, P. M. Ajayan and L. Song, Electron-Doped 1T-MoS_2 via Interface Engineering for Enhanced Electrocatalytic Hydrogen Evolution, *Chem. Mater.,* 2017, **29**, 4738-4744.
125. D. Voiry, A. Mohite and M. Chhowalla, Phase Engineering of Transition Metal Dichalcogenides, *Chem. Soc. Rev.,* 2015, **44**, 2702-2712.
126. Y. Yu, G.-H. Nam, Q. He, X.-J. Wu, K. Zhang, Z. Yang, J. Chen, Q. Ma, M. Zhao, Z. Liu, F.-R. Ran, X. Wang, H. Li, X. Huang, B. Li, Q. Xiong, Q. Zhang, Z. Liu, L. Gu, Y. Du, W. Huang and H. Zhang, High Phase-Purity 1T'-MoS2- and 1T'-MoSe2-Layered Crystals, *Nat. Chem.,* 2018, **10**, 638-643.
127. F. Zheng, C. Cai, S. Ge, X. Zhang, X. Liu, H. Lu, Y. Zhang, J. Qiu, T. Taniguchi, K. Watanabe, S. Jia, J. Qi, J.-H. Chen, D. Sun and J. Feng, On the Quantum Spin Hall Gap of Monolayer 1T'-WTe2, *Adv. Mater.,* 2016, **28**, 4845-4851.
128. L. Zhuojun, S. Yekai and T. Shujie, Quantum Spin Hall State in Monolayer 1T'-Tmdcs, *J. Phys. Condens. Matter,* 2020.
129. R. Peng, L. Liang, Z. D. Hood, A. Boulesbaa, A. Puretzky, A. V. Ievlev, J. Come, O. S. Ovchinnikova, H. Wang, C. Ma, M. Chi, B. G. Sumpter and Z. Wu, In-Plane Heterojunctions Enable Multiphasic Two-Dimensional (2D) MoS_2 Nanosheets as Efficient Photocatalysts for Hydrogen Evolution from Water Reduction, *ACS Catal.,* 2016, **6**, 6723-6729.
130. S. Deng, A. V. Sumant and V. Berry, Strain Engineering in Two-Dimensional Nanomaterials Beyond Graphene, *Nano Today,* 2018, **22**, 14-35.
131. G. M. Carroll, H. Zhang, J. R. Dunklin, E. M. Miller, N. R. Neale and J. van de Lagemaat, Unique Interfacial Thermodynamics of Few-Layer 2D MoS2 for (Photo)Electrochemical Catalysis, *Energy Environ. Sci.,* 2019, **12**, 1648-1656.
132. Y. Tan, P. Liu, L. Chen, W. Cong, Y. Ito, J. Han, X. Guo, Z. Tang, T. Fujita, A. Hirata and M. W. Chen, Monolayer MoS2 Films Supported by 3D Nanoporous Metals for High-Efficiency Electrocatalytic Hydrogen Production, *Adv. Mater.,* 2014, **26**, 8023-8028.
133. H. Li, Y. Li, A. Aljarb, Y. Shi and L.-J. Li, Epitaxial Growth of Two-Dimensional Layered Transition-Metal Dichalcogenides: Growth Mechanism, Controllability, and Scalability, *Chem. Rev.,* 2018, **118**, 6134-6150.
134. S. L. Wong, H. Liu and D. Chi, Recent Progress in Chemical Vapor Deposition Growth of Two-Dimensional Transition Metal Dichalcogenides, *Prog. Cryst. Growth Charact. Mater.,* 2016, **62**, 9-28.
135. Z. Cai, B. Liu, X. Zou and H.-M. Cheng, Chemical Vapor Deposition Growth and Applications of Two-Dimensional Materials and Their Heterostructures, *Chem. Rev.,* 2018, **118**, 6091-6133.

136. R. Cheng, D. Li, H. Zhou, C. Wang, A. Yin, S. Jiang, Y. Liu, Y. Chen, Y. Huang and X. Duan, Electroluminescence and Photocurrent Generation from Atomically Sharp WSe2/MoS2 Heterojunction P–N Diodes, *Nano Lett.,* 2014, **14**, 5590-5597.
137. G. H. Han, D. L. Duong, D. H. Keum, S. J. Yun and Y. H. Lee, Van der Waals Metallic Transition Metal Dichalcogenides, *Chem. Rev.,* 2018, **118**, 6297-6336.
138. J. H. Han, M. Kwak, Y. Kim and J. Cheon, Recent Advances in the Solution-Based Preparation of Two-Dimensional Layered Transition Metal Chalcogenide Nanostructures, *Chem. Rev.,* 2018, **118**, 6151-6188.
139. C. Huo, Z. Yan, X. Song and H. Zeng, 2D Materials via Liquid Exfoliation: A Review on Fabrication and Applications, *Sci. Bull.,* 2015, **60**, 1994-2008.
140. A. L. Elías, N. Perea-López, A. Castro-Beltrán, A. Berkdemir, R. Lv, S. Feng, A. D. Long, T. Hayashi, Y. A. Kim, M. Endo, H. R. Gutiérrez, N. R. Pradhan, L. Balicas, T. E. Mallouk, F. López-Urías, H. Terrones and M. Terrones, Controlled Synthesis and Transfer of Large-Area WS2 Sheets: From Single Layer to Few Layers, *ACS Nano,* 2013, **7**, 5235-5242.
141. J. Jeon, S. K. Jang, S. M. Jeon, G. Yoo, Y. H. Jang, J.-H. Park and S. Lee, Layer-Controlled CVD Growth of Large-Area Two-Dimensional MoS2 Films, *Nanoscale,* 2015, **7**, 1688-1695.
142. S. Deb, P. Chakrabarti, P. K. Mohapatra, B. K. Barick and S. Dhar, Tailoring of Defect Luminescence in CVD Grown Monolayer MoS2 Film, *Appl. Surf. Sci.,* 2018, **445**, 542-547.
143. S. Sasaki, Y. Kobayashi, Z. Liu, K. Suenaga, Y. Maniwa, Y. Miyauchi and Y. Miyata, Growth and Optical Properties of Nb-Doped WS2 Monolayers, *Appl. Phys. Express,* 2016, **9**, 071201.
144. S. R. Kadam, D. J. Late, R. P. Panmand, M. V. Kulkarni, L. K. Nikam, S. W. Gosavi, C. J. Park and B. B. Kale, Nanostructured 2D MoS2 Honeycomb and Hierarchical 3D CdMoS4 Marigold Nanoflowers for Hydrogen Production under Solar Light, *J. Mater. Chem. A,* 2015, **3**, 21233-21243.
145. I. Paradisanos, S. Germanis, N. T. Pelekanos, C. Fotakis, E. Kymakis, G. Kioseoglou and E. Stratakis, Room Temperature Observation of Biexcitons in Exfoliated WS2 Monolayers, *Appl. Phys. Lett.,* 2017, **110**, 193102.
146. H. Li, J. Wu, Z. Yin and H. Zhang, Preparation and Applications of Mechanically Exfoliated Single-Layer and Multilayer MoS2 and WSe2 Nanosheets, *Acc. Chem. Res.,* 2014, **47**, 1067-1075.
147. J. N. Coleman, M. Lotya, A. O'Neill, S. D. Bergin, P. J. King, U. Khan, K. Young, A. Gaucher, S. De, R. J. Smith, I. V. Shvets, S. K. Arora, G. Stanton, H.-Y. Kim, K. Lee, G. T. Kim, G. S. Duesberg, T. Hallam, J. J. Boland, J. J. Wang, J. F. Donegan, J. C. Grunlan, G. Moriarty, A. Shmeliov, R. J. Nicholls, J. M. Perkins, E. M. Grieveson, K. Theuwissen, D. W. McComb, P. D. Nellist and V. Nicolosi, Two-Dimensional Nanosheets Produced by Liquid Exfoliation of Layered Materials, *Science,* 2011, **331**, 568-571.
148. P. May, U. Khan, J. M. Hughes and J. N. Coleman, Role of Solubility Parameters in Understanding the Steric Stabilization of Exfoliated Two-Dimensional Nanosheets by Adsorbed Polymers, *J. Phys. Chem. C,* 2012, **116**, 11393-11400.
149. R. J. Smith, P. J. King, M. Lotya, C. Wirtz, U. Khan, S. De, A. O'Neill, G. S. Duesberg, J. C. Grunlan, G. Moriarty, J. Chen, J. Wang, A. I. Minett, V. Nicolosi and J. N. Coleman, Large-Scale Exfoliation of Inorganic Layered Compounds in Aqueous Surfactant Solutions, *Adv. Mater.,* 2011, **23**, 3944-3948.

150. E. Varrla, C. Backes, K. R. Paton, A. Harvey, Z. Gholamvand, J. McCauley and J. N. Coleman, Large-Scale Production of Size-Controlled MoS2 Nanosheets by Shear Exfoliation, *Chem. Mater.,* 2015, **27**, 1129-1139.
151. E. M. Alexeev, D. A. Ruiz-Tijerina, M. Danovich, M. J. Hamer, D. J. Terry, P. K. Nayak, S. Ahn, S. Pak, J. Lee, J. I. Sohn, M. R. Molas, M. Koperski, K. Watanabe, T. Taniguchi, K. S. Novoselov, R. V. Gorbachev, H. S. Shin, V. I. Fal'ko and A. I. Tartakovskii, Resonantly Hybridized Excitons in Moiré Superlattices in Van der Waals Heterostructures, *Nature,* 2019, **567**, 81-86.
152. K. C. Knirsch, N. C. Berner, H. C. Nerl, C. S. Cucinotta, Z. Gholamvand, N. McEvoy, Z. Wang, I. Abramovic, P. Vecera, M. Halik, S. Sanvito, G. S. Duesberg, V. Nicolosi, F. Hauke, A. Hirsch, J. N. Coleman and C. Backes, Basal-Plane Functionalization of Chemically Exfoliated Molybdenum Disulfide by Diazonium Salts, *ACS Nano,* 2015, **9**, 6018-6030.
153. Z. Zeng, Z. Yin, X. Huang, H. Li, Q. He, G. Lu, F. Boey and H. Zhang, Single-Layer Semiconducting Nanosheets: High-Yield Preparation and Device Fabrication, *Angew. Chem. Int. Ed.,* 2011, **50**, 11093-11097.
154. R. Ionescu, I. Ruiz, Z. Favors, B. Campbell, M. R. Neupane, D. Wickramaratne, K. Ahmed, C. Liu, N. Abrahamian, R. K. Lake, M. Ozkan and C. S. Ozkan, Two Step Growth Phenomena of Molybdenum Disulfide–Tungsten Disulfide Heterostructures, *Chem. Commun.,* 2015, **51**, 11213-11216.
155. G. V. Bianco, M. Losurdo, M. M. Giangregorio, A. Sacchetti, P. Prete, N. Lovergine, P. Capezzuto and G. Bruno, Direct Epitaxial CVD Synthesis of Tungsten Disulfide on Epitaxial and CVD Graphene, *RSC Adv.,* 2015, **5**, 98700-98708.
156. S. Wang, X. Wang and J. H. Warner, All Chemical Vapor Deposition Growth of MoS2:h-BN Vertical Van der Waals Heterostructures, *ACS Nano,* 2015, **9**, 5246-5254.
157. C. Liu, B. Chai, C. Wang, J. Yan and Z. Ren, Solvothermal Fabrication of MoS2 Anchored on ZnIn2S4 Microspheres with Boosted Photocatalytic Hydrogen Evolution Activity, *Int. J. Hydrogen Energy,* 2018, **43**, 6977-6986.
158. X. Zhang, S. Zhang, B. Chen, H. Wang, K. Wu, Y. Chen, J. Fan, S. Qi, X. Cui, L. Zhang and J. Wang, Direct Synthesis of Large-Scale Hierarchical MoS2 Films Nanostructured with Orthogonally Oriented Vertically and Horizontally Aligned Layers, *Nanoscale,* 2016, **8**, 431-439.
159. A. Gurarslan, Y. Yu, L. Su, Y. Yu, F. Suarez, S. Yao, Y. Zhu, M. Ozturk, Y. Zhang and L. Cao, Surface-Energy-Assisted Perfect Transfer of Centimeter-Scale Monolayer and Few-Layer MoS2 Films onto Arbitrary Substrates, *ACS Nano,* 2014, **8**, 11522-11528.
160. G. Tang, Y. Chen, J. Yin, S. Shen and K. Cai, Preparation, Characterization and Properties of MoS2 Nanosheets via a Microwave-Assisted Wet-Chemical Route, *Ceram. Int.,* 2018, **44**, 5336-5340.
161. M. Piao, C. Li, M.-K. Joo, J. Chu, X. Wang, Y. Chi, H. Zhang and H. Shi, Hydrothermal Synthesis of Stable 1T-WS2 and Single-Walled Carbon Nanotube Hybrid Flexible Thin Films with Enhanced Thermoelectric Performance, *Energy Technol.,* 2018, **6**, 1921-1928.
162. R. Dong, T. Zhang and X. Feng, Interface-Assisted Synthesis of 2D Materials: Trend and Challenges, *Chem. Rev.,* 2018, **118**, 6189-6235.
163. D. B. Sulas-Kern, H. Zhang, Z. Li and J. L. Blackburn, Microsecond Charge Separation at Heterojunctions between Transition Metal Dichalcogenide Monolayers and Single-Walled Carbon Nanotubes, *Mater. Horiz.,* 2019, **6**, 2103-2111.

164. C. Zhang, C. Gong, Y. Nie, K.-A. Min, C. Liang, Y. J. Oh, H. Zhang, W. Wang, S. Hong, L. Colombo, R. M. Wallace and K. Cho, Systematic Study of Electronic Structure and Band Alignment of Monolayer Transition Metal Dichalcogenides in Van der Waals Heterostructures, *2D Mater.,* 2016, **4**, 015026.
165. M.-H. Chiu, C. Zhang, H.-W. Shiu, C.-P. Chuu, C.-H. Chen, C.-Y. S. Chang, C.-H. Chen, M.-Y. Chou, C.-K. Shih and L.-J. Li, Determination of Band Alignment in the Single-Layer MoS2/WSe2 Heterojunction, *Nat. Commun.,* 2015, **6**, 7666.
166. H. M. Hill, A. F. Rigosi, K. T. Rim, G. W. Flynn and T. F. Heinz, Band Alignment in MoS2/WS2 Transition Metal Dichalcogenide Heterostructures Probed by Scanning Tunneling Microscopy and Spectroscopy, *Nano Lett.,* 2016, **16**, 4831-4837.
167. N. R. Wilson, P. V. Nguyen, K. Seyler, P. Rivera, A. J. Marsden, Z. P. L. Laker, G. C. Constantinescu, V. Kandyba, A. Barinov, N. D. M. Hine, X. Xu and D. H. Cobden, Determination of Band Offsets, Hybridization, and Exciton Binding in 2D Semiconductor Heterostructures, *Sci. Adv.,* 2017, **3**, e1601832.
168. C.-H. Lee, G.-H. Lee, A. M. van der Zande, W. Chen, Y. Li, M. Han, X. Cui, G. Arefe, C. Nuckolls, T. F. Heinz, J. Guo, J. Hone and P. Kim, Atomically Thin P–N Junctions with Van der Waals Heterointerfaces, *Nat. Nanotechnol.,* 2014, **9**, 676-681.
169. X. Hong, J. Kim, S.-F. Shi, Y. Zhang, C. Jin, Y. Sun, S. Tongay, J. Wu, Y. Zhang and F. Wang, Ultrafast Charge Transfer in Atomically Thin MoS2/WS2 Heterostructures, *Nat. Nanotechnol.,* 2014, **9**, 682.
170. A. F. Rigosi, H. M. Hill, Y. Li, A. Chernikov and T. F. Heinz, Probing Interlayer Interactions in Transition Metal Dichalcogenide Heterostructures by Optical Spectroscopy: MoS2/WS2 and MoSe2/WSe2, *Nano Lett.,* 2015, **15**, 5033-5038.
171. F. Ceballos, M. Z. Bellus, H.-Y. Chiu and H. Zhao, Ultrafast Charge Separation and Indirect Exciton Formation in a MoS2–MoSe2 Van der Waals Heterostructure, *ACS Nano,* 2014, **8**, 12717-12724.
172. M. S. Kim, C. Seo, H. Kim, J. Lee, D. H. Luong, J.-H. Park, G. H. Han and J. Kim, Simultaneous Hosting of Positive and Negative Trions and the Enhanced Direct Band Emission in MoSe2/MoS2 Heterostacked Multilayers, *ACS Nano,* 2016, **10**, 6211-6219.
173. R. Long and O. V. Prezhdo, Quantum Coherence Facilitates Efficient Charge Separation at a MoS2/MoSe2 Van der Waals Junction, *Nano Lett.,* 2016, **16**, 1996-2003.
174. H. Wang, C. Zhang and F. Rana, Ultrafast Dynamics of Defect-Assisted Electron–Hole Recombination in Monolayer MoS2, *Nano Lett.,* 2015, **15**, 339-345.
175. H. Shi, R. Yan, S. Bertolazzi, J. Brivio, B. Gao, A. Kis, D. Jena, H. G. Xing and L. Huang, Exciton Dynamics in Suspended Monolayer and Few-Layer MoS2 2D Crystals, *ACS Nano,* 2013, **7**, 1072-1080.
176. M. J. Shin, D. H. Kim and D. Lim, Photoluminescence Saturation and Exciton Decay Dynamics in Transition Metal Dichalcogenide Monolayers, *J. Korean Phys. Soc.,* 2014, **65**, 2077-2081.
177. H. Wang, J. Bang, Y. Sun, L. Liang, D. West, V. Meunier and S. Zhang, The Role of Collective Motion in the Ultrafast Charge Transfer in Van der Waals Heterostructures, *Nat. Commun.,* 2016, **7**, 11504.
178. V. Coropceanu, X.-K. Chen, T. Wang, Z. Zheng and J.-L. Brédas, Charge-Transfer Electronic States In organic Solar Cells, *Nat. Rev. Mater.,* 2019, **4**, 689-707.

179. J. Zhang, A. C. Jakowetz, G. Li, D. Di, S. M. Menke, A. Rao, R. H. Friend and A. A. Bakulin, On the Energetics of Bound Charge-Transfer States in Organic Photovoltaics, *J. Mater. Chem. A,* 2017, **5**, 11949-11959.
180. X. Zhu, N. R. Monahan, Z. Gong, H. Zhu, K. W. Williams and C. A. Nelson, Charge Transfer Excitons at Van der Waals Interfaces, *J. Am. Chem. Soc.,* 2015, **137**, 8313-8320.
181. S. Mouri, W. Zhang, D. Kozawa, Y. Miyauchi, G. Eda and K. Matsuda, Thermal Dissociation of Inter-Layer Excitons in MoS2/MoSe2 Hetero-Bilayers, *Nanoscale,* 2017, **9**, 6674-6679.
182. K. Vandewal, S. Albrecht, E. T. Hoke, K. R. Graham, J. Widmer, J. D. Douglas, M. Schubert, W. R. Mateker, J. T. Bloking, G. F. Burkhard, A. Sellinger, J. M. J. Fréchet, A. Amassian, M. K. Riede, M. D. McGehee, D. Neher and A. Salleo, Efficient Charge Generation by Relaxed Charge-Transfer States at Organic Interfaces, *Nat. Mater.,* 2014, **13**, 63-68.
183. Y. Puttisong, Y. Xia, X. Chen, F. Gao, I. A. Buyanova, O. Inganäs and W. M. Chen, Charge Generation via Relaxed Charge-Transfer States in Organic Photovoltaics by an Energy-Disorder-Driven Entropy Gain, *J. Phys. Chem. C,* 2018, **122**, 12640-12646.
184. F. Ceballos, M. Z. Bellus, H.-Y. Chiu and H. Zhao, Probing Charge Transfer Excitons in a MoSe2–WS2 Van der Waals Heterostructure, *Nanoscale,* 2015, **7**, 17523-17528.
185. A. Ciarrocchi, D. Unuchek, A. Avsar, K. Watanabe, T. Taniguchi and A. Kis, Polarization Switching and Electrical Control of Interlayer Excitons in Two-Dimensional Van der Waals Heterostructures, *Nat. Photonics,* 2019, **13**, 131-136.
186. T. Wang, S. Miao, Z. Li, Y. Meng, Z. Lu, Z. Lian, M. Blei, T. Taniguchi, K. Watanabe, S. Tongay, D. Smirnov and S.-F. Shi, Giant Valley-Zeeman Splitting from Spin-Singlet and Spin-Triplet Interlayer Excitons in WSe2/MoSe2 Heterostructure, *Nano Lett.,* 2019.
187. O. Karni, E. Barré, S. C. Lau, R. Gillen, E. Y. Ma, B. Kim, K. Watanabe, T. Taniguchi, J. Maultzsch, K. Barmak, R. H. Page and T. F. Heinz, Infrared Interlayer Exciton Emission in MoS2/WSe2 Heterostructures, *Phys. Rev. Lett.,* 2019, **123**, 247402.
188. J. Kunstmann, F. Mooshammer, P. Nagler, A. Chaves, F. Stein, N. Paradiso, G. Plechinger, C. Strunk, C. Schüller, G. Seifert, D. R. Reichman and T. Korn, Momentum-Space Indirect Interlayer Excitons in Transition-Metal Dichalcogenide Van der Waals Heterostructures, *Nat. Phys.,* 2018, **14**, 801-805.
189. F. Wu, T. Lovorn and A. H. MacDonald, Theory of Optical Absorption by Interlayer Excitons in Transition Metal Dichalcogenide Heterobilayers, *Phys. Rev. B,* 2018, **97**, 035306.
190. K. Tran, G. Moody, F. Wu, X. Lu, J. Choi, K. Kim, A. Rai, D. A. Sanchez, J. Quan, A. Singh, J. Embley, A. Zepeda, M. Campbell, T. Autry, T. Taniguchi, K. Watanabe, N. Lu, S. K. Banerjee, K. L. Silverman, S. Kim, E. Tutuc, L. Yang, A. H. MacDonald and X. Li, Evidence for Moiré Excitons in Van der Waals Heterostructures, *Nature,* 2019, **567**, 71-75.
191. K. L. Seyler, P. Rivera, H. Yu, N. P. Wilson, E. L. Ray, D. G. Mandrus, J. Yan, W. Yao and X. Xu, Signatures of Moiré-Trapped Valley Excitons in MoSe2/WSe2 Heterobilayers, *Nature,* 2019, **567**, 66-70.
192. Y. Yu, S. Hu, L. Su, L. Huang, Y. Liu, Z. Jin, A. A. Purezky, D. B. Geohegan, K. W. Kim, Y. Zhang and L. Cao, Equally Efficient Interlayer Exciton Relaxation and Improved Absorption in Epitaxial and Nonepitaxial MoS2/WS2 Heterostructures, *Nano Lett.,* 2015, **15**, 486-491.

193. H. Chen, X. Wen, J. Zhang, T. Wu, Y. Gong, X. Zhang, J. Yuan, C. Yi, J. Lou, P. M. Ajayan, W. Zhuang, G. Zhang and J. Zheng, Ultrafast Formation of Interlayer Hot Excitons in Atomically Thin MoS2/WS2 Heterostructures, *Nat. Commun.,* 2016, **7**, 12512.
194. J. Zhao, H. Liu, Z. Yu, R. Quhe, S. Zhou, Y. Wang, C. C. Liu, H. Zhong, N. Han, J. Lu, Y. Yao and K. Wu, Rise of Silicene: A Competitive 2D Material, *Progress in Materials Science,* 2016, **83**, 24-151.
195. H. Zhu, J. Wang, Z. Gong, Y. D. Kim, J. Hone and X. Y. Zhu, Interfacial Charge Transfer Circumventing Momentum Mismatch at Two-Dimensional Van der Waals Heterojunctions, *Nano Lett.,* 2017, **17**, 3591-3598.
196. P. K. Gogoi, Y.-C. Lin, R. Senga, H.-P. Komsa, S. L. Wong, D. Chi, A. V. Krasheninnikov, L.-J. Li, M. B. H. Breese, S. J. Pennycook, A. T. S. Wee and K. Suenaga, Layer Rotation-Angle-Dependent Excitonic Absorption in Van der Waals Heterostructures Revealed by Electron Energy Loss Spectroscopy, *ACS Nano,* 2019, **13**, 9541-9550.
197. F. Liu, Q. Li and X. Y. Zhu, Direct Determination of Momentum-Resolved Electron Transfer in the Photoexcited Van der Waals Heterobilayer WS2/MoS2, *Phys. Rev. B,* 2020, **101**, 201405.
198. A. Surrente, D. Dumcenco, Z. Yang, A. Kuc, Y. Jing, T. Heine, Y.-C. Kung, D. K. Maude, A. Kis and P. Plochocka, Defect Healing and Charge Transfer-Mediated Valley Polarization in MoS2/MoSe2/MoS2 Trilayer Van der Waals Heterostructures, *Nano Lett.,* 2017, **17**, 4130-4136.
199. M. M. Glazov, T. Amand, X. Marie, D. Lagarde, L. Bouet and B. Urbaszek, Exciton Fine Structure and Spin Decoherence in Monolayers of Transition Metal Dichalcogenides, *Phys. Rev. B,* 2014, **89**, 201302.
200. C. R. Zhu, K. Zhang, M. Glazov, B. Urbaszek, T. Amand, Z. W. Ji, B. L. Liu and X. Marie, Exciton Valley Dynamics Probed by Kerr Rotation in WSe2 Monolayers, *Phys. Rev. B,* 2014, **90**, 161302.
201. T. Yu and M. W. Wu, Valley Depolarization Due to Intervalley and Intravalley Electron-Hole Exchange Interactions in Monolayer MoS2, *Phys. Rev. B,* 2014, **89**, 205303.
202. M. Z. Maialle, E. A. de Andrada e Silva and L. J. Sham, Exciton Spin Dynamics in Quantum Wells, *Phys. Rev. B,* 1993, **47**, 15776-15788.
203. F. Ceballos, M.-G. Ju, S. D. Lane, X. C. Zeng and H. Zhao, Highly Efficient and Anomalous Charge Transfer in Van der Waals Trilayer Semiconductors, *Nano Lett.,* 2017, **17**, 1623-1628.
204. P. Zereshki, Y. Wei, R. Long and H. Zhao, Layer-Coupled States Facilitate Ultrafast Charge Transfer in a Transition Metal Dichalcogenide Trilayer Heterostructure, *J. Phys. Chem. Lett.,* 2018, **9**, 5970-5978.
205. M.-Y. Li, Y. Shi, C.-C. Cheng, L.-S. Lu, Y.-C. Lin, H.-L. Tang, M.-L. Tsai, C.-W. Chu, K.-H. Wei, J.-H. He, W.-H. Chang, K. Suenaga and L.-J. Li, Epitaxial Growth of a Monolayer WSe2/MoS2 Lateral P-N Junction with an Atomically Sharp Interface, *Science,* 2015, **349**, 524-528.
206. X. Duan, C. Wang, J. C. Shaw, R. Cheng, Y. Chen, H. Li, X. Wu, Y. Tang, Q. Zhang, A. Pan, J. Jiang, R. Yu, Y. Huang and X. Duan, Lateral Epitaxial Growth of Two-Dimensional Layered Semiconductor Heterojunctions, *Nat. Nanotechnol.,* 2014, **9**, 1024-1030.
207. C. Huang, S. Wu, A. M. Sanchez, J. J. P. Peters, R. Beanland, J. S. Ross, P. Rivera, W. Yao, D. H. Cobden and X. Xu, Lateral Heterojunctions within Monolayer MoSe2–WSe2 Semiconductors, *Nat. Mater.,* 2014, **13**, 1096-1101.

208. Y. Gong, J. Lin, X. Wang, G. Shi, S. Lei, Z. Lin, X. Zou, G. Ye, R. Vajtai, B. I. Yakobson, H. Terrones, M. Terrones, Beng K. Tay, J. Lou, S. T. Pantelides, Z. Liu, W. Zhou and P. M. Ajayan, Vertical and in-Plane Heterostructures from WS2/MoS2 Monolayers, *Nat. Mater.,* 2014, **13**, 1135-1142.
209. M. Mahjouri-Samani, M.-W. Lin, K. Wang, A. R. Lupini, J. Lee, L. Basile, A. Boulesbaa, C. M. Rouleau, A. A. Puretzky, I. N. Ivanov, K. Xiao, M. Yoon and D. B. Geohegan, Patterned Arrays of Lateral Heterojunctions within Monolayer Two-Dimensional Semiconductors, *Nat. Commun.,* 2015, **6**, 7749.
210. K. Chen, X. Wan, W. Xie, J. Wen, Z. Kang, X. Zeng, H. Chen and J. Xu, Lateral Built-in Potential of Monolayer MoS2–WS2 in-Plane Heterostructures by a Shortcut Growth Strategy, *Adv. Mater.,* 2015, **27**, 6431-6437.
211. W. Zhou, Y.-Y. Zhang, J. Chen, D. Li, J. Zhou, Z. Liu, M. F. Chisholm, S. T. Pantelides and K. P. Loh, Dislocation-Driven Growth of Two-Dimensional Lateral Quantum-Well Superlattices, *Sci. Adv.,* 2018, **4**, eaap9096.
212. M. Z. Bellus, M. Mahjouri-Samani, S. D. Lane, A. D. Oyedele, X. Li, A. A. Puretzky, D. Geohegan, K. Xiao and H. Zhao, Photocarrier Transfer across Monolayer MoS2–MoSe2 Lateral Heterojunctions, *ACS Nano,* 2018, **12**, 7086-7092.
213. P. K. Sahoo, S. Memaran, Y. Xin, L. Balicas and H. R. Gutiérrez, One-Pot Growth of Two-Dimensional Lateral Heterostructures via Sequential Edge-Epitaxy, *Nature,* 2018, **553**, 63-67.
214. J. Kang, H. Sahin and F. M. Peeters, Tuning Carrier Confinement in the MoS2/WS2 Lateral Heterostructure, *J. Phys. Chem. C,* 2015, **119**, 9580-9586.
215. Y. Guo and J. Robertson, Band Engineering in Transition Metal Dichalcogenides: Stacked Versus Lateral Heterostructures, *Appl. Phys. Lett.,* 2016, **108**, 233104.
216. Y. Yang, W.-H. Fang and R. Long, Disparity in Photoexcitation Dynamics between Vertical and Lateral MoS2/WSe2 Heterojunctions: Time-Domain Simulation Emphasizes the Importance of Donor–Acceptor Interaction and Band Alignment, *J. Phys. Chem. Lett.,* 2017, **8**, 5771-5778.
217. C. Zhang, M.-Y. Li, J. Tersoff, Y. Han, Y. Su, L.-J. Li, D. A. Muller and C.-K. Shih, Strain Distributions and Their Influence on Electronic Structures of WSe2–MoS2 Laterally Strained Heterojunctions, *Nat. Nanotechnol.,* 2018, **13**, 152-158.
218. P. K. Sahoo, S. Memaran, F. A. Nugera, Y. Xin, T. Díaz Márquez, Z. Lu, W. Zheng, N. D. Zhigadlo, D. Smirnov, L. Balicas and H. R. Gutiérrez, Bilayer Lateral Heterostructures of Transition-Metal Dichalcogenides and Their Optoelectronic Response, *ACS Nano,* 2019, **13**, 12372-12384.
219. H. Yao, L. Ye, H. Zhang, S. Li, S. Zhang and J. Hou, Molecular Design of Benzodithiophene-Based Organic Photovoltaic Materials, *Chem. Rev.,* 2016, **116**, 7397-7457.
220. A. Wadsworth, M. Moser, A. Marks, M. S. Little, N. Gasparini, C. J. Brabec, D. Baran and I. McCulloch, Critical Review of the Molecular Design Progress in Non-Fullerene Electron Acceptors Towards Commercially Viable Organic Solar Cells, *Chem. Soc. Rev.,* 2019, **48**, 1596-1625.
221. J.-H. Park, U.-Y. Kim, B.-M. Kim, W.-H. Kim, D.-H. Roh, J. S. Kim and T.-H. Kwon, Molecular Design Strategy toward Robust Organic Dyes in Thin-Film Photoanodes, *ACS Appl. Energy Mater.,* 2019, **2**, 4674-4682.

222. D. B. Sulas, A. E. London, L. Huang, L. Xu, Z. Wu, T. N. Ng, B. M. Wong, C. W. Schlenker, J. D. Azoulay and M. Y. Sfeir, Preferential Charge Generation at Aggregate Sites in Narrow Band Gap Infrared Photoresponsive Polymer Semiconductors, *Adv. Opt. Mater.,* 2018, **6**, 1701138.
223. Y. Zhang, S. Liu, W. Liu, T. Liang, X. Yang, M. Xu and H. Chen, Two-Dimensional MoS2-Assisted Immediate Aggregation of Poly-3-Hexylthiophene with High Mobility, *Phys. Chem. Chem. Phys.,* 2015, **17**, 27565-27572.
224. X. Lin, J. C. Lu, Y. Shao, Y. Y. Zhang, X. Wu, J. B. Pan, L. Gao, S. Y. Zhu, K. Qian, Y. F. Zhang, D. L. Bao, L. F. Li, Y. Q. Wang, Z. L. Liu, J. T. Sun, T. Lei, C. Liu, J. O. Wang, K. Ibrahim, D. N. Leonard, W. Zhou, H. M. Guo, Y. L. Wang, S. X. Du, S. T. Pantelides and H. J. Gao, Intrinsically Patterned Two-Dimensional Materials for Selective Adsorption of Molecules And nanoclusters, *Nat. Mater.,* 2017, **16**, 717.
225. J. H. Park, A. Sanne, Y. Guo, M. Amani, K. Zhang, H. C. P. Movva, J. A. Robinson, A. Javey, J. Robertson, S. K. Banerjee and A. C. Kummel, Defect Passivation of Transition Metal Dichalcogenides via a Charge Transfer Van der Waals Interface, *Sci. Adv.,* 2017, **3**, e1701661.
226. Y. Huang, F. Zhuge, J. Hou, L. Lv, P. Luo, N. Zhou, L. Gan and T. Zhai, Van der Waals Coupled Organic Molecules with Monolayer MoS2 for Fast Response Photodetectors with Gate-Tunable Responsivity, *ACS Nano,* 2018, **12**, 4062-4073.
227. A. Förster, S. Gemming, G. Seifert and D. Tománek, Chemical and Electronic Repair Mechanism of Defects in MoS2 Monolayers, *ACS Nano,* 2017, **11**, 9989-9996.
228. J. Wang, Z. Ji, G. Yang, X. Chuai, F. Liu, Z. Zhou, C. Lu, W. Wei, X. Shi, J. Niu, L. Wang, H. Wang, J. Chen, N. Lu, C. Jiang, L. Li and M. Liu, Charge Transfer within the F4tcnq-MoS2 Van der Waals Interface: Toward Electrical Properties Tuning and Gas Sensing Application, *Adv. Funct. Mater.,* 2018, **28**, 1806244.
229. S. Bertolazzi, M. Gobbi, Y. Zhao, C. Backes and P. Samorì, Molecular Chemistry Approaches for Tuning the Properties of Two-Dimensional Transition Metal Dichalcogenides, *Chem. Soc. Rev.,* 2018, **47**, 6845-6888.
230. H. Schmidt, F. Giustiniano and G. Eda, Electronic Transport Properties of Transition Metal Dichalcogenide Field-Effect Devices: Surface and Interface Effects, *Chem. Soc. Rev.,* 2015, **44**, 7715-7736.
231. S. Mouri, Y. Miyauchi and K. Matsuda, Tunable Photoluminescence of Monolayer MoS2 via Chemical Doping, *Nano Lett.,* 2013, **13**, 5944-5948.
232. S. Bettis Homan, V. K. Sangwan, I. Balla, H. Bergeron, E. A. Weiss and M. C. Hersam, Ultrafast Exciton Dissociation and Long-Lived Charge Separation in a Photovoltaic Pentacene–MoS2 Van der Waals Heterojunction, *Nano Lett.,* 2017, **17**, 164-169.
233. D. Jariwala, S. L. Howell, K.-S. Chen, J. Kang, V. K. Sangwan, S. A. Filippone, R. Turrisi, T. J. Marks, L. J. Lauhon and M. C. Hersam, Hybrid, Gate-Tunable, Van der Waals P–N Heterojunctions from Pentacene and MoS2, *Nano Lett.,* 2016, **16**, 497-503.
234. H. Huang, Y. Huang, S. Wang, M. Zhu, H. Xie, L. Zhang, X. Zheng, Q. Xie, D. Niu and Y. Gao, Van Der Waals Heterostructures between Small Organic Molecules and Layered Substrates, *Crystals,* 2016, **6**, 113.
235. S. H. Amsterdam, T. K. Stanev, Q. Zhou, A. J. T. Lou, H. Bergeron, P. Darancet, M. C. Hersam, N. P. Stern and T. J. Marks, Electronic Coupling in Metallophthalocyanine–Transition Metal Dichalcogenide Mixed-Dimensional Heterojunctions, *ACS Nano,* 2019, **13**, 4183-4190.

236. S. Padgaonkar, S. H. Amsterdam, H. Bergeron, K. Su, T. J. Marks, M. C. Hersam and E. A. Weiss, Molecular-Orientation-Dependent Interfacial Charge Transfer in Phthalocyanine/MoS2 Mixed-Dimensional Heterojunctions, *J. Phys. Chem. C,* 2019, **123**, 13337-13343.
237. X.-Y. Liu, X.-Y. Xie, W.-H. Fang and G. Cui, Theoretical Insights into Interfacial Electron Transfer between Zinc Phthalocyanine and Molybdenum Disulfide, *J. Phys. Chem. A,* 2018, **122**, 9587-9596.
238. S. Vélez, D. Ciudad, J. Island, M. Buscema, O. Txoperena, S. Parui, G. A. Steele, F. Casanova, H. S. J. van der Zant, A. Castellanos-Gomez and L. E. Hueso, Gate-Tunable Diode and Photovoltaic Effect in an Organic–2D Layered Material P–N Junction, *Nanoscale,* 2015, **7**, 15442-15449.
239. P. Choudhury, L. Ravavarapu, R. Dekle and S. Chowdhury, Modulating Electronic and Optical Properties of Monolayer MoS2 Using Nonbonded Phthalocyanine Molecules, *J. Phys. Chem. C,* 2017, **121**, 2959-2967.
240. H. Zhang, J. Choi, A. Ramani, D. Voiry, S. N. Natoli, M. Chhowalla, D. R. McMillin and J. H. Choi, Engineering Chemically Exfoliated Large-Area Two-Dimensional MoS2 Nanolayers with Porphyrins for Improved Light Harvesting, *ChemPhysChem,* 2016, **17**, 2854-2862.
241. J.-K. Kim, K. Cho, T.-Y. Kim, J. Pak, J. Jang, Y. Song, Y. Kim, B. Y. Choi, S. Chung, W.-K. Hong and T. Lee, Trap-Mediated Electronic Transport Properties of Gate-Tunable Pentacene/MoS2 P-N Heterojunction Diodes, *Sci. Rep.,* 2016, **6**, 36775.
242. X.-Y. Xie, X.-Y. Liu, Q. Fang, W.-H. Fang and G. Cui, Photoinduced Carrier Dynamics at the Interface of Pentacene and Molybdenum Disulfide, *J. Phys. Chem. A,* 2019, **123**, 7693-7703.
243. X. Yu, A. Rahmanudin, X. A. Jeanbourquin, D. Tsokkou, N. Guijarro, N. Banerji and K. Sivula, Hybrid Heterojunctions of Solution-Processed Semiconducting 2D Transition Metal Dichalcogenides, *ACS Energy Lett.,* 2017, **2**, 524-531.
244. X. Liu, J. Gu, K. Ding, D. Fan, X. Hu, Y.-W. Tseng, Y.-H. Lee, V. Menon and S. R. Forrest, Photoresponse of an Organic Semiconductor/Two-Dimensional Transition Metal Dichalcogenide Heterojunction, *Nano Lett.,* 2017, **17**, 3176-3181.
245. Arramel, X. Yin, Q. Wang, Y. J. Zheng, Z. Song, M. H. bin Hassan, D. Qi, J. Wu, A. Rusydi and A. T. S. Wee, Molecular Alignment and Electronic Structure of N,N'-Dibutyl-3,4,9,10-Perylene-Tetracarboxylic-Diimide Molecules on MoS2 Surfaces, *ACS Appl. Mater. Interfaces,* 2017, **9**, 5566-5573.
246. J. Baek, T. Umeyama, W. Choi, Y. Tsutsui, H. Yamada, S. Seki and H. Imahori, Formation and Photodynamic Behavior of Transition Metal Dichalcogenide Nanosheet–Fullerene Inorganic/Organic Nanohybrids on Semiconducting Electrodes, *Chem. Eur. J.,* 2018, **24**, 1561-1572.
247. M. Chen, R. Guan and S. Yang, Hybrids of Fullerenes and 2D Nanomaterials, *Adv. Sci.,* 2019, **6**, 1800941.
248. C.-H. Cheng, Z. Li, A. Hambarde and P. B. Deotare, Efficient Energy Transfer across Organic–2D Inorganic Heterointerfaces, *ACS Appl. Mater. Interfaces,* 2018, **10**, 39336-39342.
249. L. G. Kaake, P. F. Barbara and X. Y. Zhu, Intrinsic Charge Trapping in Organic and Polymeric Semiconductors: A Physical Chemistry Perspective, *J. Phys. Chem. Lett.,* 2010, **1**, 628-635.
250. K. Keyshar, M. Berg, X. Zhang, R. Vajtai, G. Gupta, C. K. Chan, T. E. Beechem, P. M. Ajayan, A. D. Mohite and T. Ohta, Experimental Determination of the Ionization Energies of

MoSe2, WS2, and MoS2 on SiO2 Using Photoemission Electron Microscopy, *ACS Nano,* 2017, **11**, 8223-8230.
251. H. S. Kang, T. J. Sisto, S. Peurifoy, D. H. Arias, B. Zhang, C. Nuckolls and J. L. Blackburn, Long-Lived Charge Separation at Heterojunctions between Semiconducting Single-Walled Carbon Nanotubes and Perylene Diimide Electron Acceptors, *J. Phys. Chem. C,* 2018, **122**, 14150-14161.
252. H. Sun, S. Ryno, C. Zhong, M. K. Ravva, Z. Sun, T. Körzdörfer and J.-L. Brédas, Ionization Energies, Electron Affinities, and Polarization Energies of Organic Molecular Crystals: Quantitative Estimations from a Polarizable Continuum Model (PCM)-Tuned Range-Separated Density Functional Approach, *J. Chem. Theory Comput.,* 2016, **12**, 2906-2916.
253. Y.-Y. Du, D.-Q. Lin, G.-H. Chen, X.-Y. Bai, L.-X. Wang, R. Wu, J.-O. Wang, H.-J. Qian and H.-N. Li, Electronic States and Molecular Orientation of Itic Film, *Chin. Phys. B,* 2018, **27**, 088801.
254. H. Yoshida, K. Yamada, J. y. Tsutsumi and N. Sato, Complete Description of Ionization Energy and Electron Affinity in Organic Solids: Determining Contributions from Electronic Polarization, Energy Band Dispersion, and Molecular Orientation, *Phys. Rev. B,* 2015, **92**, 075145.
255. C. Wang, A. J. Turinske and Y. Gao, Orientation-Dependent Ionization Potential of CuPc and Energy Level Alignment at C60/CuPc Interface, *Appl. Phys. B,* 2013, **113**, 361-365.
256. W. Chen, H. Huang, S. Chen, Y. L. Huang, X. Y. Gao and A. T. S. Wee, Molecular Orientation-Dependent Ionization Potential of Organic Thin Films, *Chem. Mater.,* 2008, **20**, 7017-7021.
257. W. Gao and A. Kahn, Electronic Structure and Current Injection in Zinc Phthalocyanine Doped with Tetrafluorotetracyanoquinodimethane: Interface Versus Bulk Effects, *Org. Electron.,* 2002, **3**, 53-63.
258. J. Endres, I. Pelczer, B. P. Rand and A. Kahn, Determination of Energy Level Alignment within an Energy Cascade Organic Solar Cell, *Chem. Mater.,* 2016, **28**, 794-801.
259. J. Yoo, K. Jung, J. Jeong, G. Hyun, H. Lee and Y. Yi, Energy Level Alignment at C60/DTDCTB/PEDOT:Pss Interfaces in Organic Photovoltaics, *Appl. Surf. Sci.,* 2017, **402**, 41-46.
260. E. L. Ratcliff, R. C. Bakus Ii, G. C. Welch, T. S. van der Poll, A. Garcia, S. R. Cowan, B. A. MacLeod, D. S. Ginley, G. C. Bazan and D. C. Olson, Formation of Interfacial Traps Upon Surface Protonation in Small Molecule Solution Processed Bulk Heterojunctions Probed by Photoelectron Spectroscopy, *J. Mater. Chem. C,* 2013, **1**, 6223-6234.
261. L.-Y. Gan, Q. Zhang, Y. Cheng and U. Schwingenschlögl, Photovoltaic Heterojunctions of Fullerenes with MoS2 and WS2 Monolayers, *J. Phys. Chem. Lett.,* 2014, **5**, 1445-1449.
262. D. B. Sulas, E. J. Rabe and C. W. Schlenker, Kinetic Competition between Charge Separation and Triplet Formation in Small-Molecule Photovoltaic Blends, *J. Phys. Chem. C,* 2017, **121**, 26667-26676.
263. R. M. Williams, H.-C. Chen, D. Di Nuzzo, S. C. J. Meskers and R. A. J. Janssen, Ultrafast Charge and Triplet State Formation in Diketopyrrolopyrrole Low Band Gap Polymer/Fullerene Blends: Influence of Nanoscale Morphology of Organic Photovoltaic Materials on Charge Recombination to the Triplet State, *J. Spectrosc.,* 2017, **2017**, 6867507.
264. S. D. Dimitrov, S. Wheeler, D. Niedzialek, B. C. Schroeder, H. Utzat, J. M. Frost, J. Yao, A. Gillett, P. S. Tuladhar, I. McCulloch, J. Nelson and J. R. Durrant, Polaron Pair Mediated Triplet Generation in Polymer/Fullerene Blends, *Nat. Commun.,* 2015, **6**, 6501.

265. D. N. Congreve, J. Lee, N. J. Thompson, E. Hontz, S. R. Yost, P. D. Reusswig, M. E. Bahlke, S. Reineke, T. Van Voorhis and M. A. Baldo, External Quantum Efficiency above 100% in a Singlet-Exciton-Fission–Based Organic Photovoltaic Cell, *Science,* 2013, **340**, 334.
266. N. Monahan and X. Y. Zhu, Charge Transfer–Mediated Singlet Fission, *Annu. Rev. Phys. Chem.,* 2015, **66**, 601-618.
267. C. E. Petoukhoff, S. Kosar, M. Goto, I. Bozkurt, M. Chhowalla and K. M. Dani, Charge Transfer Dynamics in Conjugated Polymer/MoS2 Organic/2D Heterojunctions, *Mol. Syst. Des. Eng.,* 2019, **4**, 929-938.
268. Y. Garcia-Basabe, G. G. Parra, M. B. Barioni, C. D. Mendoza, F. C. Vicentin and D. G. Larrudé, Species Selective Charge Transfer Dynamics in a P3HT/MoS2 Van der Waals Heterojunction: Fluorescence Lifetime Microscopy and Core Hole Clock Spectroscopy Approaches, *Phys. Chem. Chem. Phys.,* 2019, **21**, 23521-23532.
269. B. Sun, Z. Su, Y. Hao, J. Pei and Y. Li, Facile Fabrication of MoS2-P3HT Hybrid Microheterostructure with Enhanced Photovoltaic Performance in TiO2 Nanorod Array Based Hybrid Solar Cell, *Solid State Sci.,* 2019, **94**, 92-98.
270. A. S. Sarkar and S. K. Pal, A Van der Waals P–N Heterojunction Based on Polymer-2D Layered MoS2 for Solution Processable Electronics, *J. Phys. Chem. C,* 2017, **121**, 21945-21954.
271. C. Zhong, V. K. Sangwan, C. Wang, H. Bergeron, M. C. Hersam and E. A. Weiss, Mechanisms of Ultrafast Charge Separation in a PTB7/Monolayer MoS2 Van der Waals Heterojunction, *J. Phys. Chem. Lett.,* 2018, **9**, 2484-2491.
272. X.-Y. Liu, W.-K. Chen, W.-H. Fang and G. Cui, Nonadiabatic Dynamics Simulations Reveal Distinct Effects of the Thickness of PTB7 on Interfacial Electron and Hole Transfer Dynamics in PTB7@MoS2 Heterostructures, *J. Phys. Chem. Lett.,* 2019, **10**, 2949-2956.
273. T. A. Shastry, I. Balla, H. Bergeron, S. H. Amsterdam, T. J. Marks and M. C. Hersam, Mutual Photoluminescence Quenching and Photovoltaic Effect in Large-Area Single-Layer MoS2–Polymer Heterojunctions, *ACS Nano,* 2016, **10**, 10573-10579.
274. C. E. Petoukhoff, M. B. M. Krishna, D. Voiry, I. Bozkurt, S. Deckoff-Jones, M. Chhowalla, D. M. O'Carroll and K. M. Dani, Ultrafast Charge Transfer and Enhanced Absorption in MoS2–Organic Van der Waals Heterojunctions Using Plasmonic Metasurfaces, *ACS Nano,* 2016, **10**, 9899-9908.
275. E. Singh, K. S. Kim, G. Y. Yeom and H. S. Nalwa, Atomically Thin-Layered Molybdenum Disulfide (MoS2) for Bulk-Heterojunction Solar Cells, *ACS Appl. Mater. Interfaces,* 2017, **9**, 3223-3245.
276. S. Bellani, L. Najafi, A. Capasso, A. E. Del Rio Castillo, M. R. Antognazza and F. Bonaccorso, Few-Layer MoS2 Flakes as a Hole-Selective Layer for Solution-Processed Hybrid Organic Hydrogen-Evolving Photocathodes, *J. Mater. Chem. A,* 2017, **5**, 4384-4396.
277. J. L. Blackburn, A. J. Ferguson and O. G. Reid, Spectroscopy of Ground- and Excited-State Charge Carriers in Single-Wall Carbon Nanotubes. In *Handbook of Carbon Nanomaterials*, World Scientific: 2017; Vol. Volume 9 & 10, pp 237-296.
278. J. L. Blackburn, Semiconducting Single-Walled Carbon Nanotubes in Solar Energy Harvesting, *ACS Energy Lett.,* 2017, **2**, 1598-1613.
279. D. Jariwala, V. K. Sangwan, C.-C. Wu, P. L. Prabhumirashi, M. L. Geier, T. J. Marks, L. J. Lauhon and M. C. Hersam, Gate-Tunable Carbon Nanotube–MoS2 Heterojunction P-N Diode, *Proc. Natl. Acad. Sci.,* 2013, **110**, 18076-18080.

280. J. Zhang, Y. Wei, F. Yao, D. Li, H. Ma, P. Lei, H. Fang, X. Xiao, Z. Lu, J. Yang, J. Li, L. Jiao, W. Hu, K. Liu, K. Liu, P. Liu, Q. Li, W. Lu, S. Fan and K. Jiang, SWCNT-MoS2-SWCNT Vertical Point Heterostructures, *Adv. Mater.,* 2017, **29**, 1604469.
281. P. Li, Z. Yang, J. Shen, H. Nie, Q. Cai, L. Li, M. Ge, C. Gu, X. a. Chen, K. Yang, L. Zhang, Y. Chen and S. Huang, Subnanometer Molybdenum Sulfide on Carbon Nanotubes as a Highly Active and Stable Electrocatalyst for Hydrogen Evolution Reaction, *ACS Appl. Mater. Interfaces,* 2016, **8**, 3543-3550.
282. H. Huang, W. Huang, Z. Yang, J. Huang, J. Lin, W. Liu and Y. Liu, Strongly Coupled MoS2 Nanoflake–Carbon Nanotube Nanocomposite as an Excellent Electrocatalyst for Hydrogen Evolution Reaction, *J. Mater. Chem. A,* 2017, **5**, 1558-1566.
283. R. Xiang, T. Inoue, Y. Zheng, A. Kumamoto, Y. Qian, Y. Sato, M. Liu, D. Tang, D. Gokhale, J. Guo, K. Hisama, S. Yotsumoto, T. Ogamoto, H. Arai, Y. Kobayashi, H. Zhang, B. Hou, A. Anisimov, M. Maruyama, Y. Miyata, S. Okada, S. Chiashi, Y. Li, J. Kong, E. I. Kauppinen, Y. Ikuhara, K. Suenaga and S. Maruyama, One-Dimensional Van der Waals Heterostructures, *Science,* 2020, **367**, 537-542.
284. C. Liu, H. Hong, Q. Wang, P. Liu, Y. Zuo, J. Liang, Y. Cheng, X. Zhou, J. Wang, Y. Zhao, J. Xiong, B. Xiang, J. Zhang and K. Liu, Strong-Coupled Hybrid Structure of Carbon Nanotube and MoS2 Monolayer with Ultrafast Interfacial Charge Transfer, *Nanoscale,* 2019, **11**, 17195-17200.
285. G. Cheng, B. Li, C. Zhao, X. Yan, H. Wang, K. M. Lau and J. Wang, Interfacially Bound Exciton State in a Hybrid Structure of Monolayer WS2 and Ingan Quantum Dots, *Nano Lett.,* 2018, **18**, 5640-5645.
286. J. S. Shaikh, N. S. Shaikh, S. S. Mali, J. V. Patil, S. A. Beknalkar, A. P. Patil, N. L. Tarwal, P. Kanjanaboos, C. K. Hong and P. S. Patil, Quantum Dot Based Solar Cells: Role of Nanoarchitectures, Perovskite Quantum Dots, and Charge-Transporting Layers, *ChemSusChem,* 2019, **12**, 4724-4753.
287. S. Zhang, X. Wang, Y. Chen, G. Wu, Y. Tang, L. Zhu, H. Wang, W. Jiang, L. Sun, T. Lin, H. Shen, W. Hu, J. Ge, J. Wang, X. Meng and J. Chu, Ultrasensitive Hybrid MoS2–ZnCdSe Quantum Dot Photodetectors with High Gain, *ACS Appl. Mater. Interfaces,* 2019, **11**, 23667-23672.
288. Y. Zhong, Y. Shao, F. Ma, Y. Wu, B. Huang and X. Hao, Band-Gap-Matched CdSe QD/WS2 Nanosheet Composite: Size-Controlled Photocatalyst for High-Efficiency Water Splitting, *Nano Energy,* 2017, **31**, 84-89.
289. T. Frecker, D. Bailey, X. Arzeta-Ferrer, J. McBride and S. J. Rosenthal, Review—Quantum Dots and Their Application in Lighting, Displays, and Biology, *ECS J. Solid State. Sci. Technol.,* 2016, **5**, R3019-R3031.
290. C. G. Eder, Y. Voronko, C. Hirschl, R. Ebner, G. Újvári and W. Mühleisen, Non-Destructive Failure Detection and Visualization of Artificially and Naturally Aged PV Modules, *Energies,* 2018, **11**.
291. A. Boulesbaa, K. Wang, M. Mahjouri-Samani, M. Tian, A. A. Puretzky, I. Ivanov, C. M. Rouleau, K. Xiao, B. G. Sumpter and D. B. Geohegan, Ultrafast Charge Transfer and Hybrid Exciton Formation in 2D/0D Heterostructures, *J. Am. Chem. Soc.,* 2016, **138**, 14713-14719.
292. D. Kufer, I. Nikitskiy, T. Lasanta, G. Navickaite, F. H. L. Koppens and G. Konstantatos, Hybrid 2D–0D MoS2–PbS Quantum Dot Photodetectors, *Adv. Mater.,* 2015, **27**, 176-180.

293. C. Hu, D. Dong, X. Yang, K. Qiao, D. Yang, H. Deng, S. Yuan, J. Khan, Y. Lan, H. Song and J. Tang, Synergistic Effect of Hybrid PbS Quantum Dots/2D-WSe2 toward High Performance and Broadband Phototransistors, *Adv. Funct. Mater.,* 2017, **27**, 1603605.
294. O. Özdemir, I. Ramiro, S. Gupta and G. Konstantatos, High Sensitivity Hybrid PbS CQD-TMDC Photodetectors up to 2 Mm, *ACS Photonics,* 2019, **6**, 2381-2386.
295. F. Prins, A. J. Goodman and W. A. Tisdale, Reduced Dielectric Screening and Enhanced Energy Transfer in Single- and Few-Layer MoS2, *Nano Lett.,* 2014, **14**, 6087-6091.
296. R. Ahmad, R. Srivastava, S. Yadav, D. Singh, G. Gupta, S. Chand and S. Sapra, Functionalized Molybdenum Disulfide Nanosheets for 0D–2D Hybrid Nanostructures: Photoinduced Charge Transfer and Enhanced Photoresponse, *J. Phys. Chem. Lett.,* 2017, **8**, 1729-1738.
297. Q. Wang, Y. Wen, K. Cai, R. Cheng, L. Yin, Y. Zhang, J. Li, Z. Wang, F. Wang, F. Wang, T. A. Shifa, C. Jiang, H. Yang and J. He, Nonvolatile Infrared Memory in MoS2/PbS Van der Waals Heterostructures, *Sci. Adv.,* 2018, **4**, eaap7916.
298. A. K. Jena, A. Kulkarni and T. Miyasaka, Halide Perovskite Photovoltaics: Background, Status, and Future Prospects, *Chem. Rev.,* 2019, **119**, 3036-3103.
299. National Renewable Energy Laboratory, Nreljournal and Proceedings of the Royal Society of New South Wales Best Research-Cell Efficiencies. https://www.nrel.gov/pv/assets/pdfs/best-research-cell-efficiencies.20190802.pdf (accessed April 13, 2020).
300. Z.-K. Tan, R. S. Moghaddam, M. L. Lai, P. Docampo, R. Higler, F. Deschler, M. Price, A. Sadhanala, L. M. Pazos, D. Credgington, F. Hanusch, T. Bein, H. J. Snaith and R. H. Friend, Bright Light-Emitting Diodes Based on Organometal Halide Perovskite, *Nat. Nanotechnol.,* 2014, **9**, 687-692.
301. Z. Wei and J. Xing, The Rise of Perovskite Light-Emitting Diodes, *J. Phys. Chem. Lett.,* 2019, **10**, 3035-3042.
302. P. Odenthal, W. Talmadge, N. Gundlach, R. Wang, C. Zhang, D. Sun, Z.-G. Yu, Z. Valy Vardeny and Y. S. Li, Spin-Polarized Exciton Quantum Beating in Hybrid Organic–Inorganic Perovskites, *Nat. Phys.,* 2017, **13**, 894-899.
303. Y. Zhai, S. Baniya, C. Zhang, J. Li, P. Haney, C.-X. Sheng, E. Ehrenfreund and Z. V. Vardeny, Giant Rashba Splitting in 2D Organic-Inorganic Halide Perovskites Measured by Transient Spectroscopies, *Sci. Adv.,* 2017, **3**, e1700704.
304. H. Lu, J. Wang, C. Xiao, X. Pan, X. Chen, R. Brunecky, J. J. Berry, K. Zhu, M. C. Beard and Z. V. Vardeny, Spin-Dependent Charge Transport through 2D Chiral Hybrid Lead-Iodide Perovskites, *Sci. Adv.,* 2019, **5**, eaay0571.
305. Z. Liu, K. Liu, F. Zhang, S. M. Jain, T. He, Y. Jiang, P. Liu, J. Yang, H. Liu and M. Yuan, CH3NH3PbI3:MoS2 Heterostructure for Stable and Efficient Inverted Perovskite Solar Cell, *Sol. Energy,* 2020, **195**, 436-445.
306. R. Singh, A. Giri, M. Pal, K. Thiyagarajan, J. Kwak, J.-J. Lee, U. Jeong and K. Cho, Perovskite Solar Cells with an MoS2 Electron Transport Layer, *J. Mater. Chem. A,* 2019, **7**, 7151-7158.
307. U. Dasgupta, S. Chatterjee and A. J. Pal, Thin-Film Formation of 2D MoS2 and Its Application as a Hole-Transport Layer in Planar Perovskite Solar Cells, *Sol. Energy Mater. Sol. Cells,* 2017, **172**, 353-360.

308. A. Capasso, F. Matteocci, L. Najafi, M. Prato, J. Buha, L. Cinà, V. Pellegrini, A. D. Carlo and F. Bonaccorso, Few-Layer MoS2 Flakes as Active Buffer Layer for Stable Perovskite Solar Cells, *Adv. Energy Mater.,* 2016, **6**, 1600920.
309. Y. Wang, R. Fullon, M. Acerce, C. E. Petoukhoff, J. Yang, C. Chen, S. Du, S. K. Lai, S. P. Lau, D. Voiry, D. O'Carroll, G. Gupta, A. D. Mohite, S. Zhang, H. Zhou and M. Chhowalla, Solution-Processed MoS2/Organolead Trihalide Perovskite Photodetectors, *Adv. Mater.,* 2017, **29**, 1603995.
310. X. Song, X. Liu, D. Yu, C. Huo, J. Ji, X. Li, S. Zhang, Y. Zou, G. Zhu, Y. Wang, M. Wu, A. Xie and H. Zeng, Boosting Two-Dimensional MoS2/CsPbBr3 Photodetectors via Enhanced Light Absorbance and Interfacial Carrier Separation, *ACS Appl. Mater. Interfaces,* 2018, **10**, 2801-2809.
311. C. Fang, H. Wang, Z. Shen, H. Shen, S. Wang, J. Ma, J. Wang, H. Luo and D. Li, High-Performance Photodetectors Based on Lead-Free 2D Ruddlesden–Popper Perovskite/MoS2 Heterostructures, *ACS Appl. Mater. Interfaces,* 2019, **11**, 8419-8427.
312. F. Bai, J. Qi, F. Li, Y. Fang, W. Han, H. Wu and Y. Zhang, A High-Performance Self-Powered Photodetector Based on Monolayer MoS2/Perovskite Heterostructures, *Adv. Mater. Interfaces,* 2018, **5**, 1701275.
313. R. Ihly, A.-M. Dowgiallo, M. Yang, P. Schulz, N. J. Stanton, O. G. Reid, A. J. Ferguson, K. Zhu, J. J. Berry and J. L. Blackburn, Efficient Charge Extraction and Slow Recombination in Organic-Inorganic Perovskites Capped with Semiconducting Single-Walled Carbon Nanotubes, *Energy Environ. Sci.,* 2016, **9**, 1439-1449.
314. P. Schulz, A.-M. Dowgiallo, M. Yang, K. Zhu, J. L. Blackburn and J. J. Berry, Charge Transfer Dynamics between Carbon Nanotubes and Hybrid Organic Metal Halide Perovskite Films, *J. Phys. Chem. Lett.,* 2016, **7**, 418-425.
315. S. N. Habisreutinger, N. K. Noel, B. W. Larson, O. G. Reid and J. L. Blackburn, Rapid Charge-Transfer Cascade through SWCNT Composites Enabling Low-Voltage Losses for Perovskite Solar Cells, *ACS Energy Lett.,* 2019, **4**, 1872-1879.
316. G. Yang, H. Tao, P. Qin, W. Ke and G. Fang, Recent Progress in Electron Transport Layers for Efficient Perovskite Solar Cells, *J. Mater. Chem. A,* 2016, **4**, 3970-3990.
317. B. Peng, G. Yu, Y. Zhao, Q. Xu, G. Xing, X. Liu, D. Fu, B. Liu, J. R. S. Tan, W. Tang, H. Lu, J. Xie, L. Deng, T. C. Sum and K. P. Loh, Achieving Ultrafast Hole Transfer at the Monolayer MoS2 and CH3NH3PbI3 Perovskite Interface by Defect Engineering, *ACS Nano,* 2016, **10**, 6383-6391.
318. J. Bauer, L. S. Quintanar, K. Wang, A. A. Puretzky, K. Xiao, D. B. Geohegan and A. Boulesbaa, Ultrafast Exciton Dissociation at the 2D-WS2 Monolayer/Perovskite Interface, *J. Phys. Chem. C,* 2018, **122**, 28910-28917.
319. Y. Liu, H. Li, X. Zheng, X. Cheng and T. Jiang, Giant Photoluminescence Enhancement in Monolayer WS2 by Energy Transfer from CsPbBr3 Quantum Dots, *Opt. Mater. Express,* 2017, **7**, 1327-1334.
320. S. Wang, Q. Luo, W.-H. Fang and R. Long, Interfacial Engineering Determines Band Alignment and Steers Charge Separation and Recombination at an Inorganic Perovskite Quantum Dot/WS2 Junction: A Time Domain Ab Initio Study, *J. Phys. Chem. Lett.,* 2019, **10**, 1234-1241.

321. Q. Fang, Q. Shang, L. Zhao, R. Wang, Z. Zhang, P. Yang, X. Sui, X. Qiu, X. Liu, Q. Zhang and Y. Zhang, Ultrafast Charge Transfer in Perovskite Nanowire/2D Transition Metal Dichalcogenide Heterostructures, *J. Phys. Chem. Lett.,* 2018, **9**, 1655-1662.
322. Y. Wang, S. Zhao, Y. Wang, D. A. Laleyan, Y. Wu, B. Ouyang, P. Ou, J. Song and Z. Mi, Wafer-Scale Synthesis of Monolayer WSe2: A Multi-Functional Photocatalyst for Efficient Overall Pure Water Splitting, *Nano Energy,* 2018, **51**, 54-60.
323. Q. Ding, B. Song, P. Xu and S. Jin, Efficient Electrocatalytic and Photoelectrochemical Hydrogen Generation Using MoS2 and Related Compounds, *Chem,* 2016, **1**, 699-726.
324. X. Gan, D. Lei and K.-Y. Wong, Two-Dimensional Layered Nanomaterials for Visible-Light-Driven Photocatalytic Water Splitting, *Mater. Today Energy,* 2018, **10**, 352-367.
325. M. R. U. D. Biswas, A. Ali, K. Y. Cho and W.-C. Oh, Novel Synthesis of WSe2-Graphene-TiO2 Ternary Nanocomposite via Ultrasonic Technics for High Photocatalytic Reduction of CO2 into CH3OH, *Ultrason. Sonochem.,* 2018, **42**, 738-746.
326. A. Ali and W.-C. Oh, Preparation of Nanowire Like WSe2-Graphene Nanocomposite for Photocatalytic Reduction of CO2 into CH3OH with the Presence of Sacrificial Agents, *Sci. Rep.,* 2017, **7**, 1867.
327. W. Dai, J. Yu, Y. Deng, X. Hu, T. Wang and X. Luo, Facile Synthesis of MoS2/Bi2wo6 Nanocomposites for Enhanced CO2 Photoreduction Activity under Visible Light Irradiation, *Appl. Surf. Sci.,* 2017, **403**, 230-239.
328. F. Xu, B. Zhu, B. Cheng, J. Yu and J. Xu, 1D/2D TiO_2/MoS_2 Hybrid Nanostructures for Enhanced Photocatalytic CO_2 Reduction, *Adv. Opt. Mater.,* 2018, **6**, 1800911.
329. S. Sun, X. Li, W. Wang, L. Zhang and X. Sun, Photocatalytic Robust Solar Energy Reduction of Dinitrogen to Ammonia on Ultrathin MoS_2, *Appl. Catal. B,* 2017, **200**, 323-329.
330. Z. Guo, J. Zhou, L. Zhu and Z. Sun, Mxene: A Promising Photocatalyst for Water Splitting, *J. Mater. Chem. A,* 2016, **4**, 11446-11452.
331. S. Trasatti, The Absolute Electrode Potential: An Explanatory Note (Recommendations 1986), *J. Electroanal. Chem. Interf. Electrochem.,* 1986, **209**, 417-428.
332. C. Sumesh and S. C. Peter, Two-Dimensional Semiconductor Transition Metal Based Chalcogenide Based Heterostructures for Water Splitting Applications, *Dalton Trans.,* 2019.
333. Y. Li, Q. Cui, F. Ceballos, S. D. Lane, Z. Qi and H. Zhao, Ultrafast Interlayer Electron Transfer in Incommensurate Transition Metal Dichalcogenide Homobilayers, *Nano Lett.,* 2017, **17**, 6661-6666.
334. C. Xia, W. Xiong, J. Du, T. Wang, Y. Peng and J. Li, Universality of Electronic Characteristics and Photocatalyst Applications in the Two-Dimensional Janus Transition Metal Dichalcogenides, *Phys. Rev. B,* 2018, **98**, 165424.
335. J. Zhang, S. Jia, I. Kholmanov, L. Dong, D. Er, W. Chen, H. Guo, Z. Jin, V. B. Shenoy, L. Shi and J. Lou, Janus Monolayer Transition-Metal Dichalcogenides, *ACS Nano,* 2017, **11**, 8192-8198.
336. Y.-J. Yuan, D. Chen, S. Yang, L.-X. Yang, J.-J. Wang, D. Cao, W. Tu, Z.-T. Yu and Z.-G. Zou, Constructing Noble-Metal-Free Z-Scheme Photocatalytic Overall Water Splitting Systems Using MoS2 Nanosheet Modified CdS as a H2 Evolution Photocatalyst, *J. Mater. Chem. A,* 2017, **5**, 21205-21213.
337. L. Ju, Y. Dai, W. Wei, M. Li and B. Huang, Dft Investigation on Two-Dimensional Ges/WS2 Van der Waals Heterostructure for Direct Z-Scheme Photocatalytic Overall Water Splitting, *Appl. Surf. Sci.,* 2018, **434**, 365-374.

338. J. Liao, B. Sa, J. Zhou, R. Ahuja and Z. Sun, Design of High-Efficiency Visible-Light Photocatalysts for Water Splitting: MoS2/AlN(GaN) Heterostructures, *J. Phys. Chem. C,* 2014, **118**, 17594-17599.
339. Z. Zhang, Q. Qian, B. Li and K. J. Chen, Interface Engineering of Monolayer MoS2/GaN Hybrid Heterostructure: Modified Band Alignment for Photocatalytic Water Splitting Application by Nitridation Treatment, *ACS Appl. Mater. Interfaces,* 2018, **10**, 17419-17426.
340. D. Sung, K.-A. Min and S. Hong, Investigation of Atomic and Electronic Properties of 2D-MoS2/3D-GaN Mixed-Dimensional Heterostructures, *Nanotechnology,* 2019, **30**, 404002.
341. X. Qian, J. Ding, J. Zhang, Y. Zhang, Y. Wang, E. Kan, X. Wang and J. Zhu, Ultrathin Molybdenum Disulfide/Carbon Nitride Nanosheets with Abundant Active Sites for Enhanced Hydrogen Evolution, *Nanoscale,* 2018, **10**, 1766-1773.
342. R. Kumar, D. Das and A. K. Singh, C2N/WS2 Van der Waals Type-Ii Heterostructure as a Promising Water Splitting Photocatalyst, *J. Catal.,* 2018, **359**, 143-150.
343. J. Li, E. Liu, Y. Ma, X. Hu, J. Wan, L. Sun and J. Fan, Synthesis of MoS2/g-C3N4 Nanosheets as 2D Heterojunction Photocatalysts with Enhanced Visible Light Activity, *Appl. Surf. Sci.,* 2016, **364**, 694-702.
344. M. Wang, P. Ju, J. Li, Y. Zhao, X. Han and Z. Hao, Facile Synthesis of MoS2/g-C3N4/GO Ternary Heterojunction with Enhanced Photocatalytic Activity for Water Splitting, *ACS Sustain. Chem. Eng.,* 2017, **5**, 7878-7886.
345. Y. Hou, Y. Zhu, Y. Xu and X. Wang, Photocatalytic Hydrogen Production over Carbon Nitride Loaded with WS2 as Cocatalyst under Visible Light, *Appl. Catal. B,* 2014, **156-157**, 122-127.
346. M. S. Akple, J. Low, S. Wageh, A. A. Al-Ghamdi, J. Yu and J. Zhang, Enhanced Visible Light Photocatalytic H2-Production of g-C3N4/WS2 Composite Heterostructures, *Appl. Surf. Sci.,* 2015, **358**, 196-203.
347. Y.-J. Yuan, D.-Q. Chen, Y.-W. Huang, Z.-T. Yu, J.-S. Zhong, T.-T. Chen, W.-G. Tu, Z.-J. Guan, D.-P. Cao and Z.-G. Zou, MoS2 Nanosheet-Modified CuInS2 Photocatalyst for Visible-Light-Driven Hydrogen Production from Water, *ChemSusChem,* 2016, **9**, 1003-1009.
348. T. Sun, H. Zhang, X. Wang, J. Liu, C. Xiao, S. U. Nanayakkara, J. L. Blackburn, M. V. Mirkin and E. M. Miller, Nanoscale Mapping of Hydrogen Evolution on Metallic and Semiconducting MoS_2 Nanosheets, *Nanoscale Horiz.,* 2019, **4**, 619-624.
349. M. A. Lukowski, A. S. Daniel, F. Meng, A. Forticaux, L. Li and S. Jin, Enhanced Hydrogen Evolution Catalysis from Chemically Exfoliated Metallic MoS2 Nanosheets, *J. Am. Chem. Soc.,* 2013, **135**, 10274-10277.
350. Z. Liu, N. Li, C. Su, H. Zhao, L. Xu, Z. Yin, J. Li and Y. Du, Colloidal Synthesis of 1T' Phase Dominated WS2 Towards Endurable Electrocatalysis, *Nano Energy,* 2018, **50**, 176-181.
351. U. Maitra, U. Gupta, M. De, R. Datta, A. Govindaraj and C. Rao, Highly Effective Visible-Light-Induced H2 Generation by Single-Layer 1T-MoS2 and a Nanocomposite of Few-Layer 2H-MoS2 with Heavily Nitrogenated Graphene, *Angew. Chem. Int. Ed.,* 2013, **52**, 13057-13061.
352. B. Mahler, V. Hoepfner, K. Liao and G. A. Ozin, Colloidal Synthesis of 1T-WS2 and 2H-WS2 Nanosheets: Applications for Photocatalytic Hydrogen Evolution, *J. Am. Chem. Soc.,* 2014, **136**, 14121-14127.

353. X. Zong, J. Han, G. Ma, H. Yan, G. Wu and C. Li, Photocatalytic H2 Evolution on CdS Loaded with WS2 as Cocatalyst under Visible Light Irradiation, *J. Phys. Chem. C,* 2011, **115**, 12202-12208.
354. D. A. Reddy, H. Park, R. Ma, D. P. Kumar, M. Lim and T. K. Kim, Heterostructured WS2-MoS2 Ultrathin Nanosheets Integrated on CdS Nanorods to Promote Charge Separation and Migration and Improve Solar-Driven Photocatalytic Hydrogen Evolution, *ChemSusChem,* 2017, **10**, 1563-1570.
355. M. Zhu, C. Zhai, M. Fujitsuka and T. Majima, Noble Metal-Free near-Infrared-Driven Photocatalyst for Hydrogen Production Based on 2D Hybrid of Black Phosphorus/WS2, *Appl. Catal. B,* 2018, **221**, 645-651.
356. F. M. Pesci, M. S. Sokolikova, C. Grotta, P. C. Sherrell, F. Reale, K. Sharda, N. Ni, P. Palczynski and C. Mattevi, MoS2/WS2 Heterojunction for Photoelectrochemical Water Oxidation, *ACS Catal.,* 2017, **7**, 4990-4998.
357. P. C. Sherrell, P. Palczynski, M. S. Sokolikova, F. Reale, F. M. Pesci, M. Och and C. Mattevi, Large-Area CVD MoS2/WS2 Heterojunctions as a Photoelectrocatalyst for Salt-Water Oxidation, *ACS Appl. Energy Mater.,* 2019, **2**, 5877-5882.
358. J. Pan, Z. Wang, Q. Chen, J. Hu and J. Wang, Band Structure Engineering of Monolayer Mos 2 by Surface Ligand Functionalization for Enhanced Photoelectrochemical Hydrogen Production Activity, *Nanoscale,* 2014, **6**, 13565-13571.
359. Y. Suo, H. Liu, S. Huang, Y. Zhang and K. Ding, The Functionalization Effect of Benzoic Acid and Anisole on the Photocatalytic Activity of Monolayer MoS2, *Appl. Surf. Sci.,* 2018, **437**, 314-320.
360. Y. Sun and K. Liu, Strain Engineering in Functional 2-Dimensional Materials, *J. Appl. Phys.,* 2018, **125**, 082402.
361. D. Y. Hwang, K. H. Choi, J. E. Park and D. H. Suh, Highly Efficient Hydrogen Evolution Reaction by Strain and Phase Engineering in Composites of Pt and MoS2 Nano-Scrolls, *Phys. Chem. Chem. Phys.,* 2017, **19**, 18356-18365.
362. H. Li, C. Tsai, A. L. Koh, L. Cai, A. W. Contryman, A. H. Fragapane, J. Zhao, H. S. Han, H. C. Manoharan, F. Abild-Pedersen, J. K. Nørskov and X. Zheng, Activating and Optimizing MoS2 Basal Planes for Hydrogen Evolution through the Formation of Strained Sulphur Vacancies, *Nat. Mater.,* 2015, **15**, 48.
363. S. Pak, J. Lee, Y.-W. Lee, A. R. Jang, S. Ahn, K. Y. Ma, Y. Cho, J. Hong, S. Lee, H. Y. Jeong, H. Im, H. S. Shin, S. M. Morris, S. Cha, J. I. Sohn and J. M. Kim, Strain-Mediated Interlayer Coupling Effects on the Excitonic Behaviors in an Epitaxially Grown MoS2/WS2 Van der Waals Heterobilayer, *Nano Lett.,* 2017, **17**, 5634-5640.
364. G. M. Carroll, H. Zhang, J. R. Dunklin, E. M. Miller, N. R. Neale and J. Van De Lagemaat, Unique Interfacial Thermodynamics of Few-Layer 2D Mos 2 for (Photo) Electrochemical Catalysis, *Energy & Environmental Science,* 2019, **12**, 1648-1656.
365. S. Vanka, Y. Wang, P. Ghamari, S. Chu, A. Pandey, P. Bhattacharya, I. Shih and Z. Mi, A High Efficiency Si Photoanode Protected by Few-Layer MoSe2, *Sol. RRL,* 2018, **2**, 1800113.
366. L. A. King, T. R. Hellstern, J. Park, R. Sinclair and T. F. Jaramillo, Highly Stable Molybdenum Disulfide Protected Silicon Photocathodes for Photoelectrochemical Water Splitting, *ACS Appl. Mater. Interfaces,* 2017, **9**, 36792-36798.

367. A. B. Laursen, T. Pedersen, P. Malacrida, B. Seger, O. Hansen, P. C. K. Vesborg and I. Chorkendorff, MoS2—an Integrated Protective and Active Layer on n+p-Si for Solar H2 Evolution, *Phys. Chem. Chem. Phys.,* 2013, **15**, 20000-20004.
368. Q. Ding, F. Meng, C. R. English, M. Cabán-Acevedo, M. J. Shearer, D. Liang, A. S. Daniel, R. J. Hamers and S. Jin, Efficient Photoelectrochemical Hydrogen Generation Using Heterostructures of Si and Chemically Exfoliated Metallic MoS2, *J. Am. Chem. Soc.,* 2014, **136**, 8504-8507.
369. P. Gnanasekar, D. Periyanagounder, P. Varadhan, J.-H. He and J. Kulandaivel, Highly Efficient and Stable Photoelectrochemical Hydrogen Evolution with 2D-NbS2/Si Nanowire Heterojunction, *ACS Appl. Mater. Interfaces,* 2019, **11**, 44179-44185.
370. Y. Fu, F. Cao, F. Wu, Z. Diao, J. Chen, S. Shen and L. Li, Phase-Modulated Band Alignment in CdS Nanorod/SnSx Nanosheet Hierarchical Heterojunctions toward Efficient Water Splitting, *Adv. Funct. Mater.,* 2018, **28**, 1706785.
371. J. Chen, C. S. Bailey, Y. Hong, L. Wang, Z. Cai, L. Shen, B. Hou, Y. Wang, H. Shi, J. Sambur, W. Ren, E. Pop and S. B. Cronin, Plasmon-Resonant Enhancement of Photocatalysis on Monolayer WSe2, *ACS Photonics,* 2019, **6**, 787-792.
372. Z. Yin, B. Chen, M. Bosman, X. Cao, J. Chen, B. Zheng and H. Zhang, Au Nanoparticle-Modified MoS2 Nanosheet-Based Photoelectrochemical Cells for Water Splitting, *Small,* 2014, **10**, 3537-3543.
373. Y. Jing, Y. Ma, Y. Wang, Y. Li and T. Heine, Ultrathin Layers of Pdpx (X=S, Se): Two Dimensional Semiconductors for Photocatalytic Water Splitting, *Chem. Eur. J.,* 2017, **23**, 13612-13616.
374. X. Xu, G. Zhou, X. Dong and J. Hu, Interface Band Engineering Charge Transfer for 3D MoS2 Photoanode to Boost Photoelectrochemical Water Splitting, *ACS Sustain. Chem. Eng.,* 2017, **5**, 3829-3836.
375. Q. Pan, C. Zhang, Y. Xiong, Q. Mi, D. Li, L. Zou, Q. Huang, Z. Zou and H. Yang, Boosting Charge Separation and Transfer by Plasmon-Enhanced MoS2/BiVO4 P–N Heterojunction Composite for Efficient Photoelectrochemical Water Splitting, *ACS Sustain. Chem. Eng.,* 2018, **6**, 6378-6387.
376. Y. Shi, J. Wang, C. Wang, T.-T. Zhai, W.-J. Bao, J.-J. Xu, X.-H. Xia and H.-Y. Chen, Hot Electron of Au Nanorods Activates the Electrocatalysis of Hydrogen Evolution on MoS2 Nanosheets, *J. Am. Chem. Soc.,* 2015, **137**, 7365-7370.
377. H. Zhang, J. R. Dunklin, O. G. Reid, S. J. Yun, S. U. Nanayakkara, Y. H. Lee, J. L. Blackburn and E. M. Miller, Disentangling Oxygen and Water Vapor Effects on Optoelectronic Properties of Monolayer Tungsten Disulfide, *Nanoscale,* 2020, **12**, 8344-8354.
378. H. Qin, R.-T. Guo, X.-Y. Liu, W.-G. Pan, Z.-Y. Wang, X. Shi, J.-Y. Tang and C.-Y. Huang, Z-Scheme MoS2/g-C3N4 Heterojunction for Efficient Visible Light Photocatalytic CO2 Reduction, *Dalton Trans.,* 2018, **47**, 15155-15163.
379. Y. Wang, Z. Zhang, L. Zhang, Z. Luo, J. Shen, H. Lin, J. Long, J. C. S. Wu, X. Fu, X. Wang and C. Li, Visible-Light Driven Overall Conversion of CO2 and H2O to CH4 and O2 on 3D-SiC@2D-MoS2 Heterostructure, *J. Am. Chem. Soc.,* 2018, **140**, 14595-14598.
380. W. Ye, M. Arif, X. Fang, M. A. Mushtaq, X. Chen and D. Yan, Efficient Photoelectrochemical Route for the Ambient Reduction of N2 to NH3 Based on Nanojunctions

Assembled from MoS2 Nanosheets and TiO2, *ACS Appl. Mater. Interfaces,* 2019, **11**, 28809-28817.
381. K. Chu, Y.-p. Liu, Y.-b. Li, Y.-l. Guo and Y. Tian, Two-Dimensional (2D)/2D Interface Engineering of a MoS2/C3N4 Heterostructure for Promoted Electrocatalytic Nitrogen Fixation, *ACS Appl. Mater. Interfaces,* 2020, **12**, 7081-7090.
382. Z.-D. Luo, X. Xia, M.-M. Yang, N. R. Wilson, A. Gruverman and M. Alexe, Artificial Optoelectronic Synapses Based on Ferroelectric Field-Effect Enabled 2D Transition Metal Dichalcogenide Memristive Transistors, *ACS Nano,* 2020, **14**, 746-754.
383. D. D. Awschalom, R. Hanson, J. Wrachtrup and B. B. Zhou, Quantum Technologies with Optically Interfaced Solid-State Spins, *Nat. Photonics,* 2018, **12**, 516-527.
384. Z. Gong, G.-B. Liu, H. Yu, D. Xiao, X. Cui, X. Xu and W. Yao, Magnetoelectric Effects and Valley-Controlled Spin Quantum Gates in Transition Metal Dichalcogenide Bilayers, *Nat. Commun.,* 2013, **4**, 2053.